

Gravitational Wave Polarizations: A test of General Relativity using Binary Black hole mergers

Thesis by
Sudhi Mathur

In Partial Fulfillment of the Requirements for the
Degree of
Bachelor of Science, Physics

CALIFORNIA INSTITUTE OF TECHNOLOGY
Pasadena, California

2020
Defended June 5, 2020

© 2020

Sudhi Mathur

ORCID: 0000-0003-4891-0567

All rights reserved except where otherwise noted

ACKNOWLEDGEMENTS

The author gratefully acknowledges mentor Professor Alan Weinstein for this incredible opportunity and for his extensive support and guidance throughout the duration of the thesis.

The author would also like to thank Samuel Patrone (Caltech SURF student 2019), whose work this thesis is building upon, and acknowledge the support of Colm Talbot, Philippe Grassia, and Qing Gao.

The author extends gratitude to the United States National Science Foundation (NSF) for the construction and operation of the LIGO Laboratory and Advanced LIGO and would also like to thank the Science and Technology Facilities Council (STFC) of the United Kingdom, the Max-Planck-Society (MPS), and the State of Niedersachsen, Germany for their support in the construction of Advanced LIGO and operation of the GEO600 detector. Additional support for Advanced LIGO was provided by the Australian Research Council.

The author recognizes the Italian Istituto Nazionale di Fisica Nucleare (INFN), the French Centre National de la Recherche Scientifique (CNRS) and the Foundation for Fundamental Research on Matter supported by the Netherlands Organisation for Scientific Research for facilitating the construction and operation of the Virgo detector and the creation of the EGO consortium.

The author would also like to acknowledge the support of the NSF, STFC, INFN and CNRS for the provision of computational resources.

We would like to wholeheartedly thank all of the essential workers who put their health at risk during the COVID-19 pandemic, without whom we would not have been able to complete this work.

ABSTRACT

General Relativity predicts that gravitational radiation is purely tensor polarized and thus, gravitational waves are composed of linear combinations of two transverse polarization modes, referred to as plus (+) and cross (\times) tensor modes. However, alternate gravitational theories predict the existence of up to four additional vector and scalar longitudinal GW polarization modes.

In this thesis, we develop a test of the gravitational wave (GW) polarization prediction of general relativity by searching for small admixtures of vector and/or scalar polarization components in transient GWs from binary black hole mergers. We use a network of five non-co-oriented GW detectors available in the near future, Bayesian inference parameter estimation, and nested sampling to quantify the detection sensitivity for such non-tensor GW polarization components.

TABLE OF CONTENTS

Acknowledgements	iii
Abstract	iv
Table of Contents	v
List of Illustrations	vi
List of Tables	ix
Chapter I: Introduction	1
1.1 Gravitational wave polarizations	2
1.2 Theoretical background	6
1.3 Detector response and Antenna patterns	9
1.4 Ground-based detector network	14
Chapter II: Methods	18
2.1 Generating BBH Tensor-Vector-Scalar (tvs) polarized GW waveforms	18
2.2 Simulating detector response	24
2.3 Bayesian Inference	31
2.4 Quantifying polarization detection sensitivities	33
Chapter III: Results	36
3.1 Single Event Analysis	39
3.2 Multiple Event Analysis	65
Chapter IV: Summary, Conclusion and Future Work	67
4.1 Summary	67
4.2 Conclusion	68
4.3 Future work	71
Bibliography	72
Appendix A: Single Event Analysis	75
A.1 Tensor-Vector-Scalar (tvs) polarized GWs	75
A.2 Tensor-Vector (tv) polarized GWs	90
A.3 Tensor-Scalar (ts) polarized GWs	97
A.4 Tensor-Vector-Scalar (tvs) polarized GWs; uniform ψ prior	104

LIST OF ILLUSTRATIONS

<i>Number</i>	<i>Page</i>
1.1 The metric perturbation matrix for a general metric theory of gravity	3
1.2 Effects of GW polarization modes on a ring of free falling particles	3
1.3 The metric perturbation matrix for GR	4
1.4 GW polarization predictions of alternative gravitational theories	5
1.5 Layout of an Advanced LIGO detector	9
1.6 Local geometry of an incoming GW signal and a GW detector	12
1.7 Detector antenna patterns	13
1.8 Ground-based detector network	14
1.9 Network sensitivity of ground-based detectors for non-tensor GW polarization modes	16
1.10 Duty cycles of the detector network	17
2.1 Numerical relativity-based waveform modelling for a BBH merger	18
2.2 Waveforms of simulated GW polarization modes	22
2.3 Sanity check for simulated GW waveforms	23
2.4 Another sanity check for simulated GW waveforms	24
2.5 Detector noise curves	26
2.6 Detector noise and Signal magnitudes	28
2.7 Detector response to various GW signals with different polarization content	30
3.1 Corner plot for posterior probability distributions recovered through Bayesian parameter estimation	38
3.2 Violin plot of λ_v posteriors for tvs polarized GW in all possible three-detector combinations	40
3.3 Violin plot of λ_v posteriors for tvs polarized GW in all possible four-detector combinations	41
3.4 Violin plot of λ_v posteriors for tvs polarized GW in five detectors	42
3.5 Violin plot of λ_s posteriors for tvs polarized GW in all possible three-detector combinations	44
3.6 Violin plot of λ_s posteriors for tvs polarized GW in all possible four-detector combinations	45
3.7 Violin plot of λ_s posteriors for tvs polarized GW in five detectors	46
3.8 Violin plot of λ_v posteriors for tv polarized GW in all possible three-detector combinations	48

3.9	Violin plot of λ_v posteriors for tv polarized GW in all possible four-detector combinations	49
3.10	Violin plot of λ_v posteriors for tv polarized GW in five detectors	50
3.11	Violin plot of λ_s posteriors for ts polarized GW in all possible three-detector combinations	52
3.12	Violin plot of λ_s posteriors for ts polarized GW in all possible four-detector combinations	53
3.13	Violin plot of λ_s posteriors for ts polarized GW in five detectors	54
3.14	Violin plot of λ_v posteriors for tvs polarized GW in all possible three-detector combinations (uniform ψ prior distribution)	56
3.15	Violin plot of λ_v posteriors for tvs polarized GW in all possible four-detector combinations (uniform ψ prior distribution)	57
3.16	Violin plot of λ_v posteriors for tvs polarized GW in five detectors (uniform ψ prior distribution)	58
3.17	Violin plot of λ_s posteriors for tvs polarized GW in three-detector combinations (uniform ψ prior distribution)	60
3.18	Violin plot of λ_s posteriors for tvs polarized GW in four-detector combinations (uniform ψ prior distribution)	61
3.19	Violin plot of λ_s posteriors for tvs polarized GW in five detectors (uniform ψ prior distribution)	62
3.20	Violin plot of $\vec{\lambda}$ parameters for tvs polarized GWs with different BBH component masses in five detectors	64
3.21	Multiple Event Analysis for λ_v posterior probability distributions	66
3.22	Multiple Event Analysis for λ_s posterior probability distributions	66
A.1	Histograms of λ_v posteriors for tvs polarized GWs averaged over all possible three, four and five detector combinations	79
A.2	Histograms of λ_s posteriors for tvs polarized GWs averaged over all possible three, four and five detector combinations	86
A.3	Histograms of λ_v posteriors for tv polarized GWs averaged over all possible three, four and five detector combinations	93
A.4	Histograms of λ_s posteriors for ts polarized GWs averaged over three, four and five detector combinations	100
A.5	Histograms of λ_v posteriors for tvs polarized GWs averaged over three, four and five detector combinations (uniform ψ prior distribution)	107
A.6	Histograms of λ_s posteriors for tvs polarized GWs averaged over three, four and five detector combinations (uniform ψ prior distribution)	115

A.7	Histograms of $\vec{\lambda}$ posteriors for tvs polarized GWs with different BBH component masses in five detectors	119
-----	--	-----

LIST OF TABLES

<i>Number</i>	<i>Page</i>	
2.1	Parameters used to generate general relativistic GW signal of a BBH merger	19
2.2	General parameter values used to generate tvs polarized GW signal	21
2.3	$\vec{\lambda}$ parameter values used to generate the BBH tvs polarized GW signal	23
2.4	Parameter values for checking detector response to different polarization content . . .	29
2.5	List of questions explored in the thesis and computational approach	34
2.6	Additional questions addressed in thesis and computational approach	35
3.1	Common parameters for violin plots of $\vec{\lambda}$ parameters for tvs, tv and ts polarized GWs in all possible combinations of three, four and five detectors	37
3.2	Common parameters for violin plots of $\vec{\lambda}$ parameters for tvs polarized GWs with different BBH component masses	63
A.1	λ_v posterior 90% credible intervals for tvs polarized GWs with progressively in- creasing λ_v true values	81
A.2	λ_v posterior 90% upper and lower limits for tvs polarized GWs	81
A.3	λ_s posterior 90% credible intervals for tvs polarized GWs with randomly chosen λ_s true values	82
A.4	λ_s posterior 90% credible intervals for tvs polarized GWs with progressively in- creasing λ_s true values	88
A.5	λ_s posterior 90% upper and lower limits for tvs polarized GWs	88
A.6	λ_v posterior 90% credible intervals for tvs polarized GWs with randomly chosen λ_v true values	89
A.7	λ_v credible intervals for tv polarized GWs with progressively increasing λ_v true values	95
A.8	λ_v posterior 90% upper and lower limits for tv polarized GWs	95
A.9	λ_s credible intervals for tv polarized GWs with λ_s true = 0	96
A.10	λ_s credible intervals for ts polarized GWs with progressively increasing λ_s true values	102
A.11	λ_s posterior 90% upper and lower limits for ts polarized GWs	102
A.12	λ_v credible intervals for ts polarized GWs with λ_v true = 0	103
A.13	λ_v credible intervals for tvs polarized GWs with progressively increasing λ_v true values (uniform ψ prior distribution)	109
A.14	λ_v posterior 90% upper and lower limits for tvs polarized GWs (uniform ψ prior distribution)	109
A.15	λ_s credible intervals for tvs polarized GWs with randomly chosen λ_s true values (uniform ψ prior distribution)	110

A.16	λ_s posterior 90% credible intervals for tvs polarized GWs with progressively increasing λ_s true values (uniform ψ prior distribution)	117
A.17	λ_s posterior 90% upper and lower limits for tvs polarized GWs (uniform ψ prior distribution)	117
A.18	λ_v posterior 90% credible intervals for tvs polarized GWs with randomly chosen λ_v true values (uniform ψ prior distribution)	118
A.19	λ_v posterior 90% credible intervals for tvs polarized GWs with different BBH component masses	119
A.20	λ_s posterior 90% credible intervals for tvs polarized GWs with different BBH component masses	120

Chapter 1

Introduction

The detection of gravitational waves (GWs) by the Advanced Laser Interferometer Gravitational-Wave Observatory (aLIGO) and Virgo has enabled experimental studies of gravity in highly dynamic and strong-field regimes, which are inaccessible to laboratory, Solar System or cosmological tests of gravity [1–5]. These detections have been used to place some of the most stringent constraints on deviations from the general theory of relativity (GR).

General Relativity predicts that gravitational radiation is purely tensor polarized and thus, gravitational waves are composed of linear combinations of two transverse polarization modes, referred to as plus (+) and cross (×) tensor modes. However, alternate gravitational theories predict the existence of up to four additional vector and scalar longitudinal GW polarization modes. Thus, resolving the polarization content of GWs is a fundamental test of GR against alternate theories of gravity [6, 7].

It is possible to resolve the polarization components of continuous GWs using a single GW detector. This can be done by observing the distinct and predictable amplitude modulations of continuous GW polarizations as the Earth spins with respect to the fixed stars [8]. However, such continuous signals have not yet been observed.

On the other hand, transient GWs from compact binary coalescences (CBCs) have been directly observed and are well-modeled using numerical relativity.

However, it is challenging to learn about the polarization content of such GWs using signals solely from the three detector LIGO-Virgo network [9–11]. This is because, for such transient GW signals, three GW detectors are insufficient to resolve all polarization mode degeneracies and characterize the GW polarization content [7, 12, 13]. All existing observations of GWs from CBCs are so far consistent with predictions from GR, under the assumption of purely GR polarizations [5].

For transient GWs from CBCs, constraints on the amount of non-GR polarization can be placed in an indirect manner. However, such measurements do not probe the geometric effect of the GW directly and provide no direct, model-independent information on the actual polarization content of gravitational radiation [12, 13]. For example, measurements of the orbital decay of binary systems (see [14, 15] or [16, 17]), which are sensitive to the total radiated GW power, can constrain the power contained in non-GR polarizations. However, there may be multiple theories, with different polarization content, that still predict the correct observed GW power within expected errors [18–

21].

Prospects for direct observation of GW polarizations are improved by combining measurements from an increasing number of non-co-oriented GW detectors. In principle, for transient GW signals, at least five non-co-oriented differential-arm GW detectors are required to break all degeneracies among the five non-degenerate polarizations allowed by general metric theories of gravity [8, 22, 23]. The purpose of this study is to quantify how well we can constrain the polarization components of transient GWs with five or fewer than five non-co-oriented GW detectors.

In this thesis, we present a Bayesian parameter estimation methodology for extracting information about GW polarizations directly from transient CBC signals of Binary Black hole (BBH) mergers observable by a ground-based GW detector network in the near future.

1.1 Gravitational wave polarizations

In GR and all other theories that respect Einstein's equivalence principle, gravitational interactions can be fully described via the universal coupling of matter to a metric tensor [6, 24]. Consequently, in any such metric theory a nearly-null plane GW can be encoded in at most six independent components of the Riemann tensor at all points in spacetime [6, 22]. These six degrees of freedom give rise to six geometrically distinct polarizations, corresponding to the six independent components of the arbitrary metric perturbation [13].

The metric perturbation of gravitational waves, at any given point \vec{x} in spacetime can be written as

$$h_{ab}(\vec{x}) = h_A(\vec{x})e_{ab}^A \quad (1.1)$$

where $h_A(\vec{x})$ are six independent amplitudes and e_{ab}^A are the six polarization tensors implicitly summed over polarizations A , and ab are spacetime 4-vector indices.

For a GW propagating in the direction of the spatial unit vector $\mathbf{w}_z = \mathbf{w}_x \times \mathbf{w}_y$, there exists a purely space-like Lorentz gauge with Cartesian coordinates along $(\mathbf{w}_x, \mathbf{w}_y, \mathbf{w}_z)$ (Figure 1.1) such that the 4×4 tensor metric perturbation equation (Eq.1.1) collapses into a 3×3 spatial matrix,

$$[h_{ij}] = \begin{pmatrix} h_b + h_+ & h_\times & h_x \\ h_\times & h_b - h_+ & h_y \\ h_x & h_y & h_l \end{pmatrix} \quad (1.2)$$

where h_A represents the amplitudes of the linear polarizations for plus (+) and cross (\times) tensor modes; vector-x (x) and vector-y (y) modes; breathing (b) and longitudinal (l) scalar modes [13].

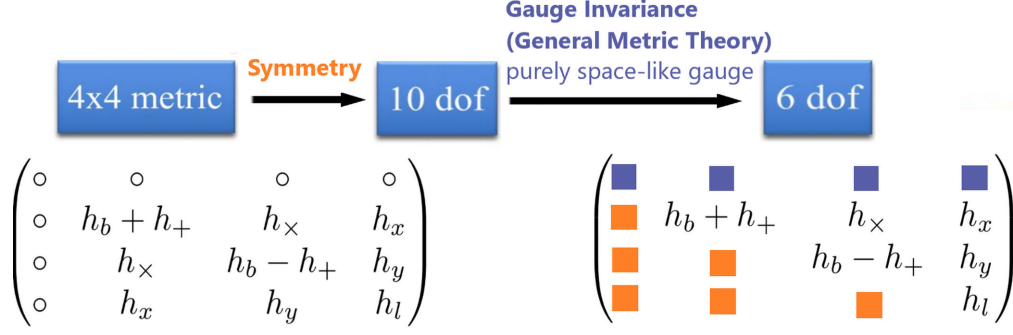


Figure 1.1: The 4x4 tensor metric perturbation $h_{ab}(\vec{x})$ (Eq.1.1) with 16 degrees of freedom collapses into a 3x3 spatial matrix $[h_{ij}]$ (Eq. 1.2) with 6 degrees of freedom by arguments of symmetry and Gauge invariance.

It is important to note that in a traceless gauge we would have $2h_b + h_l = 0$. However, in a more general gauge or theory h_b and h_l are unconstrained, free parameters. Thus, depending upon different assumptions, we refer to either five or (usually) six polarization modes throughout this study.

The six different GW linear polarization modes have different geometrical effects that exhibit different directions of the stretching and squeezing of spacetime on a ring of free falling particles (Figure 1.2) [22, 23].

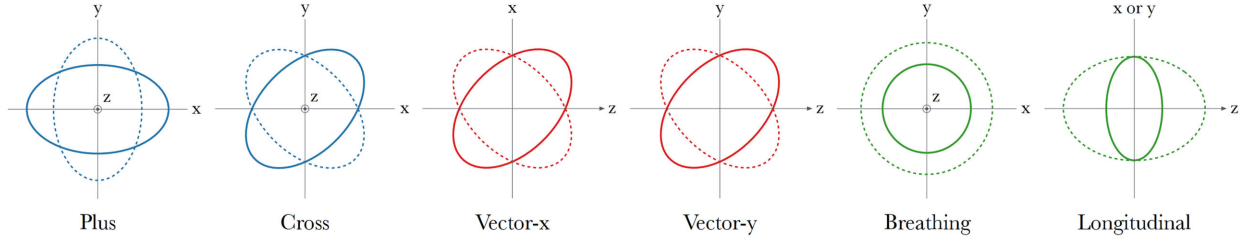


Figure 1.2: Effects of different GW polarization modes (plus (+) and cross (x) tensor modes; vector-x (x) and vector-y (y) modes; breathing (b) and longitudinal (l) scalar modes) on a ring of free falling particles. In all of these diagrams the GW propagates along the z direction (into the plane for plus (+), cross (x) and breathing (b) modes; to the right for vector-x (x), vector-y (y) and longitudinal (l) modes) [23].

Note that a purely scalar polarization mode looks like a three-dimensional breathing mode that causes the stretching and squeezing of a sphere of free falling particles in all directions. The “sixth” polarization mode is created by artificially breaking this purely scalar mode into equal amounts of scalar polarizations in the transverse (b) and longitudinal (l) directions (Plot 5 and 6 in Figure 1.2).

This is done to observe any unequal detector DARM response (Section 1.3) to the otherwise zero net scalar response in a general relativistic gauge.

GR allows only linear combinations of the tensor (+) and (\times) polarizations (Figure 1.3) [6]. This is a direct consequence of the Bianchi identities and the Einstein Field Equations (EFE) outlined in subsection 1.2.

6 dof Transverse 2 dof

$$\begin{pmatrix} h_b + h_+ & h_x & h_x \\ h_x & h_b - h_+ & h_y \\ h_x & h_y & h_l \end{pmatrix} \xrightarrow{G_{\mu\nu} = \frac{8\pi G}{c^4} T_{\mu\nu}} \begin{pmatrix} h_+ & h_x \\ h_x & -h_+ \end{pmatrix}$$

Traceless

Figure 1.3: In GR, the 3×3 spatial matrix $[h_{ij}]$ (Eq. 1.2) with 6 degrees of freedom collapses into a 2×2 spatial matrix with only 2 degrees of freedom due to the Bianchi identities and the EFE (more in the subsection 1.2). Thus, GR allows only linear combinations of the tensor (+) and (\times) polarizations [6].

However, alternative theories of gravity predict the existence of vector and scalar modes in addition to the general relativistic tensor polarization modes. Scalar-tensor theories and some theories with extra dimensions predict the presence of the breathing component (Plot 5 in Figure 1.2) associated with a scalar field [25, 26]. Massive-graviton frameworks and bimetric theories, such as the Rosen or Lightman-Lee theory, predict the presence of both vector and scalar modes [27–29]. Less conventional theories [30] predict the presence of either vector or scalar modes only. Figure 1.4 outlines the GW polarization predictions of a few alternative gravitational theories.

These alternate theories do not intend to replace GR, but to challenge its completeness and possibly modify GR into a more generalized theory of gravity. They can be tested without invoking GW polarization predictions. However, GW polarization predictions provide a new and powerful test for such alternative theories of gravity and for the completeness of GR.

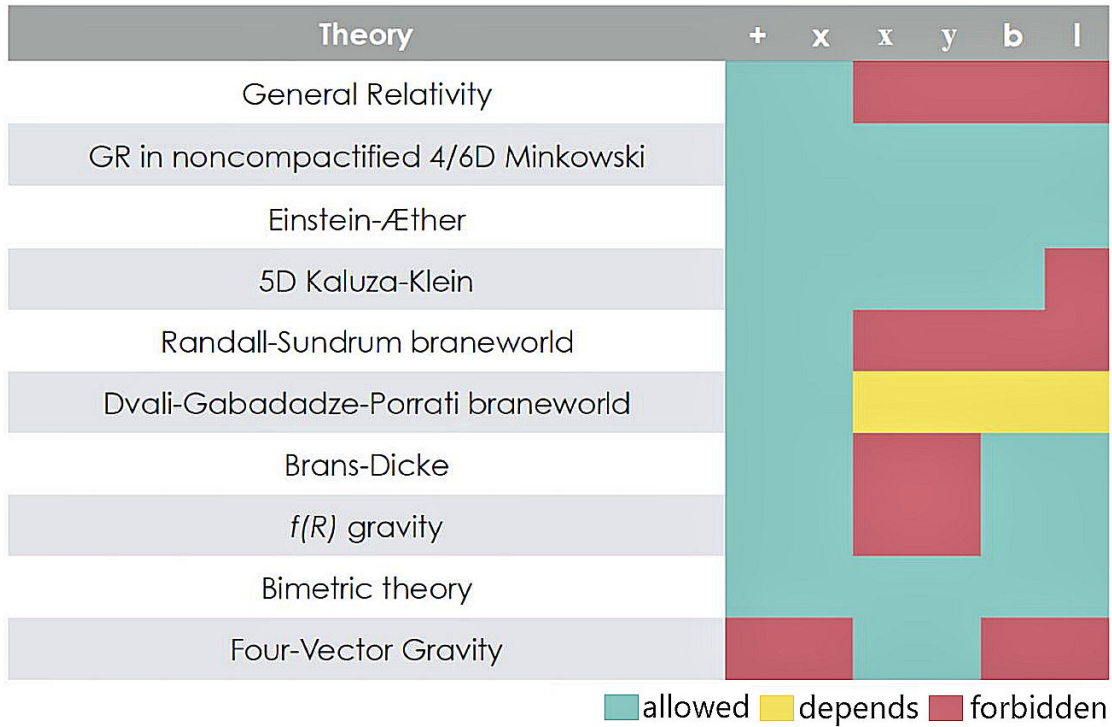


Figure 1.4: The GW polarization predictions of alternative theories of gravity [31, 32].

In this thesis, we explore the possibility of detecting small admixtures of vector and/or scalar polarizations in gravitational radiation. We explore beyond GR regimes by simulating BBH transient GW signals with tensor, vector and scalar polarization components in a network of five non-co-oriented GW detectors available in the near future. We quantitatively determine the detection sensitivity towards small admixtures of vector and/or scalar polarizations in the simulated GW signal.

1.2 Theoretical background

“Experimental tests of relativistic gravitational effects should be carried on using a broader theoretical framework than provided by general relativity alone [6].”

- Clifford M. Will

Motivation for exploring alternate gravitational theories

Einstein used electromagnetic theory as a foundation for special relativity. GR is motivated by a theoretical criterion of elegance and simplicity and a primary goal of producing a gravitational theory that incorporates the principle of equivalence and special relativity, rather than a desire to account for unexplained experimental or observational results [6].

GR has been tested to a high level of accuracy within the Solar System. It accounts for the anomalous perihelion advance of Mercury, deflection of light by the Sun’s gravitational field, gravitational redshift, Shapiro time delay and the absence of Nordtvedt effect in lunar motion. However, the Solar System cannot be regarded as the absolute testing ground for gravitational theories. This is because many alternate theories of gravity agree with GR in their weak-field, slow-motion limits closely enough to pass all the Solar System tests. Disparities between alternate theories of gravity and GR become more apparent through other predictions involving spacetime near compact objects, and gravitational radiation or cosmological phenomenon in strong-field, highly dynamical gravity regimes [6].

Some fundamental predictions of GR have also been tested through cosmological tests and in strong-field and highly dynamical gravity regimes such as binary pulsars, neutron stars, black holes, and inspiralling compact binaries [6].

However, the fundamental prediction of GR that GW have only two linearized tensor polarization components has not been tested using GW observations, except in the extreme and crude case of distinguishing purely-tensor polarized GWs from purely-vector or purely-scalar polarized GWs [5, 11, 13]. More generalized and subtle mixtures of GW polarization contents are yet to be extensively explored.

To incorporate non-tensorial gravitational polarization components, alternative theories of gravity modify the very foundations of GR, such as the equivalence principle and the Einstein Field Equations (discussed in the next section).

Our motivation for exploring alternative theories of gravity and beyond GR regimes by searching for such non-tensor GW polarizations in the near future is threefold. Firstly, as gravity is a fundamental interaction of nature, it requires the most solid empirical underpinning we can provide. Secondly, all attempts to quantize gravity and to unify it with other forces of nature suggest that GR might

be an incomplete theory of gravitation. And lastly, as GR contains no adjustable constants, its predictions are fixed. This implies that tests of any fundamental prediction of GR, including the search for non-tensor GW polarizations, is either a dead end or a possible probe for new physics [6].

Equivalence principle and non-tensor gravitational fields

The Equivalence principle (EP) is one of the fundamental foundations of gravitational theory and states that gravitation is a phenomenon of curved spacetime [6].

The EP assumes equivalence between inertial mass and gravitational mass $m_I = m_g$ and, thus, for the force equations

$$\vec{F} = m_I \vec{a}, \quad \vec{F} = m_g \vec{g} \quad (1.3)$$

$$\vec{a} = \vec{g} \quad (1.4)$$

where g is the gravitational field.

This implies that, the gravitational interaction of an object with the field it is in can be fully understood solely through its location in the field. That is, gravity is a purely geometric phenomenon that can be completely explained by the geometry of spacetime as quantified by the space time metric. Thus, the EP leads to “metric” theories of gravity.

Based on the EP and inspired by Maxwell’s equations for electromagnetism, Einstein’s Field Equations (EFE) (Eq. 1.5) describe how matter and energy fit into gravity through continuous and discrete transformations of space and matter.

$$G_{\mu\nu} = \frac{8\pi G}{c^4} T_{\mu\nu} \quad (1.5)$$

where the Einstein tensor $G_{\mu\nu}$ describes space time curvature and the stress-energy tensor $T_{\mu\nu}$ represents matter and energy.

These field equations describe gravitational field dynamics and obey Poincaré invariance, which incorporates special relativistic symmetries of rotations and translations in spacetime including isotropy, homogeneity of space, Lorentz invariance, and time-translation invariance [33]. Such symmetries are spontaneously broken at any particular point in space when we consider initial conditions such as externally applied electric and magnetic fields.

However, to accommodate vector and scalar gravitational fields, alternate metric theories of gravity modify the existing theoretical framework.

From a quantum mechanical viewpoint, accounting for such vector and scalar gravitational fields is relatively simple. This can be done by endowing the graviton with an effective mass.

On one hand, GR predicts that gravitons are massless in a vacuum and only gain a negligibly small induced mass when they interact with matter. This is a direct consequence of the Bianchi identities in a vacuum

$$G^{\alpha\beta}_{;\beta} = 0 \quad (1.6)$$

and the EFE (Eq.1.5) which outline gravity-matter interactions.

The Bianchi identities in a vacuum (Eq. 1.6) are analogous to $\nabla \cdot \vec{E} = 0$ in electromagnetism. We draw such a parallel between gravity and electromagnetism as electromagnetic waves are carried by spin 1 photons while gravity is carried by spin 2 gravitons.

In electromagnetism, transverse electric fields in a vacuum imply that photons are massless and, thus, exhibit only two of their three total possible polarizations states given by ($m_s = \pm 1$). The longitudinal polarization mode (corresponding to $m_s = 0$) for a photon is absent in a vacuum. Similarly, in a vacuum, the general relativistic solution of the Bianchi identities (Eq. 1.6) implies gravitational waves are transverse and, thus, gravitons are massless.

Moreover, the EFE predict that a graviton moving in ordinary matter will acquire an induced mass. This effect is similar to photons gaining an effective mass when they interact with matter. However, as the interaction of gravity with matter is extremely weak, the induced graviton mass is negligibly small.

Thus, in GR, gravitons are essentially massless and must exhibit only two tensorial polarization modes ($m_s = \pm 2$) out of their five possible polarization modes given by ($m_s = 0, \pm 1, \pm 2$) for spin 2 particles.

By contrast, massive graviton metric theories endow the graviton with a significant mass and assume that gravitation is not transverse, but only traceless [27]. This allows for a more general solution where all five possible polarization modes exist (Eq. 1.2). Mathematically, this represents the effects of the existence of vector and scalar gravitational fields.

Thus, GR predicts that gravitational radiation must be purely tensor polarized as it is carried by massless gravitons. On the other hand, endowing the graviton with an effective mass gives rise to vector ($m_s = \pm 1$) and scalar ($m_s = 0$) polarization modes in addition to the tensor ($m_s = \pm 2$) polarized modes.

From a classical viewpoint, introducing such vector and scalar gravitational fields is challenging. If vector and/or scalar gravitational fields exist, they must be sourced by vector and scalar components

incorporated in the stress-energy tensor $T_{\mu\nu}$ on the RHS of Eq. 1.5. To do so, we must force the vector and scalar terms into being components of a tensor and transforming like a tensor, which is mathematically restrictive. Moreover, as the GWs leave the source and propagate in vacuum, the vector and scalar terms must also be incorporated in the Einstein tensor $G_{\mu\nu}$ on the LHS of Eq. 1.5. Thus, searching for vector and scalar polarizations might lead to modified, more general versions of the EP, EFE and GR that change spacetime $G_{\mu\nu}$ to support vector and scalar polarizations.

1.3 Detector response and Antenna patterns

The strain produced by an incoming GW is detected through laser phase shifts (Eq. 1.8) resulting from slight changes in lengths of the arms (Fabry-Perot cavities) [34] of the GW detectors (Figure 1.5).

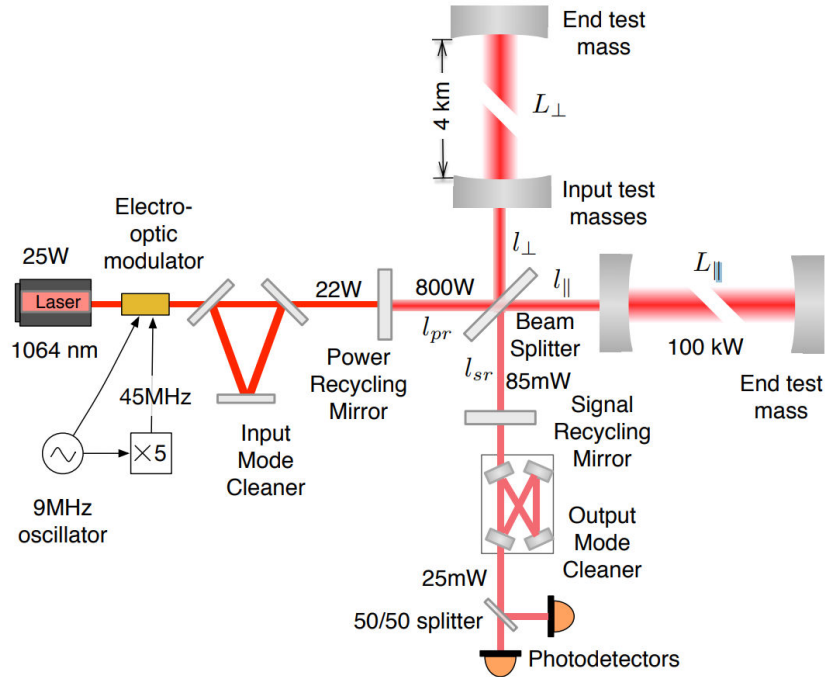


Figure 1.5: Layout of an Advanced LIGO detector [34].

The phase ϕ of the laser depends on the laser frequency k and the length of the detector arm l and can be given as

$$kl = \frac{2\pi l}{\lambda} = \phi \quad (1.7)$$

The laser phase shifts $\delta\phi$ are a function of the change in the detector arm length δl and the laser frequency fluctuations $\delta\lambda$

$$\delta\phi = \frac{2\pi}{\lambda}\delta l - \frac{2\pi l}{\lambda^2}\delta\lambda \quad (1.8)$$

The common arm (CARM) response of a GW detector (ΔL_+) in Eq. 1.9 is highly sensitive to $\delta\lambda$ and used to generate feedback to correct for laser frequency fluctuations (Eq. 1.9).

$$\Delta L_+ = \frac{1}{2}(\Delta l_x + \Delta l_y) \quad (1.9)$$

where l_x and l_y are the lengths of the detector arms [34].

On the other hand, the differential arm (DARM) response of the GW detector (ΔL_-) in Eq. 1.10 measures the differential displacement of the detector arm lengths, cancels $\delta\lambda$, and is ideal for detecting GW signals (Eq. 1.10) [34].

$$\Delta L_- = \frac{1}{2}(\Delta l_x - \Delta l_y) \quad (1.10)$$

The GW detectors measure the dimensionless strain

$$h = \frac{\Delta L_-}{L} \quad (1.11)$$

where L is the length of the GW detector arms (4 km for LIGO-like GW detectors).

DARM response of a single detector

As different polarization modes have different geometric effects on the stretching and squeezing of spacetime (Figure 1.2), the GW detectors respond differently to each polarization mode.

The strain produced by a GW metric perturbation h_{ab} in the DARM response of a GW detector D is given as

$$h_D(t) = \sum_A \frac{1}{2}(d_x^a d_x^b - d_y^a d_y^b) e_{ab}^A h_A(t, x_D) = \sum_A F_A^D h_A(t, x_D) \quad (1.12)$$

where d_x and d_y are the spatial unit vectors along the detector arms and we sum over repeated spatial indices a and b . Although these spatial vectors are also a function of time due to the motion of Earth with respect to the fixed stars, they can be approximately treated as constants for transient

CBC signals that last for a few seconds. $h_A(t, x_D)$ represents the amplitude of linear polarization $A \in [+, \times, x, y, l, b]$.

These linear polarization amplitudes ($h_A(t)$'s) are determined by non-trivial combinations of source dynamics, matter-gravity coupling and vacuum structure of a theory [13]. In the case of CBCs with tensor modes only as predicted by GR, h_+ and h_\times are the only non-zero components and can be completely specified in terms of the binary masses, spins, and the orbital orientation of the source with respect to the line of sight (more in section 2.1).

The F_A^D represent the detector response (also called antenna pattern) of a detector D to the polarization mode A . The antenna patterns depend only on the local geometry of the GW and the detector, irrespective of the properties of the source [13, 35]. Thus, in the detector frame

$$F_A^D \equiv F_A^D(\psi, \theta, \phi) \quad (1.13)$$

where ψ is the polarization angle of the incident plane wave GW radiation from the source and (θ, ϕ) are the polar and azimuthal angles of the source location with respect to the detector.

Figure 1.6 shows the local geometry of an incoming GW and a GW detector in the detector's frame of reference. In this figure d_x and d_y represent unit vectors along the arms of the detector and w_z represents the line of sight from the detector to the source (opposite to the direction of propagation of the GW) such that $w_z = w_x \times w_y$.

Apart from this figure, we refer to w_z as the direction of propagation of the GW while still using the right-handed coordinate system $w_z = w_x \times w_y$. Therefore, throughout the rest of the thesis, w_x , w_y , and w_z are defined in the opposite direction with respect to that shown in Figure 1.6.

In this section we consider the source location (Figure 1.6) and detector response antenna patterns (Figure 1.7) with respect to the local geometry of a single detector. Thus, we define w_x , w_y , w_z and ψ in the detector's frame such that w_x and w_y is closely aligned with d_x and d_y respectively.

However, in the context of a network of detectors (in all following sections), we do not reference w_x , w_y , w_z and ψ with respect to any one detector. Instead, we define our coordinate system (and specifically w_x , w_y , w_z and ψ) with respect to the celestial coordinate system such that w_x points towards the celestial north pole. Thus, for a network of detectors in the next section, we use right ascension and declination (α, δ) instead of detector frame polar and azimuthal angles (θ, ϕ) to describe the source location.

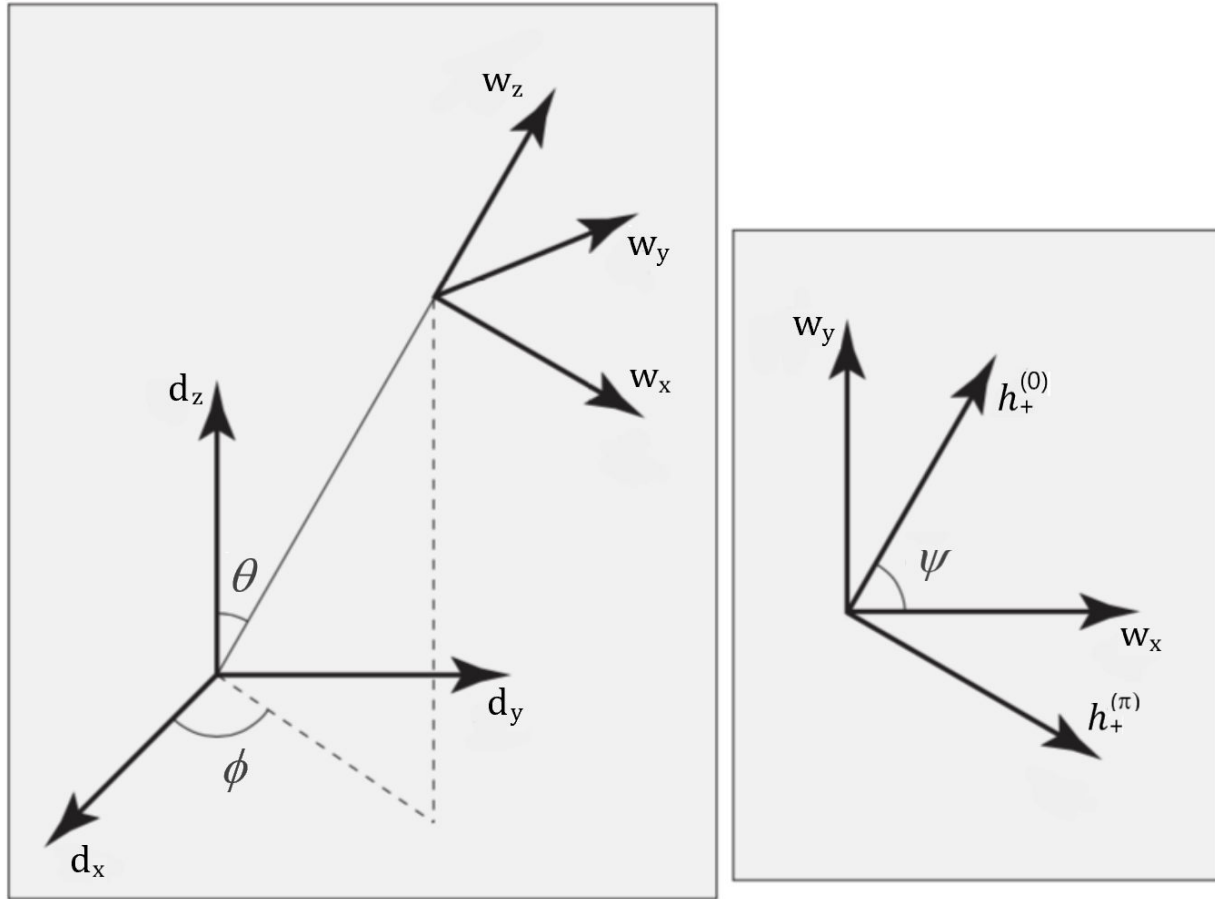


Figure 1.6: The local geometry of an incoming GW signal and a GW detector (left) and the GW polarization axis observed along the line of sight from the detector to the source (right) [35] in the detector's frame of reference. Here d_x and d_y represent unit vectors along the arms of the detector, w_z represents the line of sight from the detector to the source (opposite to the direction of propagation of the GW) such that $w_z = w_x \times w_y$. The source location with respect to the detector is specified by the polar and azimuthal angles (θ, ϕ) . When observed along the line of sight from the detector to the source (right), ψ is the polarization angle between w_x and $h_+^{(0)}$, where $h_+^{(0)}$ and $h_+^{(\pi)}$ are the directions along which space is stretched for the plus polarization in phase 0 and phase π respectively.

The antenna patterns F_A^D (Eq. 1.13) for a single detector in the detector's frame of reference for different polarization modes A are shown in Figure 1.7. The antenna response F_A^D depend heavily on the sky location of the source with respect to the detector.

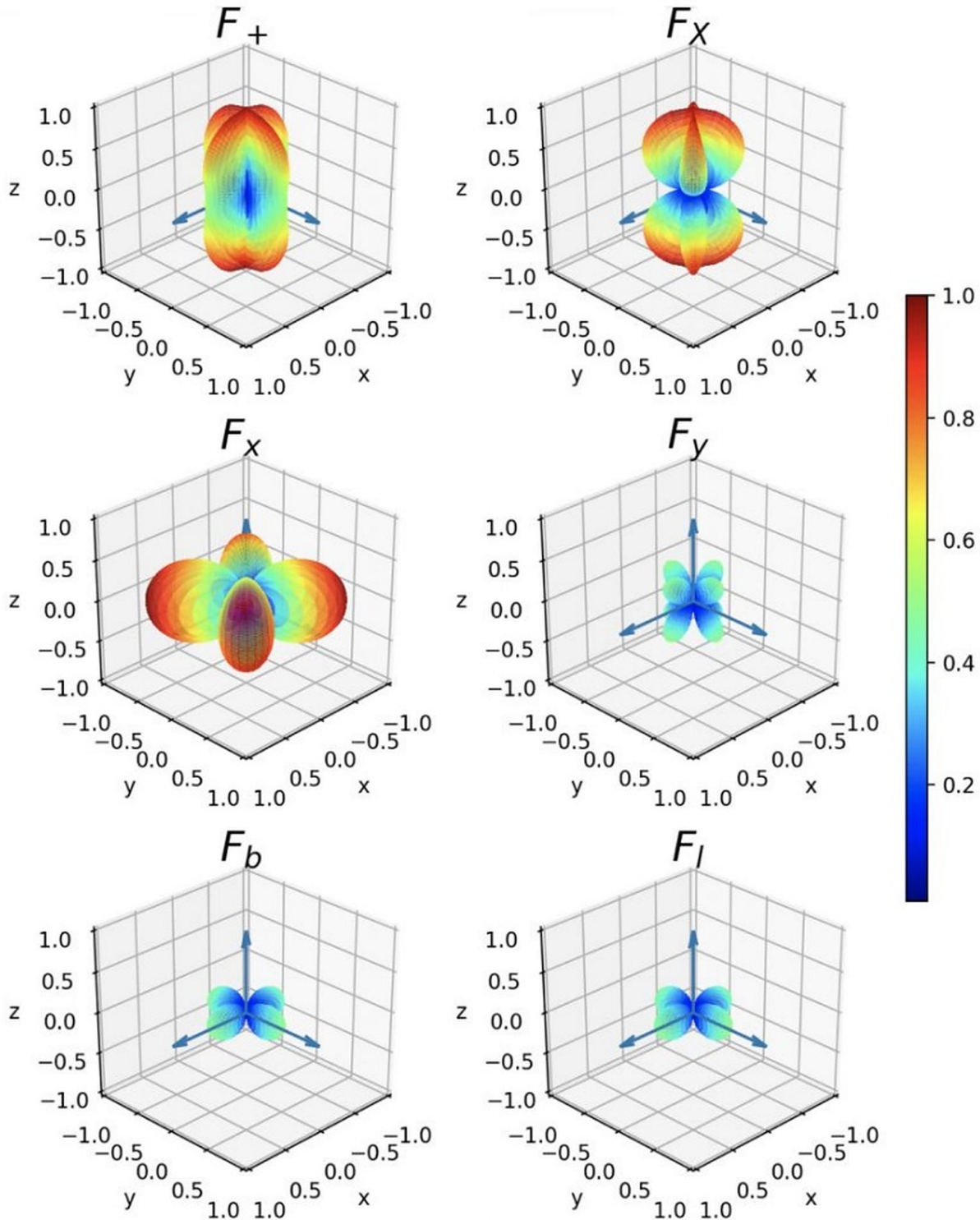


Figure 1.7: Antenna patterns for a single detector in detector's frame of reference for different polarization modes $A \in \{+, \times, x, y, l, b\}$. The blue vectors in the x-y plane depict the spatial unit vectors d_x and d_y along the detector arms. The x, y, and z coordinates specify the sky location of the source with respect to the detector in the detector's reference frame. The radial distance from origin, which is redundant with the color map, quantifies the detector response F_A^D for polarization mode A. Note that the detector DARM response is significantly weaker for scalar polarization modes [32].

Thus, a specific sky location generates different detector strain amplitudes $h_D(t)$ at a detector D for each F_A^D (Eq. 1.12 and Figure 1.7).

There are five non-degenerate polarizations A , namely $+$, \times , x , y , and either l or b , and five possible values of F_A^D for these non-degenerate polarizations A . Since the antenna patterns of the polarization modes are different, we need non-co-oriented detectors sensitive to different linear combinations of polarization modes to distinguish between them. Thus, we require strain data from five non-co-oriented detectors, which would be sensitive to different linear combinations of polarizations, to disentangle the polarization content of transient GWs.

However, in this thesis, we are only concerned with the tensor, vector, or scalar polarizations. This allows us to group the $+$ and \times modes (the x and y modes) into a single variable quantifying the extent of tensor (vector) polarization. Thus, we expect to be able to resolve tensor, vector, and scalar polarization degeneracies with less than five non-co-oriented detectors.

1.4 Ground-based detector network

To disentangle GW polarization content, we are interested in the sensitivity of a network of detectors and its ability to distinguish different polarizations. In this thesis, we simulate five ground-based GW detectors, including presently available detectors LIGO-Hanford, LIGO-Livingston, Virgo, under construction detector KAGRA, and the detector available in the near future LIGO-India (Figure 1.8).

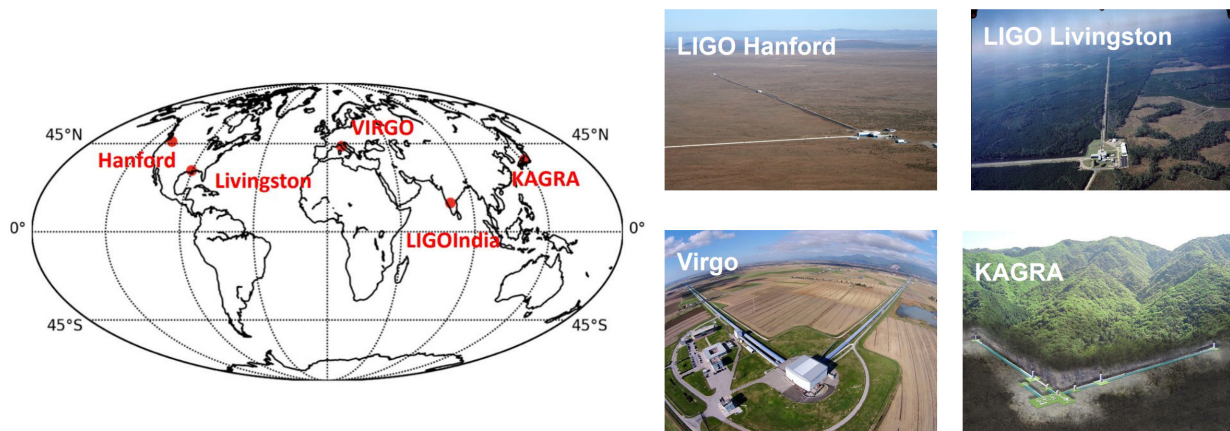


Figure 1.8: Five GW detectors, including presently available detectors LIGO-Hanford, LIGO-Livingston, Virgo, under construction detector KAGRA, and the detector available in the near future LIGO-India [32, 36].

The sensitivity of the network to different polarizations can be quantified by an overlap factor. The overlap factor (Figure 1.9) is a normalized inner product that compares the effective vector or scalar

network sensitivity to the tensor network sensitivity [13]. It is given as

$$\mathcal{F}_{H/t}(\alpha, \delta) = \frac{\vec{F}_H(\alpha, \delta) \cdot \vec{F}_t(\alpha, \delta)}{\vec{F}_t(\alpha, \delta) \cdot \vec{F}_t(\alpha, \delta)} \quad (1.14)$$

where the effective response $\vec{F}_H(\alpha, \delta)$ for each polarization $H \in \{t, v, s\}$ for a sky location (α, δ) and a set of N detectors is given as

$$\vec{F}_H(\alpha, \delta) \equiv (|F_H^1(\alpha, \delta)|, \dots, |F_H^N(\alpha, \delta)|), \quad (1.15)$$

and for any detector D among the N detectors

$$|F_t^D(\alpha, \delta)| \equiv \sqrt{F_+^D(\alpha, \delta)^2 + F_\times^D(\alpha, \delta)^2}, \quad (1.16)$$

$$|F_v^D(\alpha, \delta)| \equiv \sqrt{F_x^D(\alpha, \delta)^2 + F_y^D(\alpha, \delta)^2}, \quad (1.17)$$

$$|F_s^D(\alpha, \delta)| \equiv \sqrt{F_l^D(\alpha, \delta)^2 + F_b^D(\alpha, \delta)^2} = \sqrt{2}|F_l^D(\alpha, \delta)|. \quad (1.18)$$

The average response of the network over all sky locations (Figure 1.9) is worse for scalar polarization modes than it is for vector ones [13, 32]. This is consistent with the fact that each detector is individually less sensitive to scalar modes (Figure 1.7). Averaging over all sky locations, there is no significant difference in network sensitivity between vector and tensor polarization modes [13].

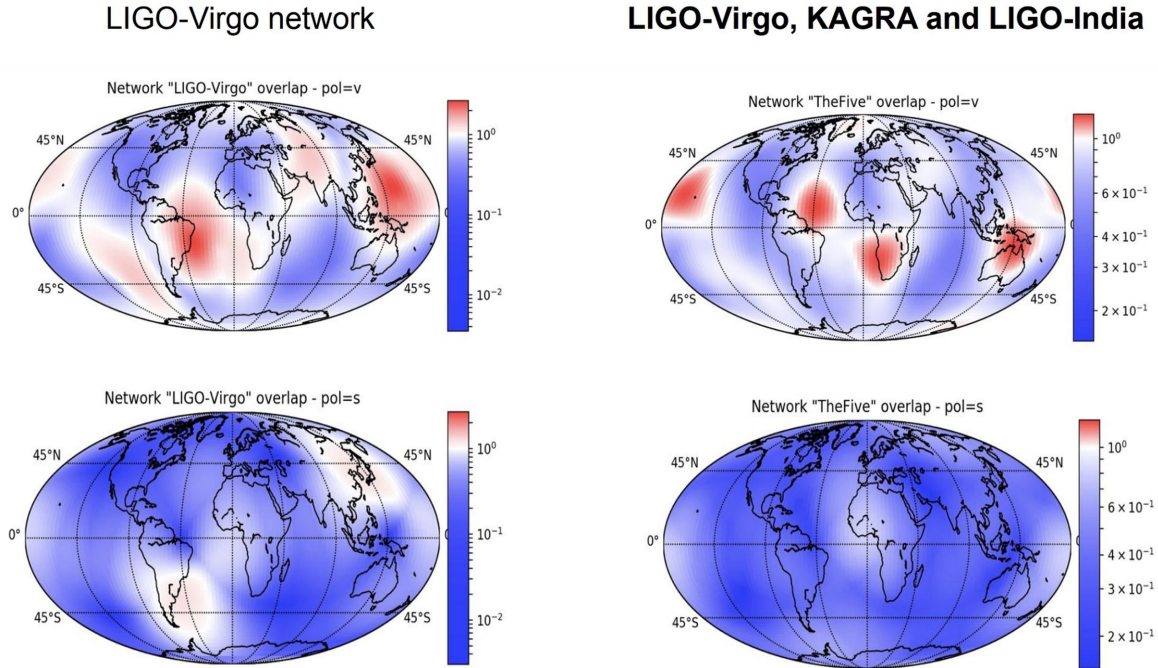


Figure 1.9: Overlaps for the effective antenna patterns of the three detector (LIGO-Virgo) and the five detector (LIGO-Virgo, KAGRA and LIGO-India) networks. The top plots compare the vector to tensor overlap factor (\mathcal{F}_v/t), and the bottom plots compare the scalar to tensor overlap factor (\mathcal{F}_s/t). Red (blue) color marks regions for which the effective non-tensor response is greater (less) than the tensor response. That is, the network of detectors is more sensitive to non-tensor polarization modes in the redder regions. A map of the Earth is overlaid for reference under the assumption that the location of the source is well-defined in geographic coordinates for BBH transient GW signals that last for a few seconds [13, 32].

However, even if we have a network of five detectors in the near future, data from all detectors might not be available for a particular observation. This is because individual GW detectors have duty factors of 60-80%, which quantify the fraction of time a detector is acquiring data. Thus, a network of GW detectors has a network duty factor, quantifying the fraction of time for which different combinations of detectors are acquiring data. As an example, Figure 1.10 shows the duty factor for the network of detectors acquiring data during the third LIGO observational run (O3) [37].

In the subsequent sections, the existence of such a network duty factor motivates us to consider random combinations of three or four detectors in order to determine the polarization detection sensitivity for a GW observation when only three or four detectors out of a five GW detector network are acquiring data.

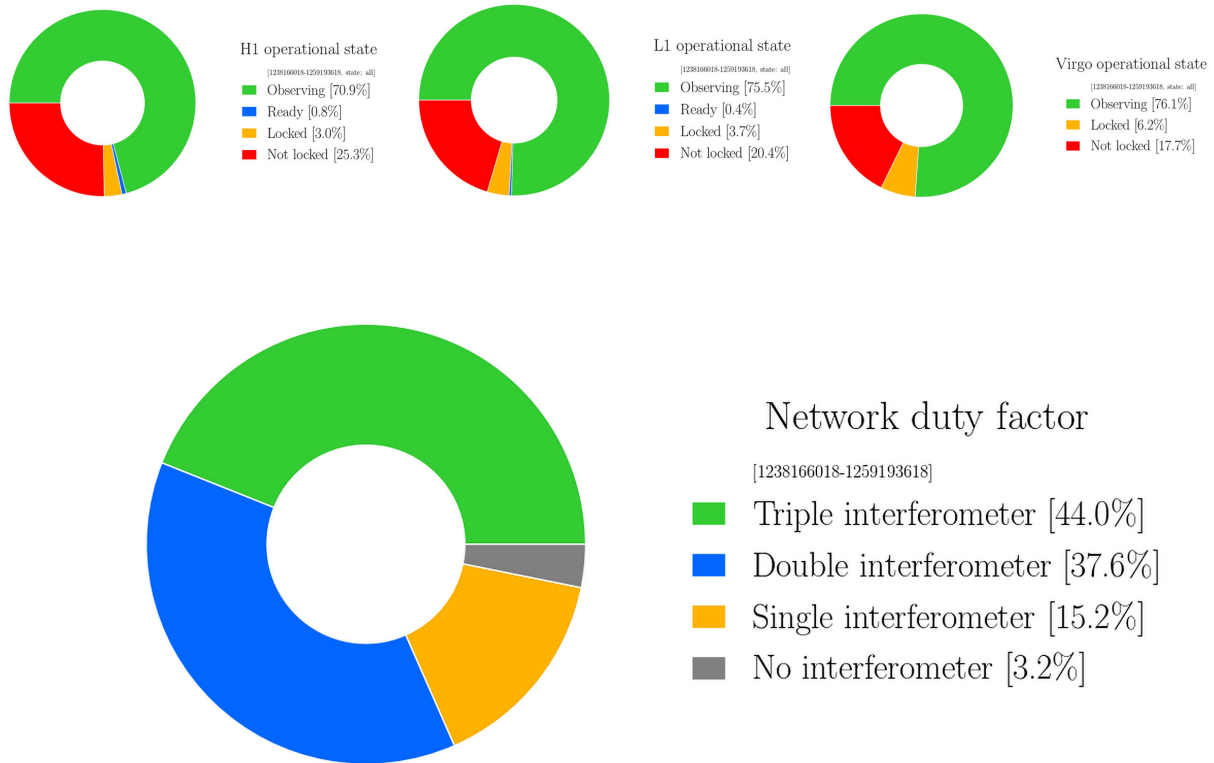


Figure 1.10: Duty Factors for individual detectors and the Network duty factor for the LIGO-Virgo detector network used in the third LIGO Observational Run (O3) [37].

Chapter 2

Methods

2.1 Generating BBH Tensor-Vector-Scalar (tvs) polarized GW waveforms

We generate BBH GW waveforms inspired by numerical relativity to model the BBH merger. The waveforms are a part of the LALsimulation package and the inspiral is modeled by the waveform approximant IMRPhenomPv2 [38], which assumes tensor polarizations (Figure 2.1). IMRPhenomPv2 is also capable of modelling spin-orbit precession. However, for the purpose of our study, we assume that the BBHs are spinless.

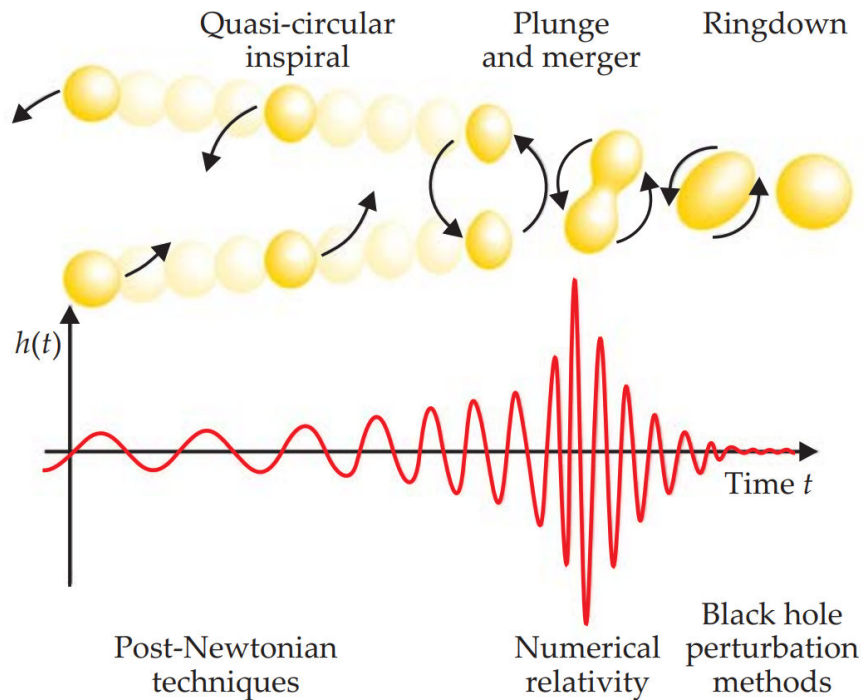


Figure 2.1: The inspiral, merger and ringdown phase of a BBH merger and the corresponding tensor polarized GW waveform ($h(t)$). Post-Newtonian perturbation methods are used to model the early-inspiral phase. However, these methods break down for the late-inspiral and merger phases and waveforms based on numerical relativity (modeled through waveform approximants such as IMRPhenomPv2) must be employed.

The waveform approximant models the general relativistic GW BBH signal using the following simulated intrinsic (to the source) and extrinsic (relative to the observer) parameters.

Symbol	Parameter	Type
m_1	Mass of primary black hole [M_\odot]	Intrinsic
m_2	Mass of secondary black hole [M_\odot]	Intrinsic
\vec{s}_1	Spin vector of primary black hole	Intrinsic
\vec{s}_2	Spin vector of secondary black hole	Intrinsic
α	Right Ascension of Source [rad]	Extrinsic
δ	Declination of Source [rad]	Extrinsic
d_L	Luminosity distance of Source [Mpc]	Extrinsic
i	Inclination angle of Source w.r.t. observer [rad]	Extrinsic
ψ	Polarization angle [rad]	Extrinsic
t_c	Time at coalescence [GPS time in sec]	Extrinsic
ϕ_c	Phase at coalescence [rad]	Extrinsic

Table 2.1: Table of intrinsic and extrinsic parameters used by the waveform approximant to generate the general relativistic GW signal of a BBH merger.

The waveform approximant returns the amplitudes of linear polarizations h_+ and h_\times for the tensor + and \times polarizations respectively.

$$h_+(m_1, m_2, \vec{s}_1, \vec{s}_2, \alpha, \delta, d_L, i, \psi, t_c, \phi_c) \quad (2.1)$$

$$h_\times(m_1, m_2, \vec{s}_1, \vec{s}_2, \alpha, \delta, d_L, i, \psi, t_c, \phi_c) \quad (2.2)$$

For a general relativistic signal, the only non-zero polarization amplitudes h_+ and h_\times of the inspiraling BBH merger take the form

$$h_+ = \frac{h_0(t)}{2} (1 + \cos i^2) \cos \Phi(t), \quad h_\times = h_0(t) \cos i \sin \Phi(t) \quad (2.3)$$

where $h_0(t)$ is the overall, time dependent amplitude for the tensor-only GW, $\Phi(t)$ is the signal's phase (which encodes information about the masses and spins of the source) and i is the inclination angle between the angular momentum (\vec{L}) normal to the orbital plane and the observer's line of sight (\hat{n}) [39].

Since model-independent knowledge of the true vector and scalar polarized GW waveforms is limited [12], we use h_+ and h_\times to create vector and scalar polarization waveforms by defining $\vec{\lambda} = (\lambda_t, \lambda_v, \lambda_s)$ parameters.

$$\vec{h}_+ \equiv \lambda_t h_+(m_1, m_2, \vec{s}_1, \vec{s}_2, \alpha, \delta, d_L, i, \psi, t_c, \phi_c) \quad (2.4)$$

$$\bar{h}_\times \equiv \lambda_t h_\times(m_1, m_2, \vec{s}_1, \vec{s}_2, \alpha, \delta, d_L, i, \psi, t_c, \phi_c) \quad (2.5)$$

$$\bar{h}_x \equiv \lambda_v h_+ \quad (2.6)$$

$$\bar{h}_y \equiv \lambda_v h_\times \quad (2.7)$$

$$\bar{h}_l \equiv \lambda_s h_+ \quad (2.8)$$

with the constraints

$$2\lambda_t + 2\lambda_v + \lambda_s = 1 \quad (2.9)$$

$$\lambda_t, \lambda_v \in [0, 0.5]; \quad \lambda_s \in [0, 1] \quad (2.10)$$

where λ_t , λ_v and λ_s quantify the fraction of tensor, vector and scalar polarization components present in the GW signal.

Since the detector responses to the two different scalar polarizations l and b only differ in a minus sign and are indistinguishable, we include only one of the two scalar polarizations for our analysis.

It is important to note that through the above definition, we assume that the vector and scalar polarization waveforms are similar to the tensor polarization waveform and only differ from it in amplitude and phase. Although this assumption is known to be false, it compels us to use only the geometrical effect of the GW in the non-co-oriented detector network, instead of a non-tensor waveform template, in order to distinguish between polarization modes. Thus, it represents a near worst case scenario for quantifying and placing upper limits on the detection sensitivity of the vector and scalar polarization admixtures in GW radiation.

Waveform plots

We simulate BBH tvs polarized GW signal using the injection parameters in Table 2.2. The randomly chosen GPS time corresponds to Jan 1, 2026 when we look forward to observing data from five ground-based GW detectors. Note that the common t_c for all the GW injections is not a problem in our simulated study as we analyse each GW injection as a separate event.

We generate waveforms starting from frequencies above 20 Hz (Figure 2.2) as the LIGO detectors are only sensitive to GW with frequencies higher than 20 Hz and waveforms in lower frequency regions are long and time-consuming to generate.

The time domain waveforms $\bar{h}(t)$ in Figure 2.2 highlight the inspiral, merger and ringdown phase of the BBH coalescence. The frequency domain waveforms $\bar{h}(f)$ fall with increasing frequency because the BBH spends more time radiating GW at lower frequencies during the inspiral than it spends radiating GW at higher frequencies during the merger and ringdown phase. The magnitude versus frequency plots highlight the local frequency maxima at which the ringdown (broad Lorentzian) occurs.

Symbol	Parameter	Value
m_1	Mass of primary black hole [M_\odot]	36.
m_2	Mass of secondary black hole [M_\odot]	29.
α	Right Ascension of Source [rad]	1.37
δ	Declination of Source [rad]	-1.21
d_L	Luminosity distance of Source [Mpc]	170.
θ_{jn}	Inclination angle [rad]	0.4
ψ	Polarization angle [rad]	2.66
t_c	Time at coalescence [GPS time in sec]	1451260818 (Jan 1, 2026)
ϕ_c	Phase at coalescence [rad]	1.3

Table 2.2: Table of intrinsic and extrinsic general parameters used to generate the BBH tvs polarized GW signal.

Note that in Table 2.1 the inclination angle (i) is the angle between angular momentum (\vec{L}) normal to the orbital plane and the observer's line of sight (\hat{n}). However, in the presence of spin orbit precession, \vec{L} is not constant and the corrected inclination angle (θ_{jn} in Table 2.2) is calculated with respect to the total angular momentum (\vec{J}) instead.

For the purpose of this thesis, $i = \theta_{jn}$ since the simulated BBHs are spinless.

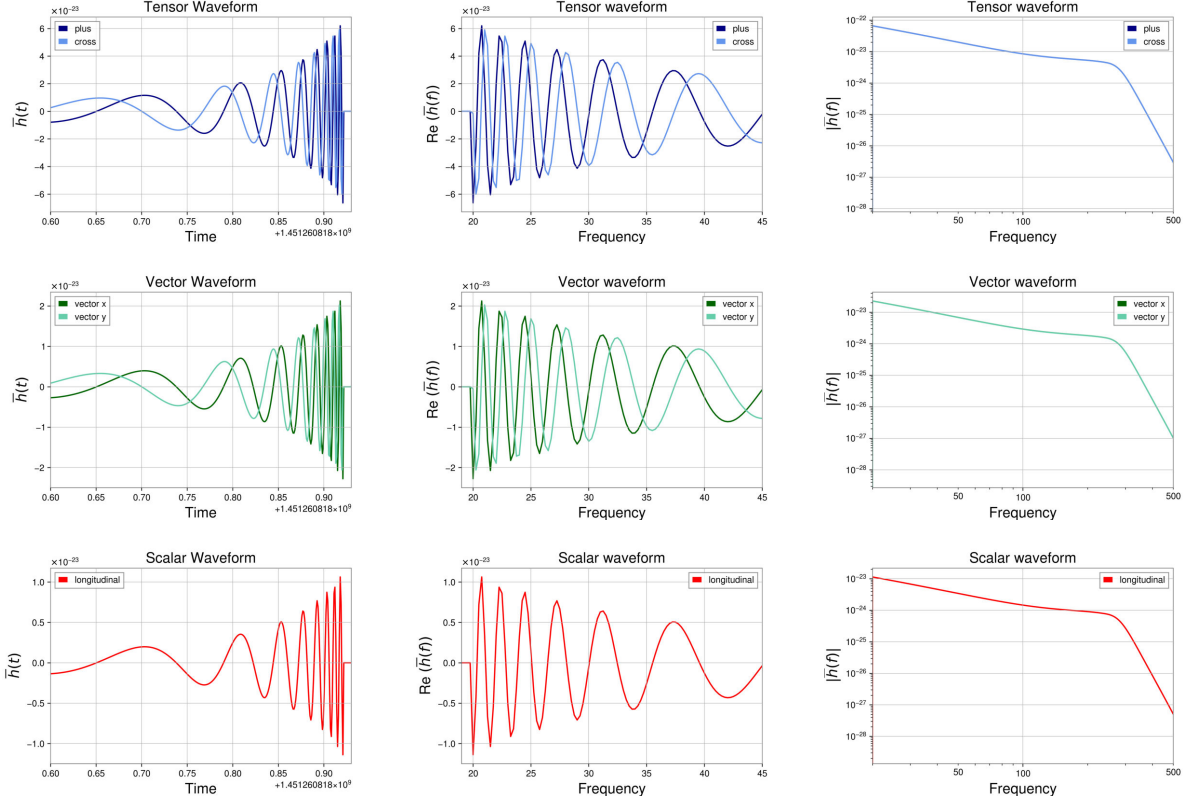


Figure 2.2: The time domain waveforms (left), frequency domain waveforms (middle), and magnitudes (right) of the tensor, vector and scalar polarization components (the three rows respectively) of the BBH tvs polarized GW signal as defined by the general parameters in Table 2.2 and the $\vec{\lambda}$ parameters $\lambda_t = 0.35$, $\lambda_v = 0.12$ and $\lambda_s = 0.06$.

Sanity check for waveforms

Using simulated BBH tvs polarized GW signal, we see that the vector x and scalar l waveforms closely follow the tensor $+$ waveform while the vector y waveform closely follows the tensor \times waveform (Figure 2.3). The vector \bar{h}_x and scalar \bar{h}_l amplitudes differ from the tensor \bar{h}_+ amplitude by factor of λ_v and λ_s respectively. The vector \bar{h}_y amplitude differs from the tensor \bar{h}_\times amplitude by factor of λ_v . This is consistent with our definition of the $\vec{\lambda}$ parameters.

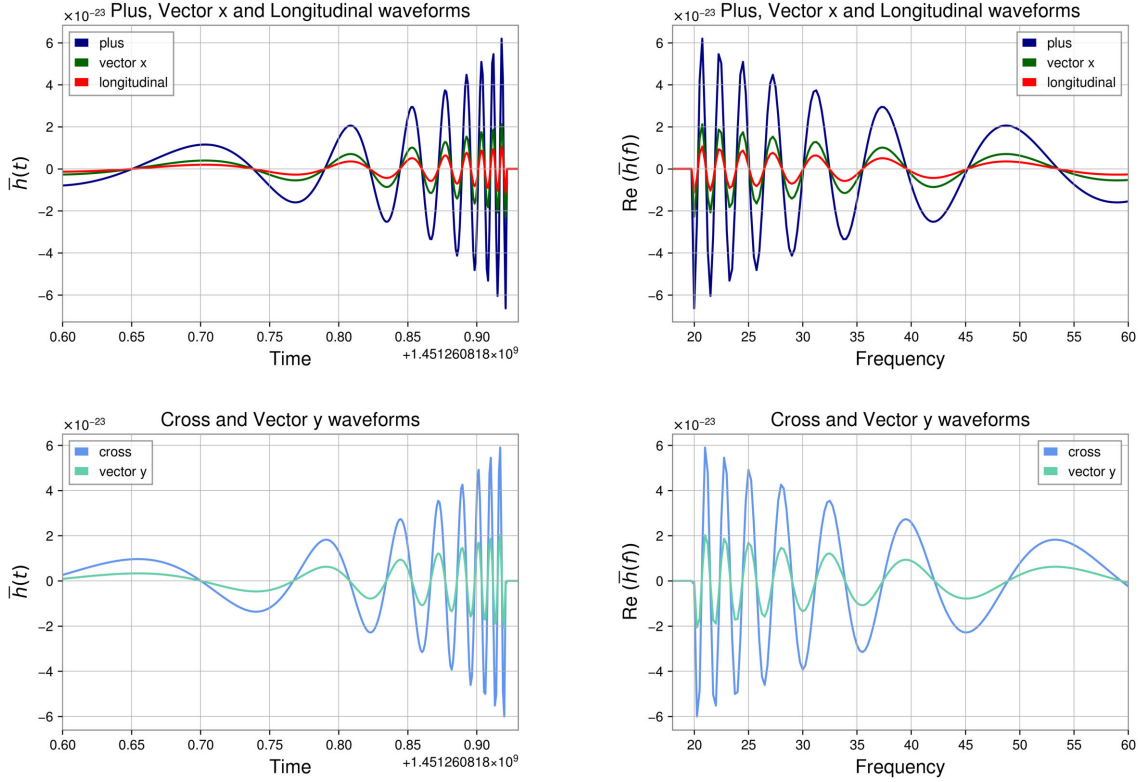


Figure 2.3: The time (left) and frequency (right) domain waveforms for the polarization components of the BBH tvs polarized GW signal generated in Figure 2.2. The $\vec{\lambda}$ parameter values are $\lambda_t = 0.35$, $\lambda_v = 0.12$ and $\lambda_s = 0.06$. As per our definition, the vector \bar{h}_x and scalar \bar{h}_l amplitudes differ from the tensor \bar{h}_+ amplitude by factor of λ_v and λ_s respectively. The vector \bar{h}_y amplitude differs from the tensor \bar{h}_\times amplitude by factor of λ_v .

Next, we generate four different BBH tvs polarized GW waveforms using the general parameter in Table 2.2 and the different $\vec{\lambda}$ parameter values given in Table 2.3.

Waveform Polarizations	λ_t	λ_v	λ_s
Almost equal tvs	0.2	0.15	0.3
High Tensor	0.35	0.12	0.06
High Vector	0.16	0.3	0.08
High Scalar	0.05	0.15	0.6

Table 2.3: Table of different values of $\vec{\lambda}$ parameters used to generate four different BBH tvs polarized GW waveforms.

Figure 2.4 shows the four different BBH tvs polarized GW signals. The signals have different admixtures of tensor, vector and scalar polarization components (given in Table 2.3). The amplitudes

of the tensor, vector and scalar waveforms change as we change the $\vec{\lambda}$ parameters. This is consistent with our definition of the vector and scalar waveforms (Eqs. 2.4 - 2.8)

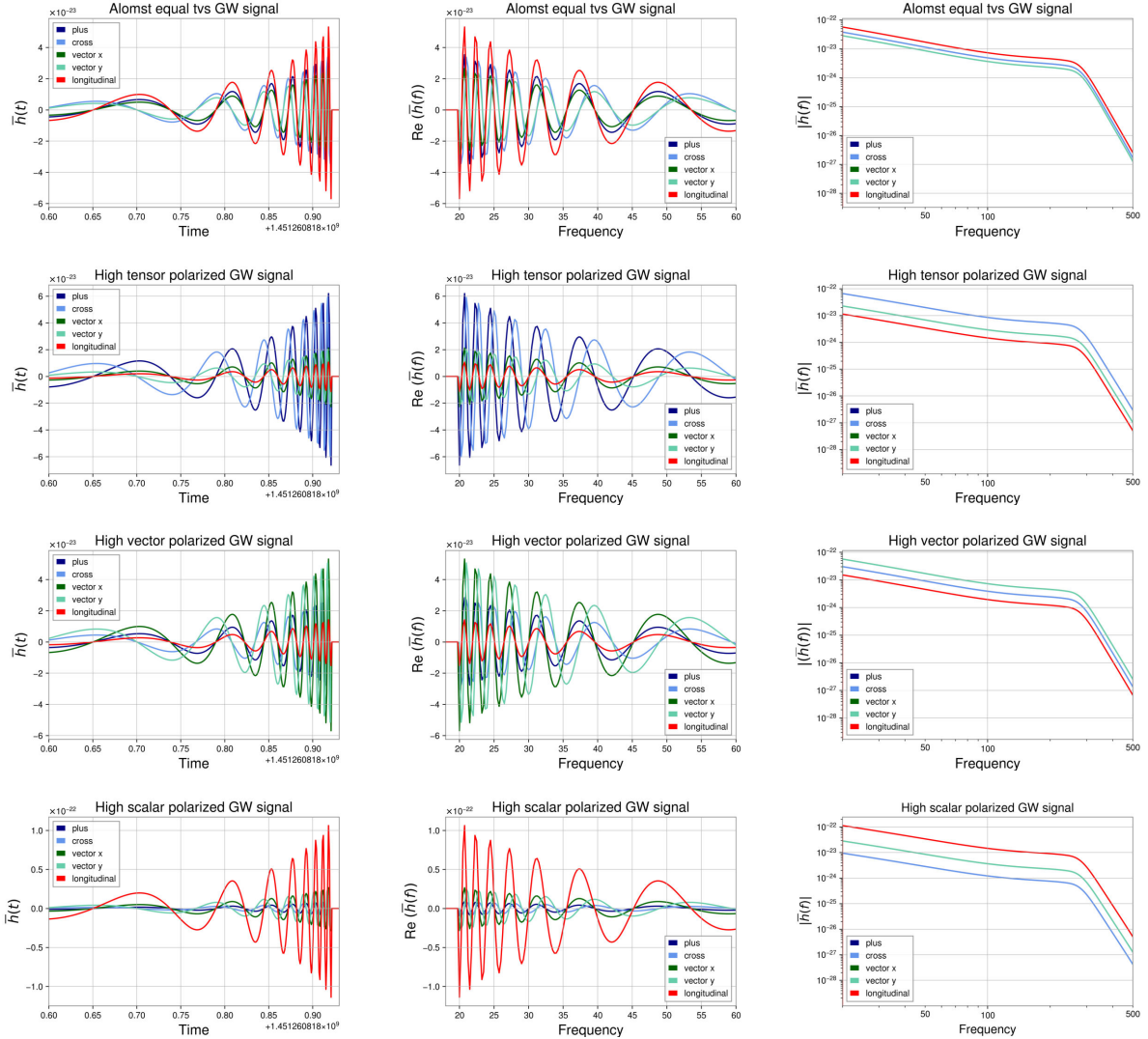


Figure 2.4: The time (left) and frequency (middle) domain waveforms, and magnitudes (right) of the four different BBH tvs polarized GW signals (four rows). The signals have different admixtures of tensor, vector and scalar polarization components (given in Table 2.3) and the same general parameters (given in Table 2.2). The amplitudes of the tensor, vector and scalar waveforms change as we change the $\vec{\lambda}$ parameters. This is consistent with our definition of the vector and scalar waveforms (Eqs. 2.4 - 2.8).

2.2 Simulating detector response

We use the default interferometer list in the GW astronomy Bayesian inference library “Bilby” [40] to simulate the GW detectors LIGO-Hanford (H1), LIGO-Livingston (L1), Virgo (V1) and

KAGRA (K1). The noise curves for the LIGO detectors H1 and L1 are simulated with A+ detector sensitivity [41]. While, the noise curves for V1 and K1 are simulated using Advanced-Virgo and KAGRA design detector sensitivities respectively [40] (Figure 2.5).

The fifth GW detector, LIGO-India (I1), which would be available in the near future, is virtually created using Bilby. For the purposes of our analysis, LIGO India is projected using an A+ detector sensitivity noise curve (Figure 2.5) and its location is the latitude and longitude of Hingoli district, Maharashtra. The latitude, longitude, elevation, and detector arm azimuths used for simulating LIGO-India may be different from the actual design.

We refer to a GW detector's strain equivalent noise spectrum (i.e., the way detector noise manifests in the strain channel) as its noise Amplitude Spectral Density (ASD). The ASDs in Figure 2.5 are sampled at 16 KHz, which is usually used to observe GW signal from binary neutron star mergers at about 3 KHz. However, as we study GW signals from BBH mergers, we downsample our dataset to 2,048 Hz with a Nyquist frequency of 1,024 Hz throughout the thesis in order to increase computational efficiency. We then low pass filter the data below the Nyquist frequency to prevent high frequency noise from leaking into lower frequencies.

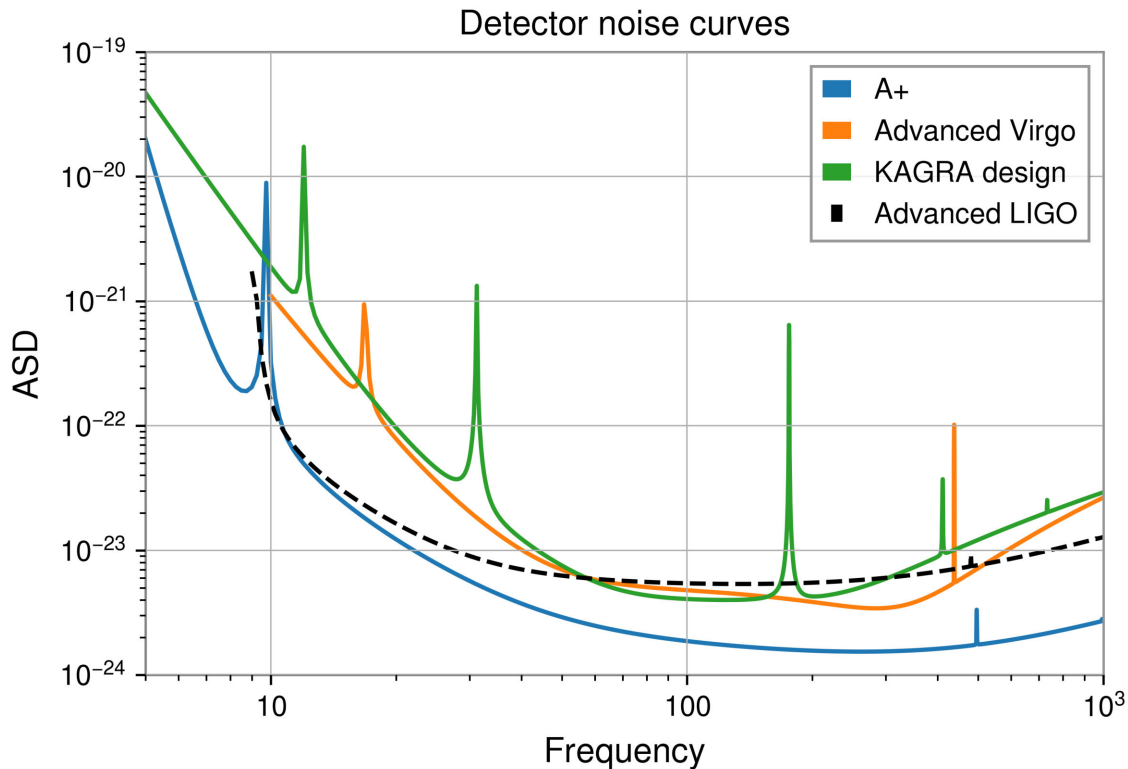


Figure 2.5: The noise Amplitude Spectral Densities (ASDs) for A+ [41], Advanced LIGO [42], Advanced Virgo and KAGRA design detector sensitivities [40] sampled at 16 KHz. The ASDs for detectors H1, L1 and I1 are based on the A+ detector sensitivity, which is significantly better than Advanced-LIGO detector sensitivity. The ASDs for V1 and K1 are based on Advanced Virgo and KAGRA design detector sensitivities respectively.

The sensitivities of these ground-based detectors (Figure 2.5) are limited by the seismic motion of the earth at low frequencies below 10 Hz, by thermal noise at intermediate frequencies and by photon shot noise at high frequencies [42].

The A+ detector sensitivity noise curve (Figure 2.5) takes the Advanced LIGO model further by making modifications to reduce thermal and quantum noise at intermediate and high frequencies [41].

For low frequencies, third generation underground GW detectors with better seismic isolation [43] would be able to detect GW signals down to 2-3 Hz. Since CBCs spend most time in the low frequency regime, GW data from detectors sensitive to lower frequencies would allow detections hours before the merger and give enough response time to observe the coalescence through optical telescopes.

Moreover, the space-based detector LISA [44], which is set to be operational in 2036, would be

able to observe GW signals in the low frequency regime between 10^{-5} and 10^{-1} Hz. At such low frequencies, stellar mass BBHs will be effectively continuous sources and the techniques developed in [23] can be used to study the polarization content of such GWs.

Figure 2.6 shows the noise ASD for the A+ detector sensitivity and the scaled magnitude of GW signals of BBH mergers. The signal magnitude is scaled by a factor of \sqrt{f} in order to place it in the same plot as the noise ASD. The GW signal magnitude falls off as a power law during the inspiral phase, flattens during the merger and forms a knee at the ringdown phase. The ringdown signal is an exponentially damped sinusoid in the time domain and falls off as a broad-peaked Lorentzian in the frequency domain. The waveform data above 130 Hz is overwhelmed by Gibbs noise and is to be ignored.

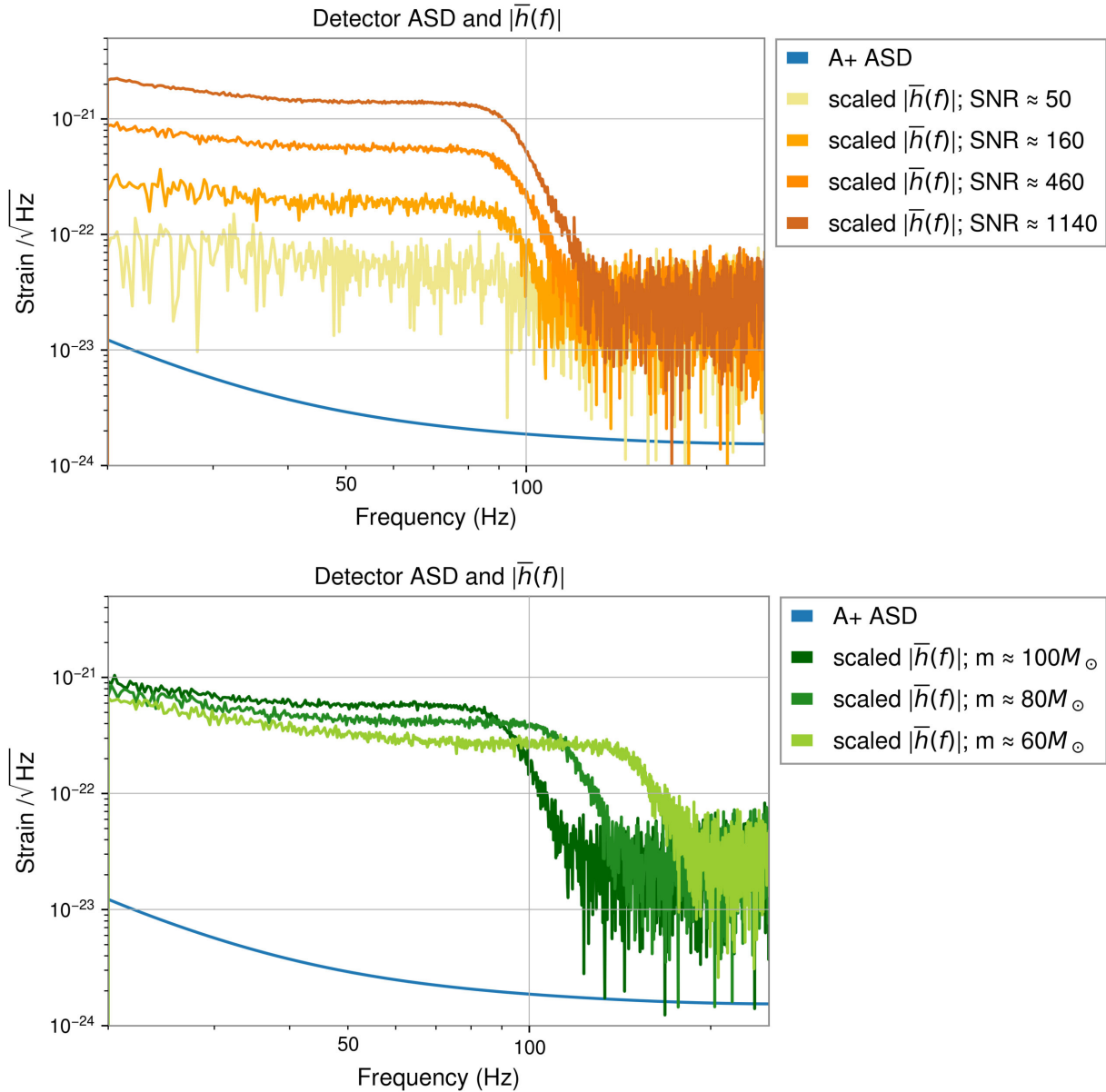


Figure 2.6: The noise ASD for A+ detector sensitivity and the scaled BBH merger GW signal magnitude (scaled $|\bar{h}(f)|$) versus frequency plot for different SNRs with a fixed component masses $m \approx 100M_{\odot}$ (top), and different BBH component masses with a fixed $\text{SNR} \in [100, 200]$ (bottom). The signal magnitude is scaled by a factor of \sqrt{f} in order to place it in the same plot as the noise ASD. The waveform data above 130 Hz is overwhelmed by Gibbs noise and is to be ignored. We observe that BBH with higher masses merge at lower frequencies (bottom).

Next, we inject BBH tvs polarized GW signals with different admixtures of tensor, vector and scalar (tvs) polarizations in the network of the five non-co-oriented GW detectors (using parameters in Table 2.4 and $\vec{\lambda}$ parameters in Table 2.3).

For a GW signal, the detector response for a particular detector depends upon the location of the source with respect to the detector and the polarization composition of the incoming GW signal (Eq. 1.12 and Figure 1.7). Thus, for an incoming GW wave, the detector response differs between the non-co-oriented detectors as the location, polarization angle, and inclination angle of the source changes with respect to different detectors.

As a result, the strain injected in five non-co-oriented detectors due to the same incoming GW signal differs in amplitude and phase (Figure 2.7). We use these differences in amplitudes and phases of the injected strains in our non-co-oriented detectors to resolve degeneracies in the polarization content of an incoming GW wave.

Symbol	Parameter	Value
m_1	Mass of primary black hole [M_\odot]	36.
m_2	Mass of secondary black hole [M_\odot]	29.
α	Right Ascension of Source [rad]	0.99
δ	Declination of Source [rad]	0.88
d_L	Luminosity distance of Source [Mpc]	1 or 30
θ_{jn}	Inclination angle (with spin orbit precession) [rad]	0.4
ψ	Polarization angle [rad]	1.73
t_c	Time at coalescence [GPS time in sec]	1451260818 (Jan 1, 2026)
ϕ_c	Phase at coalescence [rad]	1.3

Table 2.4: Table of intrinsic and extrinsic parameters used in Figure 2.7. Luminosity distance of 1 Mpc simulates the detector response without noise (left column in Figure 2.7) while that of 30 Mpc simulates the detector response where signal is buried in noise (right column in Figure 2.7).

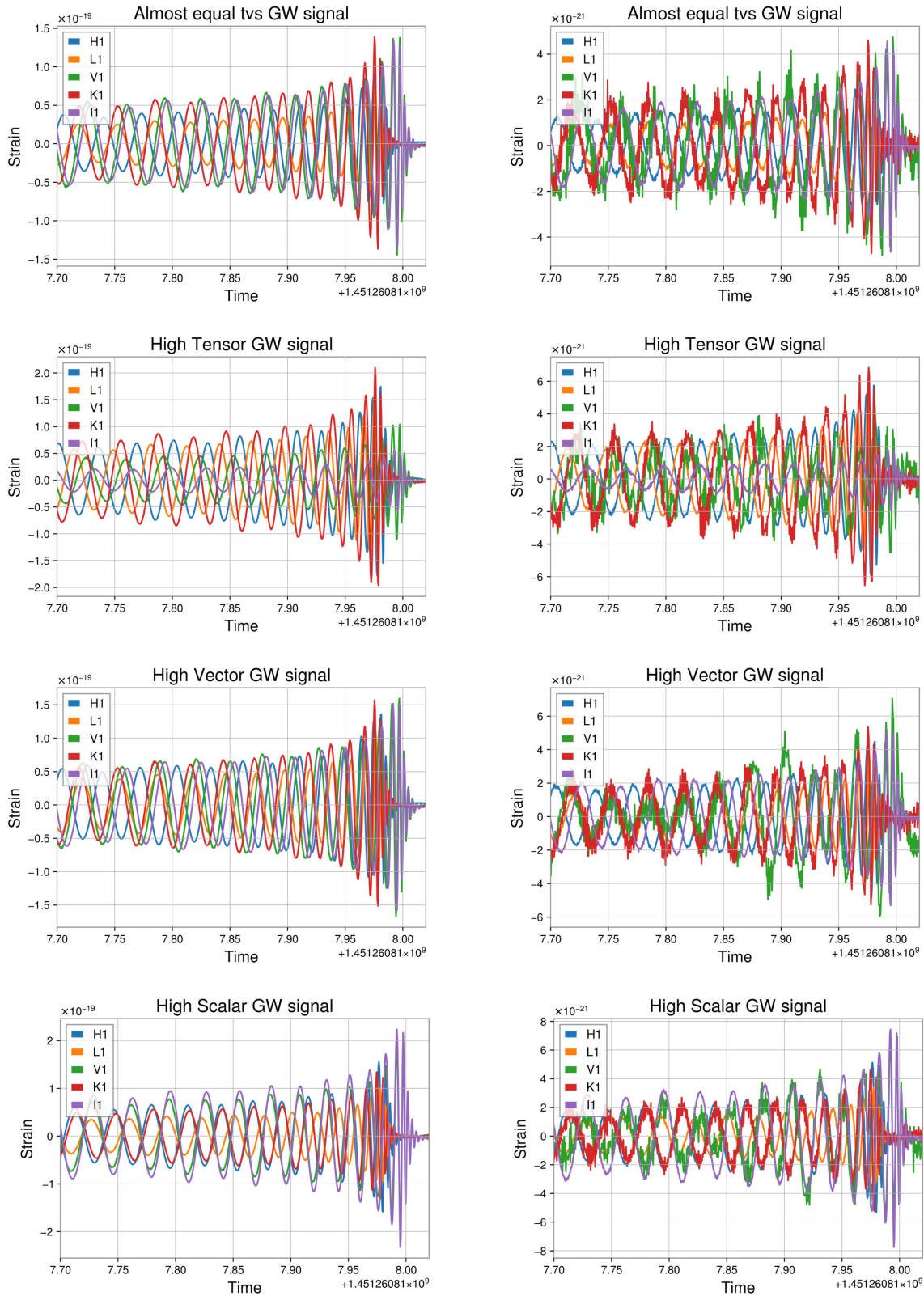


Figure 2.7: The injected time domain strain for five non-co-oriented GW detectors without (left) and with (right) detector noise. Four different BBH tvs polarized GW signals (four different rows) with different admixtures of tvs polarization components were injected in all the five detectors (general parameters given in Table 2.4 and $\vec{\lambda}$ parameters given in Table 2.3). The strain injected in five non-co-oriented detectors due to the same incoming GW signal (in every plot) differs in amplitude and phase.

2.3 Bayesian Inference

We use Bayesian parameter estimation and nested sampling to quantify how well we can retrieve the values of the injected $\vec{\lambda}$ parameters. The $\vec{\lambda}$ parameter values quantify the admixtures of tensor, vector and scalar polarization present in the injected BBH GW signal. By estimating the values of these $\vec{\lambda}$ parameter through Bayesian inference, we place constraints of the detection sensitivity for the admixtures of vector and scalar polarizations.

Bayes theorem gives the posterior probability distribution of parameters $\vec{\theta}$ (any varying parameters such as $\vec{\lambda}, d_L, \alpha, \delta, \psi$), given the data \vec{d} and hypothesis H as

$$p(\vec{\theta}|\vec{d}, H) = \frac{p(\vec{d}|\vec{\theta}, H)p(\vec{\theta}|H)}{Z} \quad (2.11)$$

where H is our hypothesis that GW signal is described by a model such that the signal subtracted from the data gives Gaussian random noise, $p(\vec{d}|\vec{\theta}, H)$ (or L) is the likelihood of the data given the parameters $\vec{\theta}$ and hypothesis H , $p(\vec{\theta}|H)$ are the priors, and the evidence $Z = p(\vec{d}|\vec{H})$ normalizes the RHS such that the posterior probability distribution is 1 when integrated over all parameter space. The evidence Z is estimated numerically as

$$Z = \int_{\Theta} p(\vec{d}|\vec{\theta}, H)p(\vec{\theta}|H)d\vec{\theta} \quad (2.12)$$

where Θ is the complete space of parameters $\vec{\theta}$.

We employ a standard Gaussian noise likelihood L for detector strain data \vec{d} given the parameters $\vec{\theta}$ such that

$$p(\vec{d}|\vec{\theta}, H) \equiv L(\vec{d}|\vec{\theta}) \quad (2.13)$$

and

$$\ln p(\vec{d}|\vec{\theta}, H) = \ln L(\vec{d}|\vec{\theta}) = -\frac{1}{2} \sum_k \left\{ \frac{[d_k - \mu_k(\vec{\theta})]^2}{\sigma_k^2} + \ln 2\pi\sigma_k^2 \right\} \quad (2.14)$$

where k is the frequency bin index, σ^2 is the square of the noise ASD (called noise Power Spectral Density), and $\mu_k(\vec{\theta})$ is the signal in the frequency domain [40] as a function of the extrinsic, intrinsic and $\vec{\lambda}$ parameters.

When our hypothesis H is true and the signal $\mu(\vec{\theta})$ matches the data such that their difference gives Gaussian random noise, the likelihood is large. This, in turn, gives a large posterior probability for those values of $\vec{\theta}$ for which the signal $\mu(\vec{\theta})$ matches the data.

Our dataset \vec{d} is a $16384 \times D$ dimensional vector comprising of the detectors $D \in [1, N = 5]$ and time steps $\in [1, 16384]$ for one second of data. In practice, the signals we observe for BBH mergers are significantly shorter than one second in the detectable frequency regime above 20 Hz (Figure 2.5).

Each data point is correlated in time but in the frequency domain, noise is not correlated between frequency bins (Eq. 2.14). This implies that the signal (which is determined by $\vec{\theta}$ and H) is strongly correlated between the detectors in a deterministic way. However, noise from each of the D detectors is probabilistic and uncorrelated between detectors. Thus, subtracting the correlated signal from the data in Eq. 2.14, leaves us with uncorrelated noise in each of the N detectors.

Due to such uncorrelated and random Gaussian noise, we assume that the data from each of the N detectors are uncorrelated with that from the any other detector. Therefore, we define the probability of our data from a network of detectors as

$$p(\vec{d}|\vec{\theta}, H)_{\text{network}} = \prod_{D=1}^N p(\vec{d}|\vec{\theta}, H)_D \quad (2.15)$$

In practice, however, using the product of individual detector likelihoods to compute the likelihood for a network of detectors is computationally inefficient. Instead, we compute the Bayes theorem likelihood (Eq. 2.11) by exponentiating the sum of the log likelihood (Eq. 2.14) over all detectors.

The priors $p(\vec{\theta}|H)$ we use for Bayesian parameter estimation (Eq. 2.11), are delta functions at the true values for all the fixed parameters such as BBH masses, spins, orientation and polarization angles (θ_{jn}, ψ) , and time and phase at coalescence (t_c, ϕ_c) .

The priors for the $\vec{\lambda}$ parameters span the entire parameter space allowed after imposing the constraints outlined in our definition (Eqs. 2.9, 2.10). The priors are uniform in sky location $(\alpha \in [0, 2\pi]$ and $\sin \delta \in [-1, 1])$.

For a few GW parameter estimations, the polarization angle prior is uniform and periodic $(\psi \in [0, \pi])$ instead of a delta function at its true value (more in the next section).

Ideally, the prior for distance should be uniform in comoving volume in order to account for cosmological effects of the evolution and expansion of the universe. Due to the evolution of the universe, the rate of mergers changes over time with changes in the star formation rate. Also, due to the expansion of the universe, the Euclidean volume changes over time, the observed rate of

mergers changes with time dilation, and the GW signal is redshifted. However, for the purpose of this study, we ignore such cosmological effects since they only affect the prior on distance and have negligible impact on our results. We treat the universe as static and Euclidean.

We note that the choice of a prior that is uniform in Euclidean volume $V = 4\pi d_L^3$ such that $dV = 4\pi d_L^2 d(d_L)$ is computationally inefficient as the sampler spends more time at larger d_L , where signals can be undetectably weak.

To increase the efficiency of our sampler, we define our prior to be uniform in d_L instead. While a prior uniform in d_L is astrophysically and cosmologically incorrect, it makes the sampler converge faster and does not affect our results as long as we work with relatively high SNR (> 20) signals.

We justify this as follows: For such relatively high SNR (> 20) signals in three or more detectors our data are informative, the priors vary smoothly, the likelihood peaks strongly at a particular value of $\vec{\theta}$ and, consequently, our choice of prior should not impact our results.

2.4 Quantifying polarization detection sensitivities

In this thesis, we aim to determine the dependence of GW polarization detection sensitivity on the number of detectors, true values of λ_v and λ_s , SNR, sky location (α, δ) , polarization angle ψ , BBH binary masses, and our choice of the ψ prior distribution.

This is done through Single Event Analysis where the λ_t , λ_v and λ_s posterior probability distributions are extracted from each individual event through a separate evaluation of the posterior.

Table 2.5 shows a list of questions that this thesis explores and our approach towards each of them.

Note that the ‘‘assigned name’’ in Table 2.5 signifies the $\vec{\lambda}$ parameter true values that we are stepping through. For example, the assigned name ‘‘ λ_v posterior’’ means that we step through 11 bins of progressively increasing values of λ_v while λ_s is either randomly selected, as in the case of Tensor-Vector-Scalar (tvs) polarized GWs, or zero as in the case of Tensor-Vector (tv) only GWs.

The first four sets of GW parameter estimations (first four rows of Table 2.5) are performed using a ‘‘fixed’’ ψ prior distribution, where the ψ prior is a delta function at its true value in the Bayesian parameter estimation. If our data are informative, the choice of ψ prior should not have a significant effect on our results. To examine this claim we perform two additional sets of tvs polarized GW parameter estimations (row five and six of Table 2.5) with a ‘‘uniform’’ ψ prior distribution where the ψ prior is uniform and periodic $\in [0, \pi]$ for the Bayesian parameter estimation.

Moreover, Table 2.6 presents additional questions addressed in thesis that require a more elaborate study (a major part of which is left for future work) for conclusive remarks.

We verify that our methods work for different BBH component masses (first row of Table 2.6).

Through the Multiple Event Analysis (second row of Table 2.6), we present an example method which explores the possibility that the fraction of vector and/or scalar polarization content is constant for all GW radiation. This involves the hypothesis that the polarization $\vec{\lambda}$ parameters are shared between different GW detections and are independent of all other parameters and properties of the BBH merger. We then generate joint one-dimensional λ posterior probability distributions for n number of such event by marginalizing over all other parameters.

Polarization	Assigned Name	Approach and Description	Benefits
Tensor -Vector -Scalar (tvs)	λ_v posterior for tvs GWs; fixed ψ prior	528 GW injections for each; (11 λ_v or λ_s true values \times 3 different SNRs \times 16 combinations of 3, 4, or 5 GW detectors).	Explores the dependence of polarization detection sensitivity on λ_v and λ_s true values, the number of detectors, SNR, sky location, and polarization angle.
	λ_s posterior for tvs GWs; fixed ψ prior	Sky location and polarization angles randomly chosen from uniform distributions of $\alpha \in [0, 2\pi]$, $\sin \delta \in [-1, 1]$, and $\psi \in [0, \pi]$.	
Tensor -Vector (tv)	λ_v posterior for tv GWs; fixed ψ prior		
Tensor -Scalar (ts)	λ_s posterior for ts GWs; fixed ψ prior	Prior distribution ψ is a delta function at true value.	
Tensor -Vector -Scalar (tvs)	λ_v posterior for tvs GWs; uniform ψ prior	528 GW injections for each; similar to the above, except	Explores the dependence of polarization detection sensitivity on the choice of ψ prior distribution.
	λ_s posterior for tvs GWs; uniform ψ prior	Prior distribution ψ is uniform and periodic.	

Table 2.5: List of questions explored in the thesis and an outline of our computational approach.

Polarization	Assigned Name	Approach and Description	Benefits
Tensor -Vector -Scalar (tvs)	$\vec{\lambda}$ posteriors for tvs GWs with different BBH masses	9 GW injections; (3 different m_1 and m_2 values \times 3 different SNRs) Prior distribution ψ is a delta function at true value.	Explores the dependence of polarization detection sensitivity on the BBH component masses (more for future work)
	Multiple Event Analysis: Joint $\vec{\lambda}$ posteriors	149 GW injections; (fixed $\vec{\lambda}$ parameters with randomly chosen binary masses (m_1, m_2), and luminosity distance (d_L))	Explores the possibility that there is a constant fraction of vector and/or scalar polarization content in GW radiation (thesis outlines a simple example; more left for future work)

Table 2.6: Additional questions addressed in thesis that require a more elaborate study for conclusive remarks (a major part of which is left for future work). The sky location and polarization angles are randomly chosen from uniform distributions of $\alpha \in [0, 2\pi]$, $\sin \delta \in [-1, 1]$, and $\psi \in [0, \pi]$. Prior distribution ψ is a delta function at its true value in the Bayesian parameter estimation.

Chapter 3

Results

We use the High Throughput Computing (HTC) software HTCondor [45] to run “embarrassingly parallel” Bilby Bayesian parameter estimation “jobs” on the LIGO Caltech computing cluster.

We run multiple sets of 528 HTCondor jobs (outlined the first four rows of Table 2.5). Each set of jobs simulates 33 different GWs in all possible combinations of three, four and five detectors (10 + 5 + 1 detector combinations). The simulation parameters common in all 528 injections are given in Table 3.1. The randomly chosen GPS time corresponds to Jan 1, 2026 when we look forward to observing data from five ground-based GW detectors. Note that the common t_c for all the GW injections is not a problem in our simulated study as we analyse each GW injection as a separate event.

The 33 different GWs have randomly chosen sky location and polarization angles from uniform distributions of $\alpha \in [0, 2\pi]$, $\sin \delta \in [-1, 1]$, and $\psi \in [0, \pi]$. They are further split into 11 simulations of progressively increasing λ_v (or λ_s) values with low ($d_L = 700$ Mpc), medium ($d_L = 195$ Mpc) and high ($d_L = 50$ Mpc) SNR signals and random distribution of the remaining polarization content between scalar (or vector) and tensor polarization components.

Thus, 528 jobs = 16 possible detector combinations \times 3 different SNRs \times 11 λ_v bins $\in [0, 0.5]$ (or 11 λ_s bins $\in [0, 1]$).

Each job runs Bayesian parameter estimation on ONE event and produces posterior probability distributions (Eq. 2.11) for λ_v , λ_s , sky location (α, δ) and luminosity distance d_L with masses, spins, orientation and polarization angles (θ_{jn}, ψ), and time and phase at coalescence (t_c, ϕ_c) fixed at their true value.

The priors used to compute the likelihood (Eq. 2.14) are Bilby’s default prior distributions for the sky location (α, δ) and uniform priors for d_L . The priors for the $\vec{\lambda}$ parameters span the entire parameter space allowed after imposing a constraint prior corresponding to Eq. 2.9. Prior distributions that are delta functions at the true value are used for the mass, spin, orientation and polarization angles (θ_{jn}, ψ), time and phase at coalescence (t_c, ϕ_c) in Table 3.1.

Symbol	Parameter	Value
m_1	Mass of primary black hole [M_\odot]	36.
m_2	Mass of secondary black hole [M_\odot]	29.
\vec{s}_1	Spin vector of primary black hole [M_\odot]	0.
\vec{s}_2	Spin vector of secondary black hole [M_\odot]	0.
θ_{jn}	Inclination angle (with spin orbit precession) [rad]	0.4
ψ	Polarization angle [rad]	random
t_c	Time at coalescence [GPS time in sec]	1451260818 (Jan 1, 2026)
ϕ_c	Phase at coalescence [rad]	1.3

Table 3.1: Table of common parameters in the multiple sets of 528 condor jobs (outlined in Table 2.5) used to simulate 33 different tvs, tv and ts polarized GWs in all possible combinations of three, four and five detectors.

We expect that varying the mass, spin, orientation angle (θ_{jn}), polarization angle (ψ), time and phase at coalescence (t_c , ϕ_c) priors from their delta function distribution in the Bayesian parameter estimation would decrease both the accuracy and precision of our results. However, varying all possible priors is prohibitively computationally intensive and beyond the scope of this thesis.

To verify that our results are not unrealistic, we allow one of these previously fixed priors, namely the polarization angle (ψ) prior, to vary in the Bayesian parameter estimation for a small number of jobs with tvs polarized GWs (outlined in rows five and six of Table 2.5) and quantify the effect of this uniform ψ prior distribution on the polarization detection sensitivity. Figure 3.1 represents an example corner plot for the posterior probability distributions inferred from ONE such Bayesian parameter estimation job for a BBH tvs polarized GW injected in five detectors. It highlights the correlation between the $\vec{\lambda}$ parameters, sky location (α , δ), luminosity distance (d_L), and the polarization angle ψ and projects the one-dimensional λ posteriors. Such one-dimensional λ posteriors are plotted against their respective true parameter values to present our results as “violin” plots in Section 3.1.

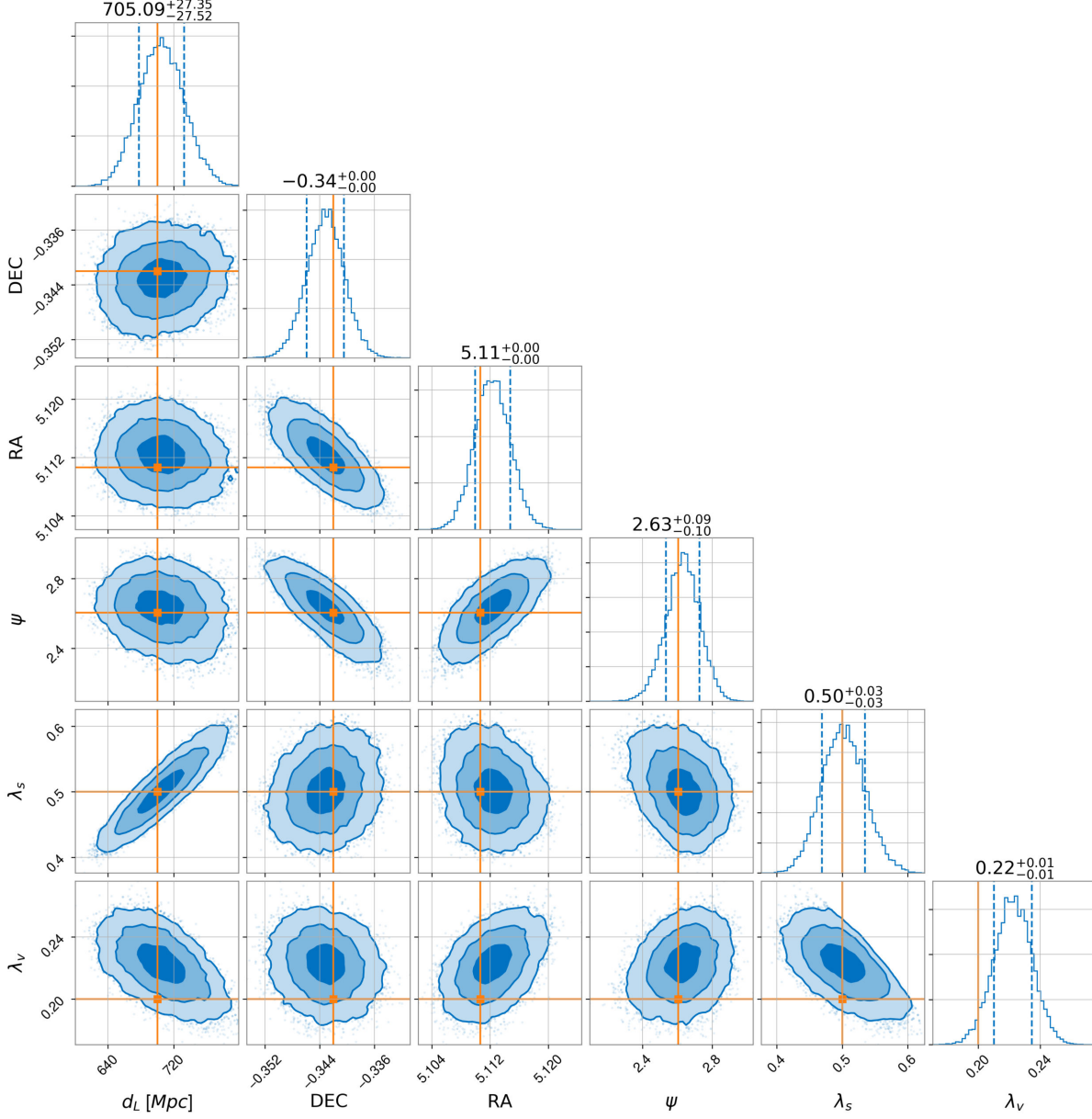


Figure 3.1: Corner plot for one-dimensional projections of λ_v and λ_s , sky location (RA, DEC), luminosity distance (d_L), and polarization angle (ψ) posterior probability distributions recovered through Bayesian parameter estimation. The BBH tvs polarized GW with $\lambda_t = 0.05$, $\lambda_v = 0.2$, $\lambda_s = 0.5$, low SNR (corresponding to $d_L = 700$ Mpc), randomly chosen sky location and polarization angle, and other parameters given in Table 3.1 was injected in five detectors. The orange lines depict the true parameter values while the blue outlines depict the 68% and 90% credible areas. The priors used to compute the likelihood (Eq. 2.14) are Bilby’s default prior distributions for the sky location (α , δ) and uniform priors for d_L . The priors for the $\vec{\lambda}$ parameters span the entire parameter space allowed after imposing a constraint prior corresponding to Eq. 2.9. Prior distributions that are delta functions at the true value are used for the mass, spin, orientation angle (θ_{jn}), time and phase at coalescence (t_c , ϕ_c) priors. The prior ψ distribution is uniform and periodic $\in [0, \pi]$ for the Bayesian parameter estimation.

We leave for future work more accurate variations of the prior distributions for mass, spin, orientation angle (θ_{jn}), time and phase at coalescence (t_c, ϕ_c).

Note that for most of the analysis, the ψ prior distribution used in Bayesian parameter estimation is a delta function at its true value unless specified otherwise.

In the following sections of this Chapter 3, we focus on presenting our results graphically. For analysis, inference and conclusion of our results refer to Chapter 4.

3.1 Single Event Analysis

In this section, we present the posterior probability distributions of the inferred $\vec{\lambda}$ versus the injected $\vec{\lambda}$ values (colloquially referred to as “violin” plots) for the sets of 528 jobs outlined in Table 2.5. Each violin in this section is created through Single Event Analysis. That is, λ_t , λ_v and λ_s probability distributions are extracted from each individual event through a separate evaluation of the posterior.

The analysis, inference and conclusion for our results is presented in Chapter 4.

Tensor-Vector-Scalar (tvs) polarized GWs

3.1.1. λ_v posterior for tvs polarized GWs; fixed ψ prior

In Figures 3.2, 3.3, and 3.4 we present violin plots of the inferred λ_v posteriors versus the λ_v true values for tvs polarized GWs in all possible three, four, and five detector combinations respectively. Each plot highlights posterior probability distribution violins for 33 different tvs polarized GWs (11 increasing values of λ_v with low, medium and high SNRs).

The one-dimensional λ posterior probability distributions are also plotted as histograms in the Appendix (Figure A.1). The median and errors corresponding to the 90% credible interval for the posterior probability distributions are given in Table A.1 and A.3 in the Appendix. Moreover, the 90% upper and lower limits for the λ_v posterior probability distributions (corresponding to the true values $\lambda_v = 0.0$ and $\lambda_v = 0.5$ respectively) are given in Table A.2.

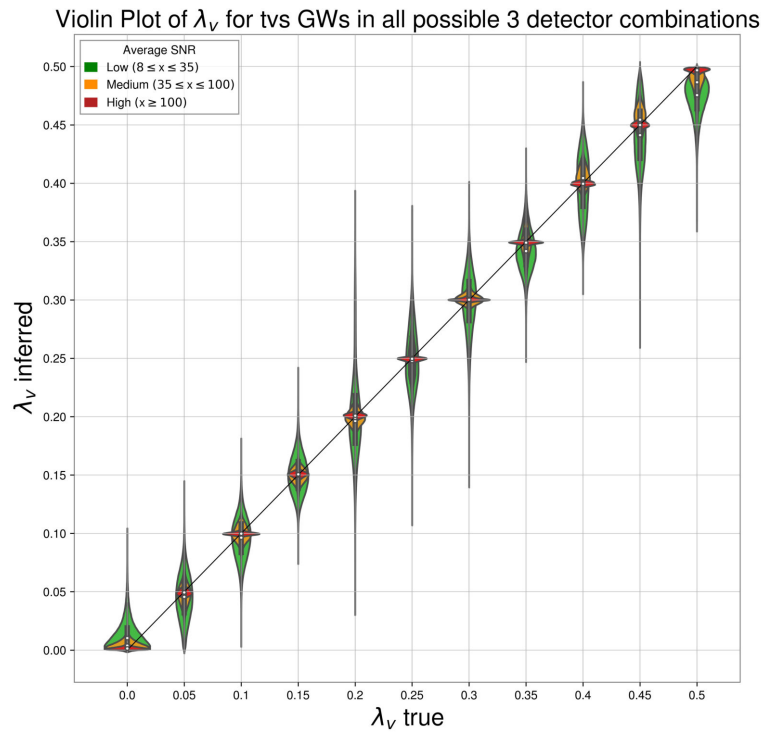
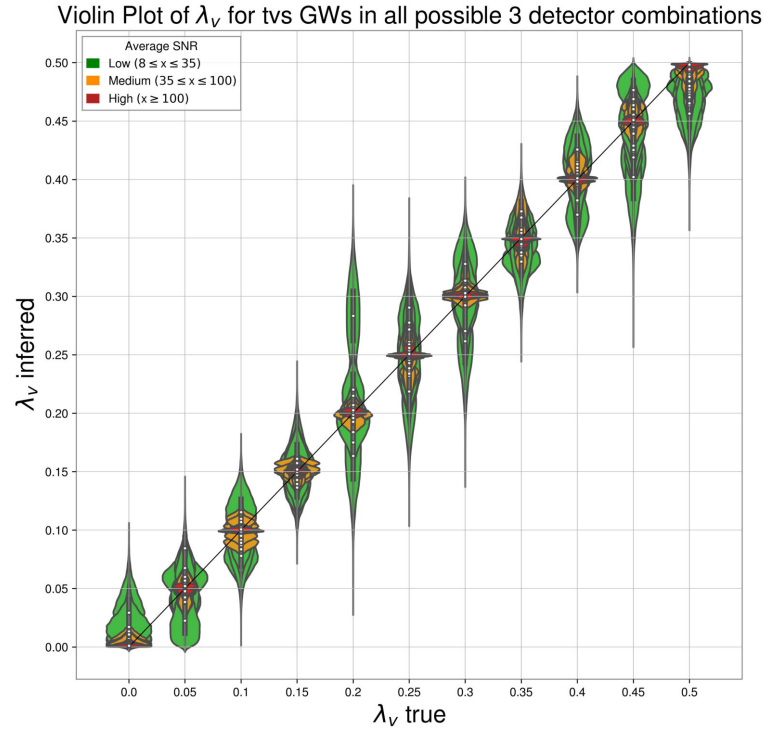


Figure 3.2: Violin plot of λ_V for tvs polarized GW in all possible three-detector combinations for low, medium and high SNRs. For a specific value of λ_V and SNR, the violin plot depicts 10 different violins corresponding to 10 possible three-detector combinations (top) and combines them into a single violin (bottom). Each violin represents an injection with a randomly chosen sky location, polarization angle (ψ) and random distribution of the remaining polarization content between tensor (λ_t value) and scalar (λ_s value) components.

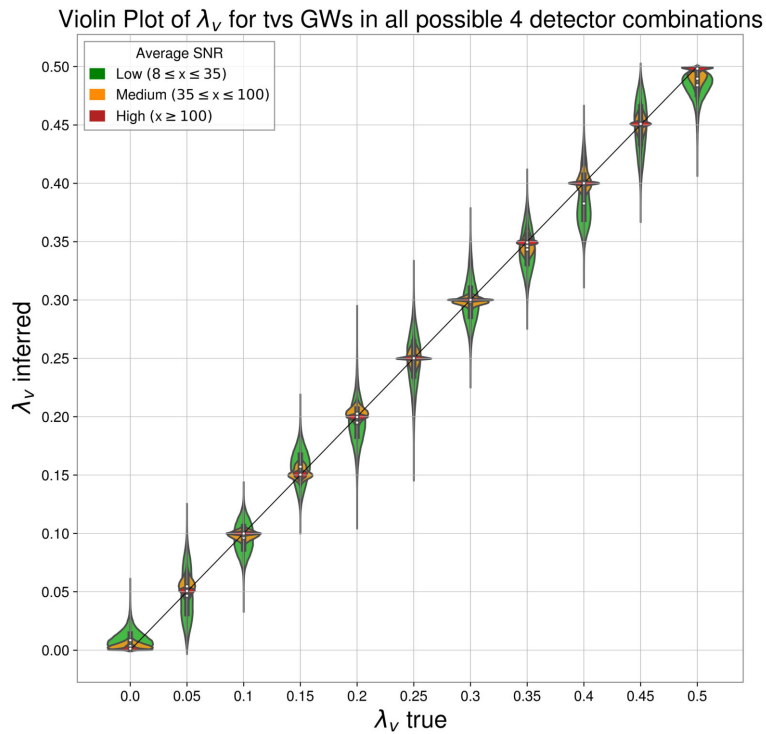
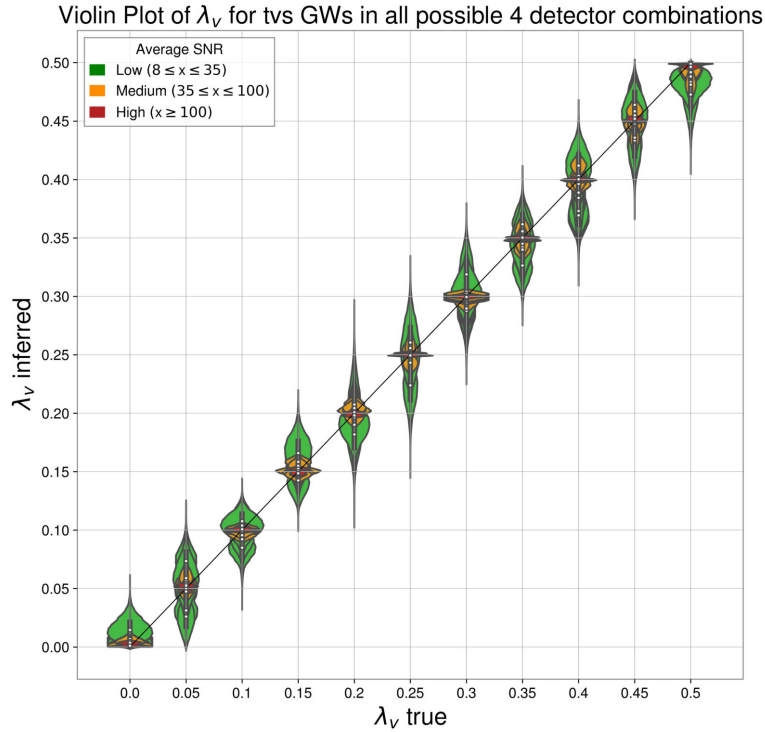


Figure 3.3: Violin plot of λ_v for tvs polarized GW in all possible four-detector combinations for low, medium and high SNRs. For a specific value of λ_v and SNR, the violin plot depicts 5 different violins corresponding to 5 possible four-detector combinations (top) and combines them into a single violin (bottom). Each violin represents an injection with a randomly chosen sky location, polarization angle (ψ) and random distribution of the remaining polarization content between tensor (λ_t value) and scalar (λ_s value) components.

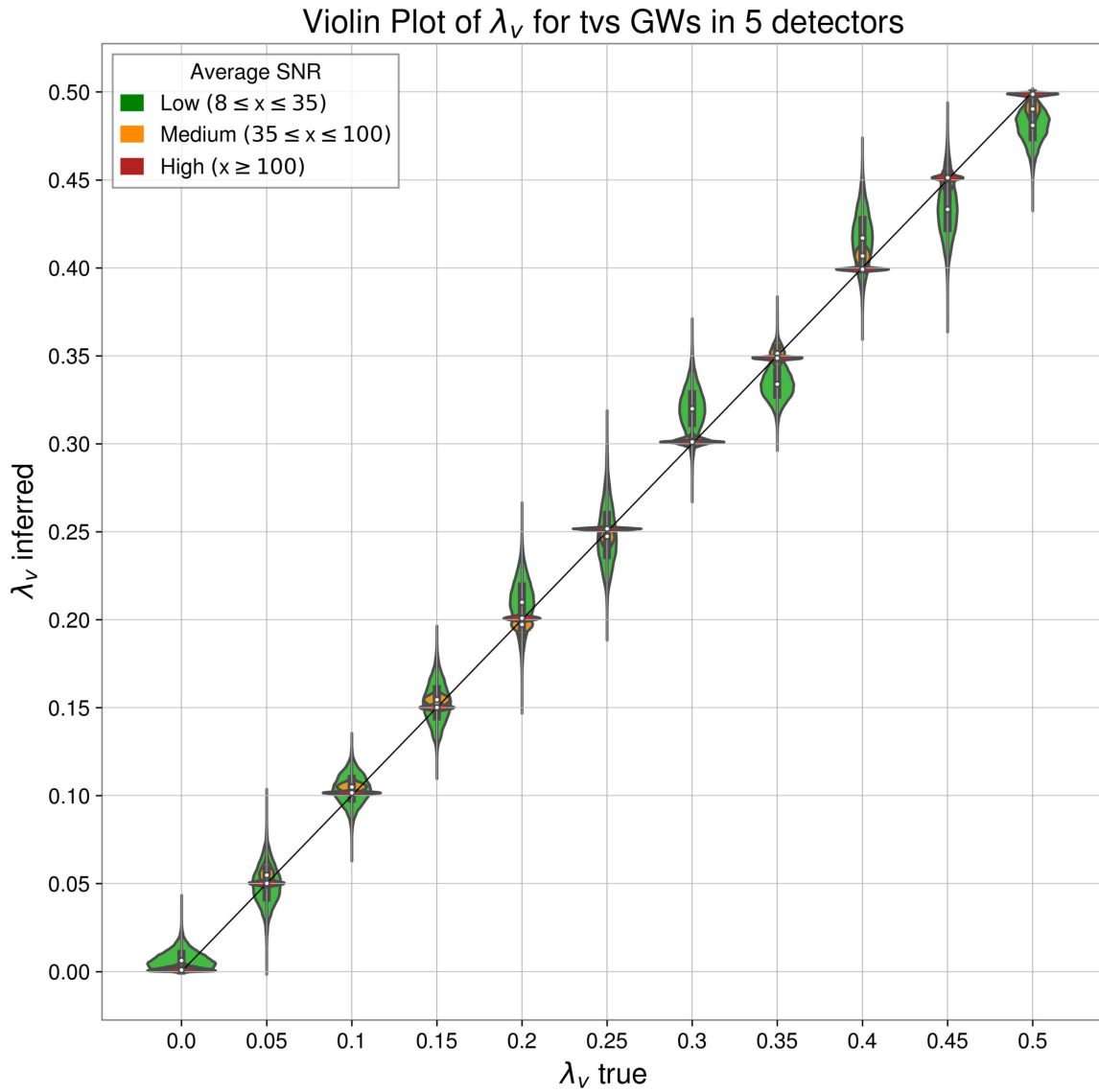


Figure 3.4: Violin plot of λ_v for tvs polarized GW in five detectors for low, medium and high SNRs. Each violin represents an injection with a randomly chosen sky location, polarization angle (ψ) and random distribution of the remaining polarization content between tensor (λ_t value) and scalar (λ_s value) components.

3.1.2. λ_s posterior for tvs polarized GWs; fixed ψ prior

In Figures 3.5, 3.6, and 3.7 we present violin plots of the inferred λ_s posteriors versus the λ_s true values for tvs polarized GWs in all possible three, four, and five detector combinations respectively.

Each plot highlights posterior probability distribution violins for 33 different tvs polarized GWs (11 increasing values of λ_s with low, medium and high SNRs).

The one-dimensional λ posterior probability distributions are also plotted as histograms in the Appendix (Figure A.2). The median and errors corresponding to the 90% credible interval for the posterior probability distributions are given in Table A.4 and A.6 in the Appendix. Moreover, the 90% upper and lower limits for the λ_s posterior probability distributions (corresponding to the true values $\lambda_s = 0.0$ and $\lambda_s = 1.0$ respectively) are given in Table A.5.

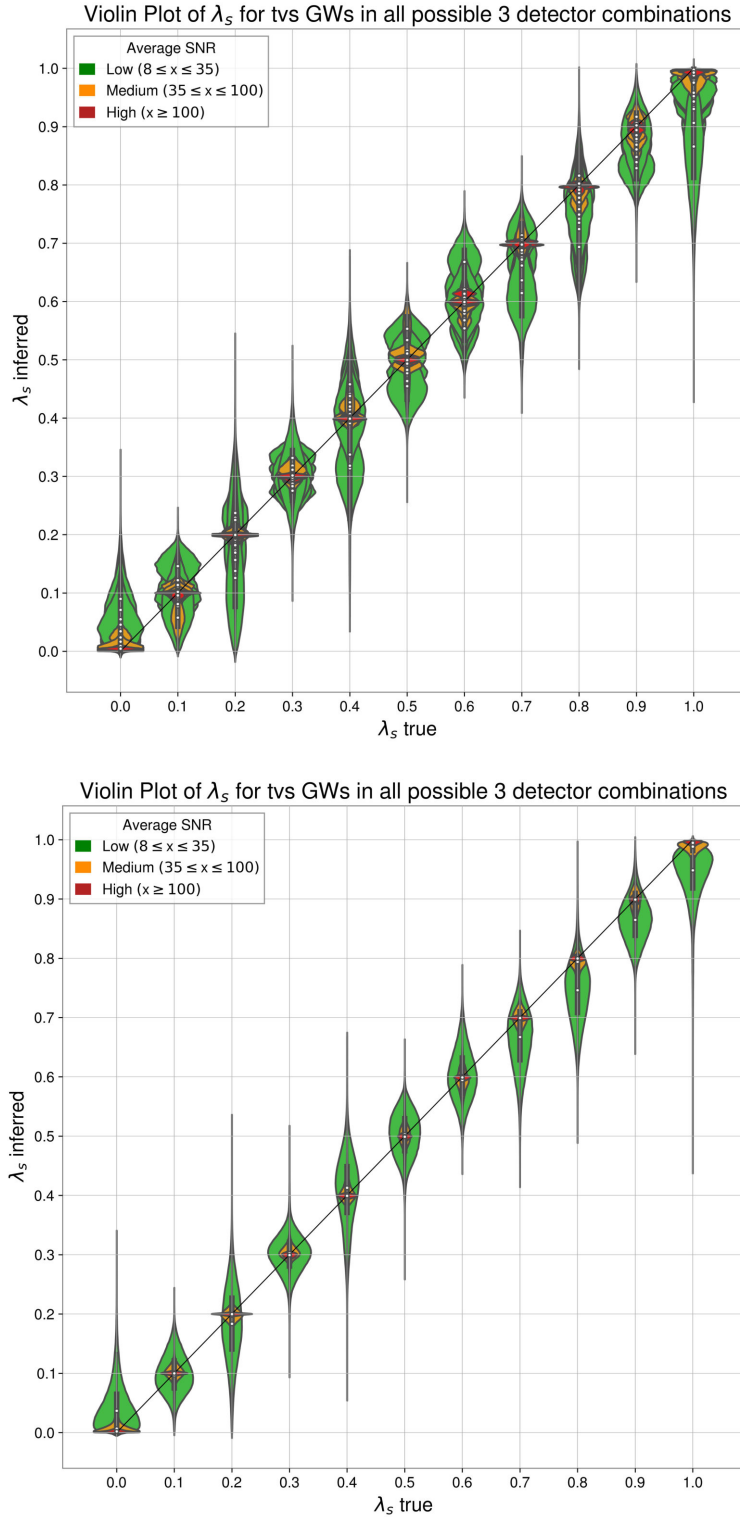


Figure 3.5: Violin plot of λ_s for tvs polarized GW in all possible three-detector combinations for low, medium and high SNRs. For a specific value of λ_s and SNR, the violin plot depicts 10 different violins corresponding to 10 possible three-detector combinations (top) and combines them into a single violin (bottom). Each violin represents an injection with a randomly chosen sky location, polarization angle (ψ) and random distribution of the remaining polarization content between tensor (λ_t value) and vector (λ_v value) components.

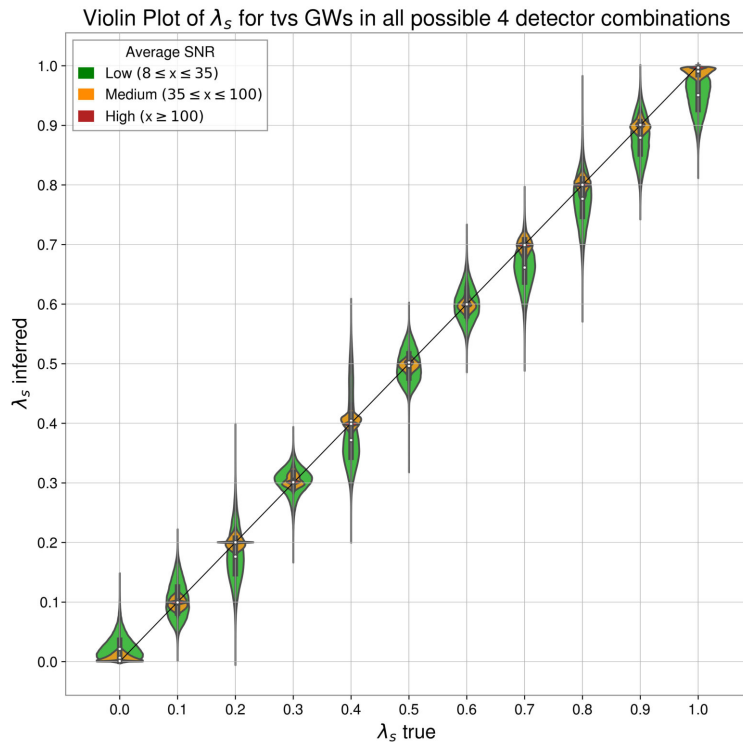
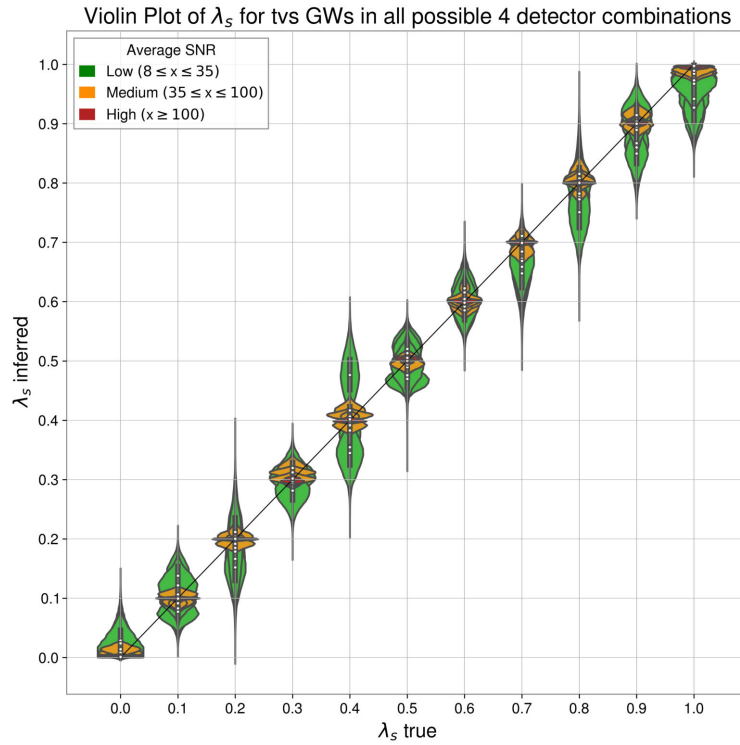


Figure 3.6: Violin plot of λ_s for tvs polarized GW in all possible four-detector combinations for low, medium and high SNRs. For a specific value of λ_s and SNR, the violin plot depicts 5 different violins corresponding to 5 possible four-detector combinations (top) and combines them into a single violin (bottom). Each violin represents an injection with a randomly chosen sky location, polarization angle (ψ) and random distribution of the remaining polarization content between tensor (λ_t value) and vector (λ_v value) components.

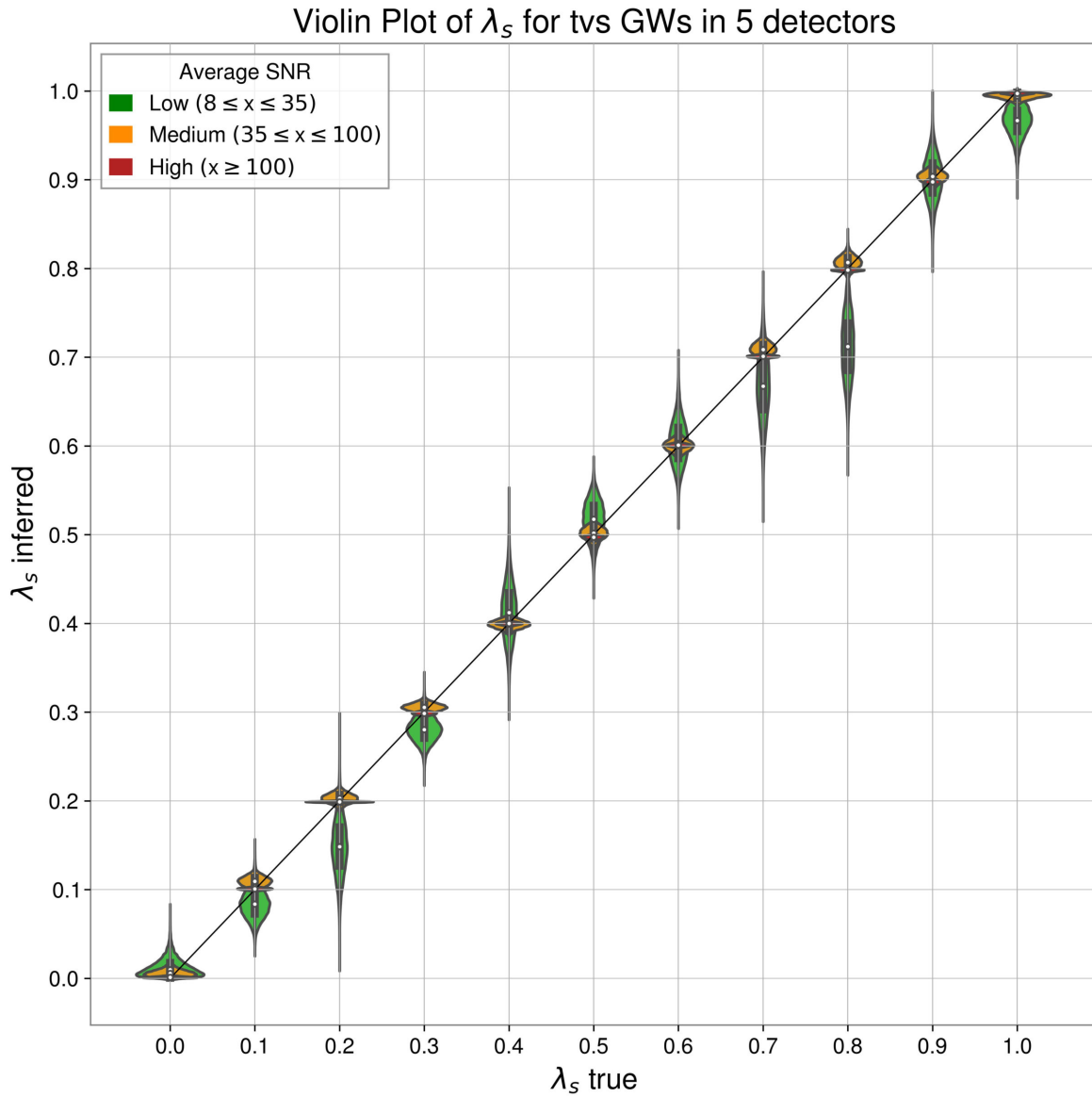


Figure 3.7: Violin plot of λ_s for tvs polarized GW in five detectors for low, medium and high SNRs. Each violin represents an injection with a randomly chosen sky location, polarization angle (ψ) and random distribution of the remaining polarization content between tensor (λ_t value) and vector (λ_v value) components.

Tensor-Vector (tv) polarized GWs

3.1.3. λ_v posterior for tv polarized GWs; fixed ψ prior

In Figures 3.8, 3.9, and 3.10 we present violin plots of the inferred λ_v posteriors versus the λ_v true values for tv polarized GWs in all possible three, four, and five detector combinations respectively.

Each plot highlights posterior probability distribution violins for 33 different tv polarized GWs (11 increasing values of λ_v with low, medium and high SNRs).

The one-dimensional λ posterior probability distributions are also plotted as histograms in the Appendix (Figure A.3). The median and errors corresponding to the 90% credible interval for the posterior probability distributions are given in Table A.7 and A.9 in the Appendix. Moreover, the 90% upper and lower limits for the λ_v posterior probability distributions (corresponding to the true values $\lambda_v = 0.0$ and $\lambda_v = 0.5$ respectively) are given in Table A.8

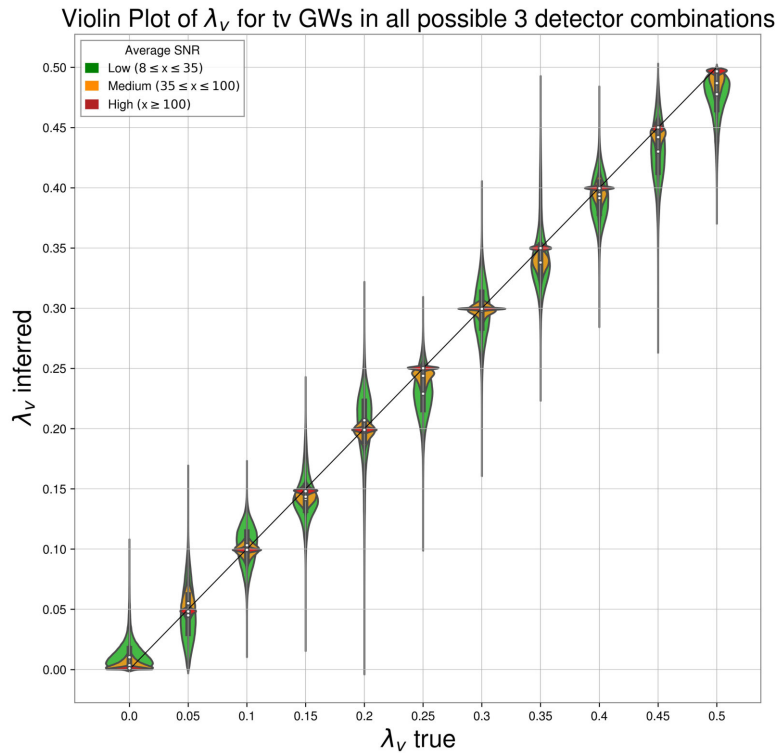
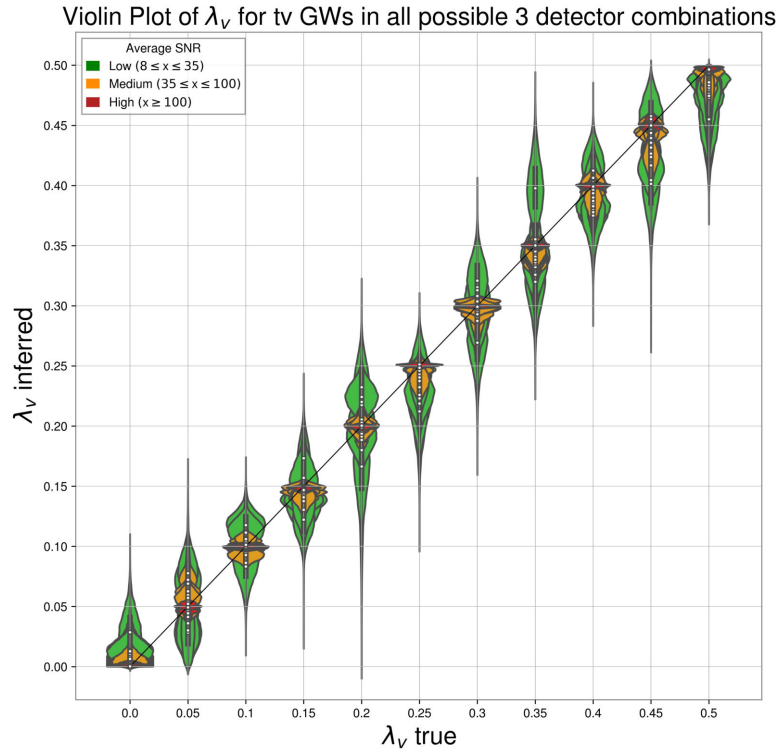


Figure 3.8: Violin plot of λ_v for tv polarized GW in all possible three-detector combinations for low, medium and high SNRs. For a specific value of λ_v and SNR, the violin plot depicts 10 different violins corresponding to 10 possible three-detector combinations (top) and combines them into a single violin (bottom). Each violin represents an injection with a randomly chosen sky location, polarization angle (ψ) where all remaining polarization content is tensorial (i.e., $\lambda_s = 0$).

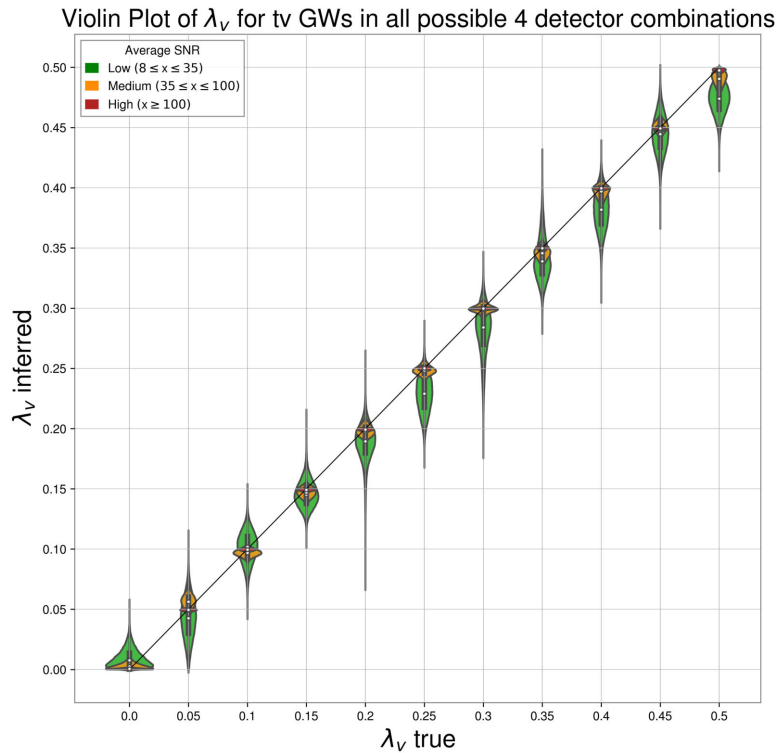
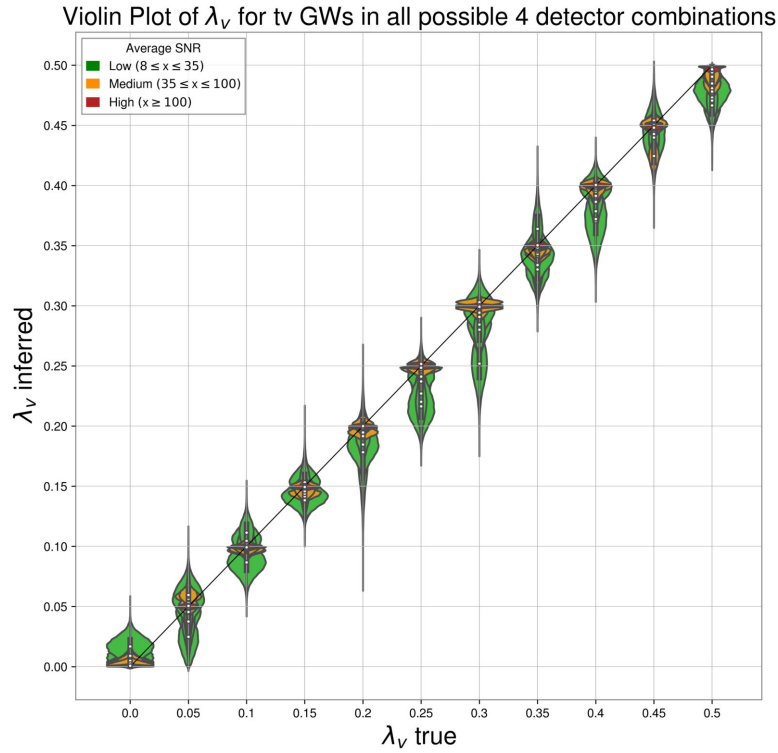


Figure 3.9: Violin plot of λ_ν for tv polarized GW in all possible four-detector combinations for low, medium and high SNRs. For a specific value of λ_ν and SNR, the violin plot depicts 5 different violins corresponding to 5 possible four-detector combinations (top) and combines them into a single violin (bottom). Each violin represents an injection with a randomly chosen sky location, polarization angle (ψ) where all remaining polarization content is tensorial (i.e., $\lambda_S = 0$).

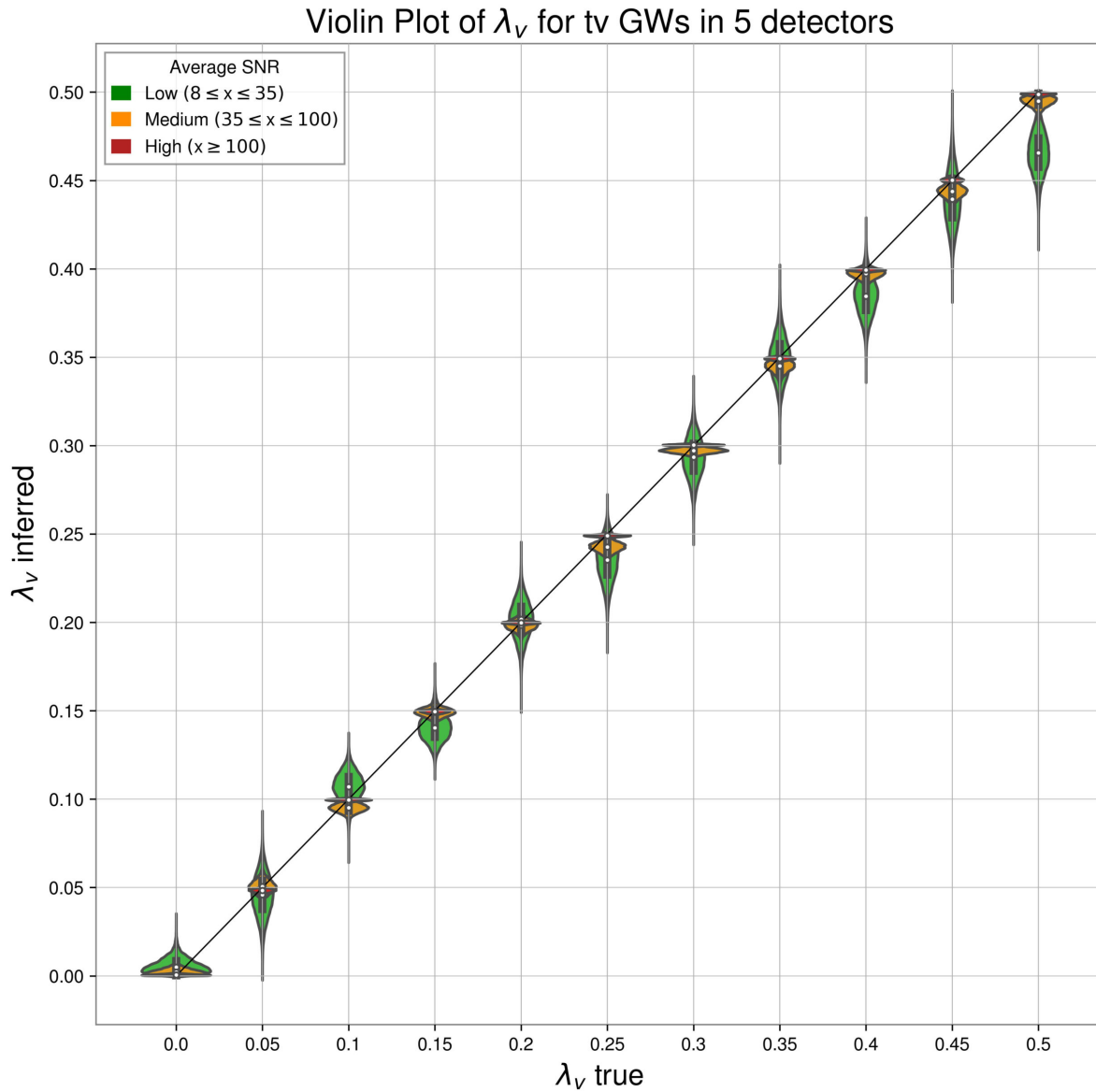


Figure 3.10: Violin plot of λ_v for tv polarized GW in five detectors for low, medium and high SNRs. Each violin represents an injection with a randomly chosen sky location, polarization angle (ψ) where all remaining polarization content is tensorial (i.e., $\lambda_s = 0$).

Tensor-Scalar (ts) polarized GWs

3.1.4. λ_s posterior for ts polarized GWs; fixed ψ prior

In Figures 3.11, 3.12, and 3.13 we present violin plots of the inferred λ_s posteriors versus the λ_s true values for ts polarized GWs in all possible three, four, and five detector combinations respectively.

Each plot highlights posterior probability distribution violins for 33 different ts polarized GWs (11 increasing values of λ_s with low, medium and high SNRs).

The one-dimensional λ posterior probability distributions are also plotted as histograms in the Appendix (Figure A.4). The median and errors corresponding to the 90% credible interval for the posterior probability distributions are given in Table A.10 and A.12 in the Appendix. Moreover, the 90% upper and lower limits for the λ_s posterior probability distributions (corresponding to the true values $\lambda_s = 0.0$ and $\lambda_s = 1.0$ respectively) are given in Table A.11.

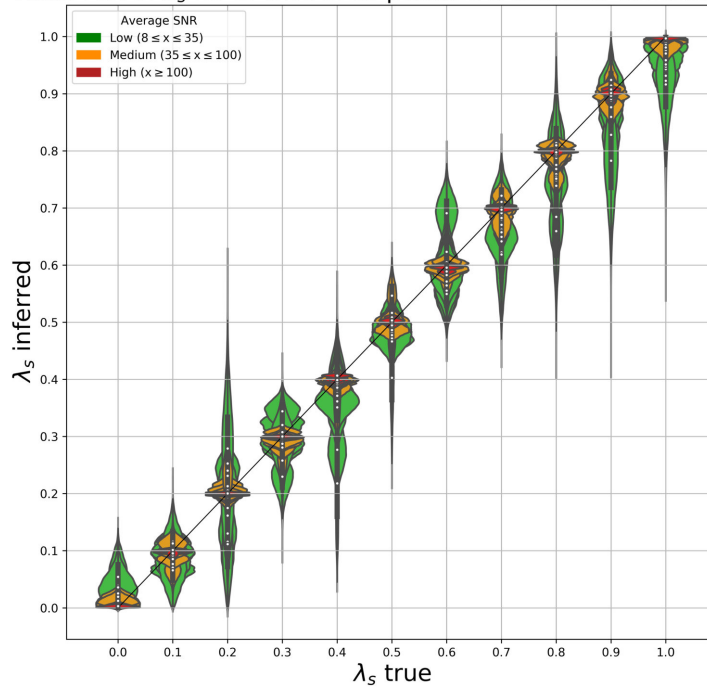
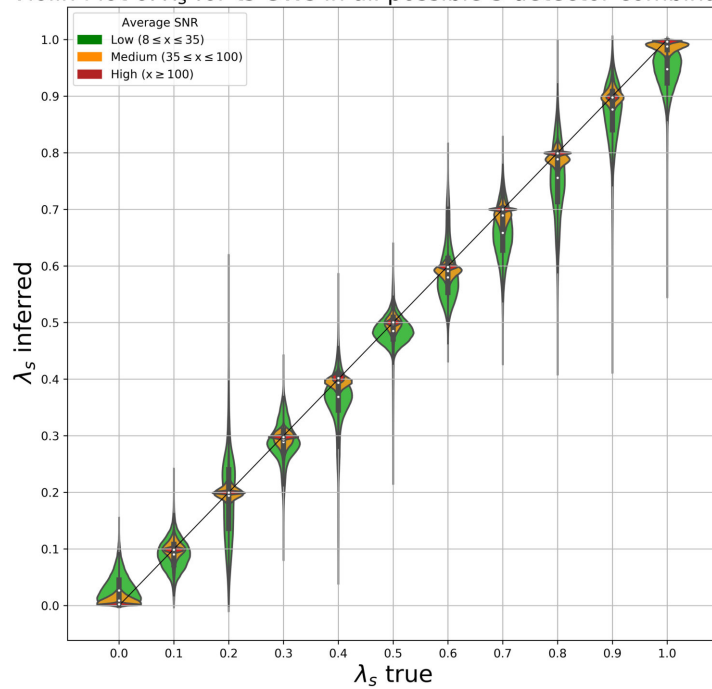
Violin Plot of λ_s for ts GWs in all possible 3 detector combinationsViolin Plot of λ_s for ts GWs in all possible 3 detector combinations

Figure 3.11: Violin plot of λ_s for ts polarized GW in all possible three-detector combinations for low, medium and high SNRs. For a specific value of λ_s and SNR, the violin plot depicts 10 different violins corresponding to 10 possible three-detector combinations (top) and combines them into a single violin (bottom). Each violin represents an injection with a randomly chosen sky location, polarization angle (ψ) where all remaining polarization content is tensorial (i.e., $\lambda_v = 0$).

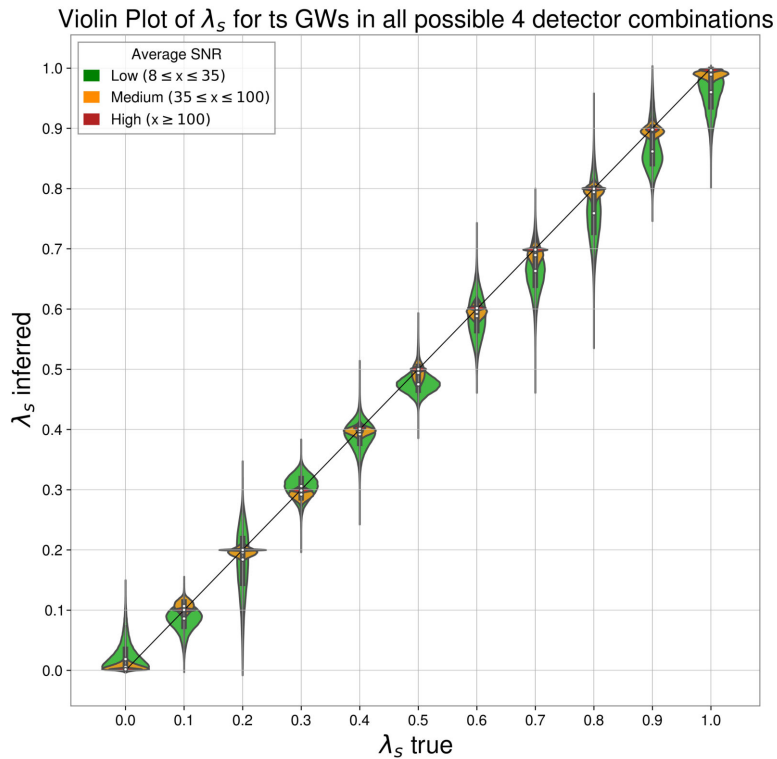
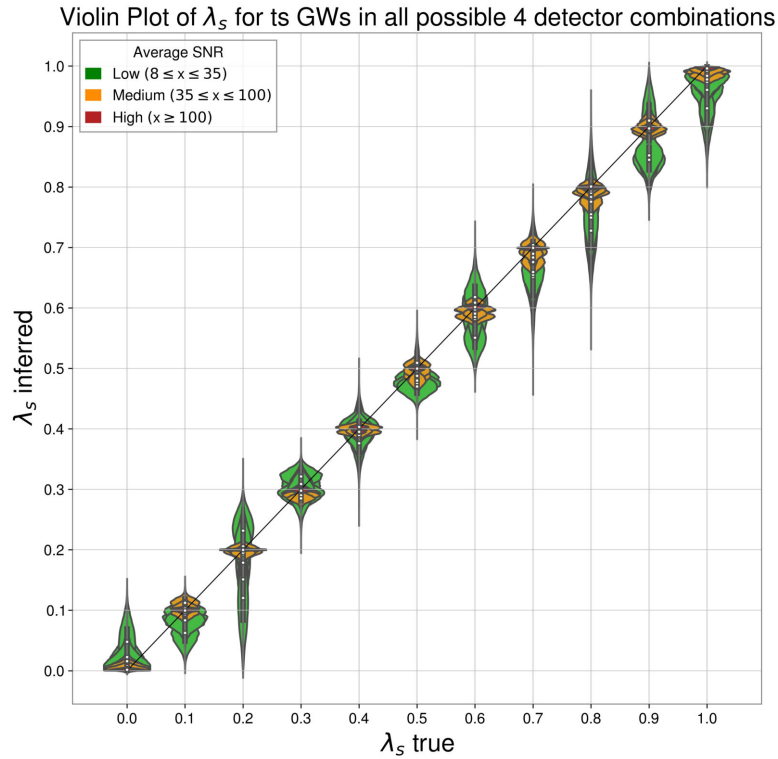


Figure 3.12: Violin plot of λ_s for ts polarized GW in all possible four-detector combinations for low, medium and high SNRs. For a specific value of λ_s and SNR, the violin plot depicts 5 different violins corresponding to 5 possible four-detector combinations (top) and combines them into a single violin (bottom). Each violin represents an injection with a randomly chosen sky location, polarization angle (ψ) where all remaining polarization content is tensorial (i.e., $\lambda_v = 0$).

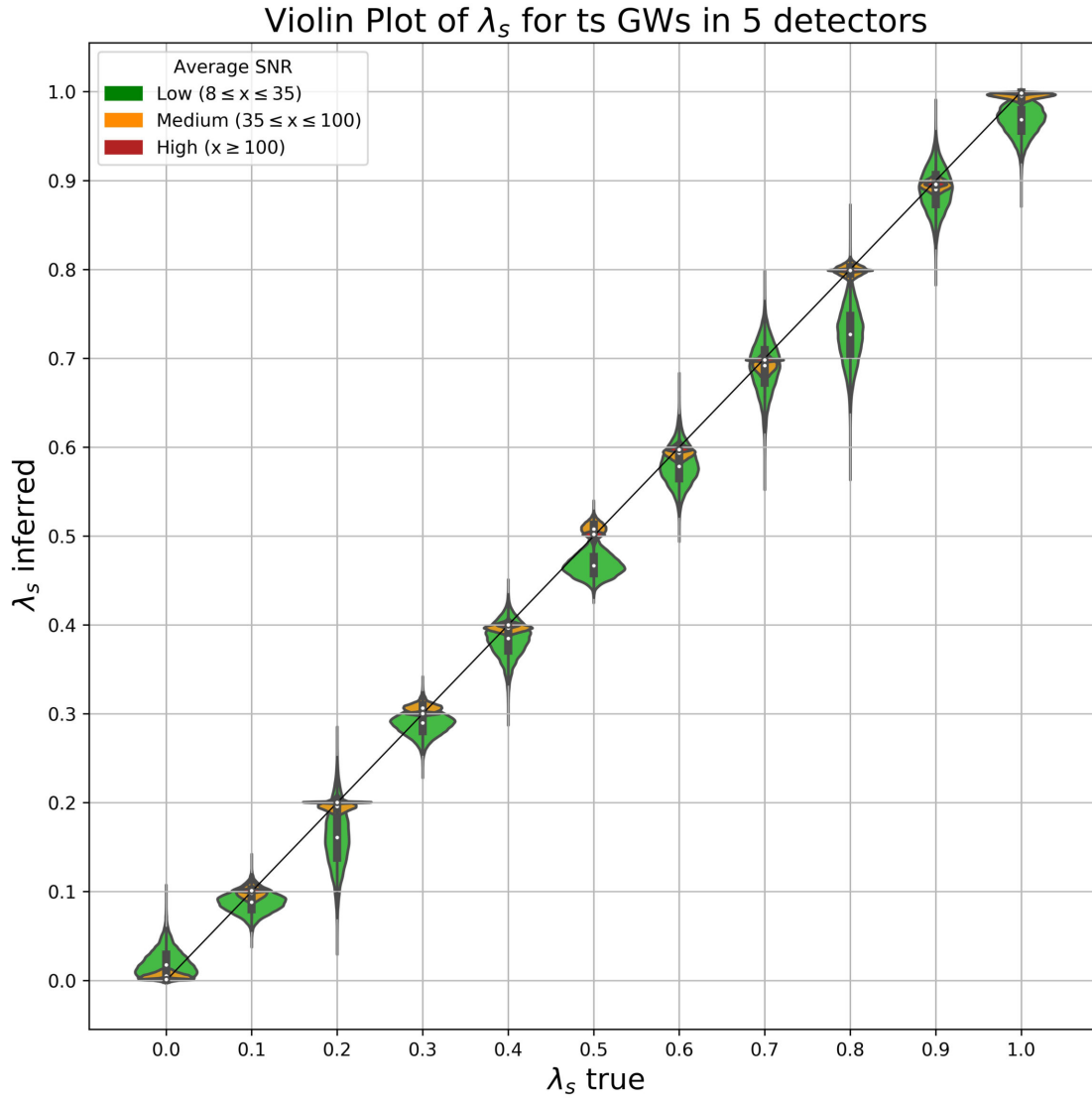


Figure 3.13: Violin plot of λ_s for ts polarized GW in five detectors for low, medium and high SNRs. Each violin represents an injection with a randomly chosen sky location, polarization angle (ψ) where all remaining polarization content is tensorial (i.e., $\lambda_v = 0$).

Tensor-Vector-Scalar (tvs) polarized GW

3.1.5. λ_v posterior for tvs polarized GWs; uniform ψ prior

In Figures 3.14, 3.15, and 3.16 we present violin plots of the inferred λ_v posteriors versus the λ_v true values for tvs polarized GWs in all possible three, four, and five detector combinations respectively.

Each plot highlights posterior probability distribution violins for 33 different tvs polarized GWs (11 increasing values of λ_v with low, medium and high SNRs). The ψ prior distribution is uniform and periodic $\in [0, \pi]$ for the Bayesian parameter estimation.

The one-dimensional λ posterior probability distributions are also plotted as histograms in the Appendix (Figure A.5). The median and errors corresponding to the 90% credible interval for the posterior probability distributions are given in Table A.13 and A.15 in the Appendix. Moreover, the 90% upper and lower limits for the λ_v posterior probability distributions (corresponding to the true values $\lambda_v = 0.0$ and $\lambda_v = 0.5$ respectively) are given in Table A.14.

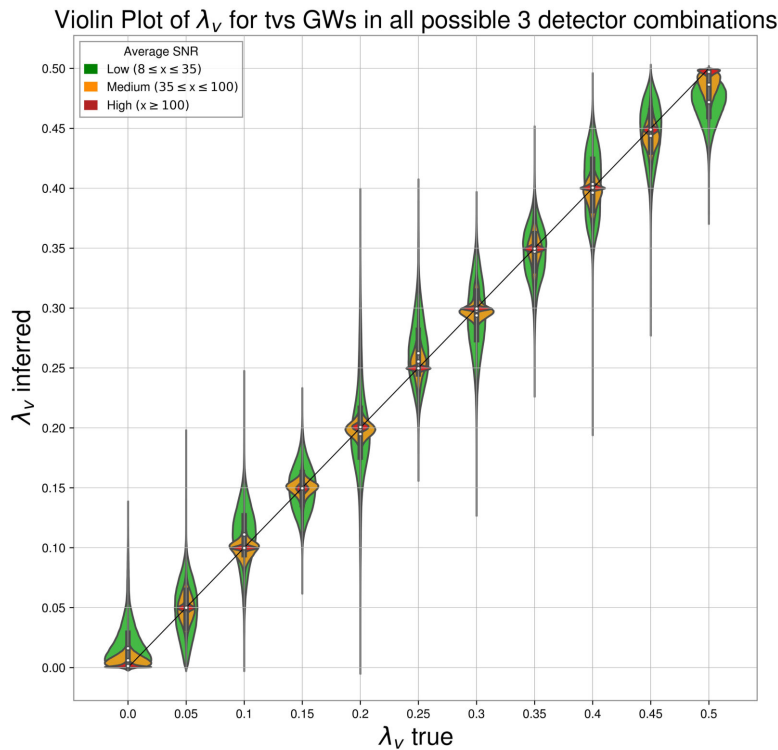
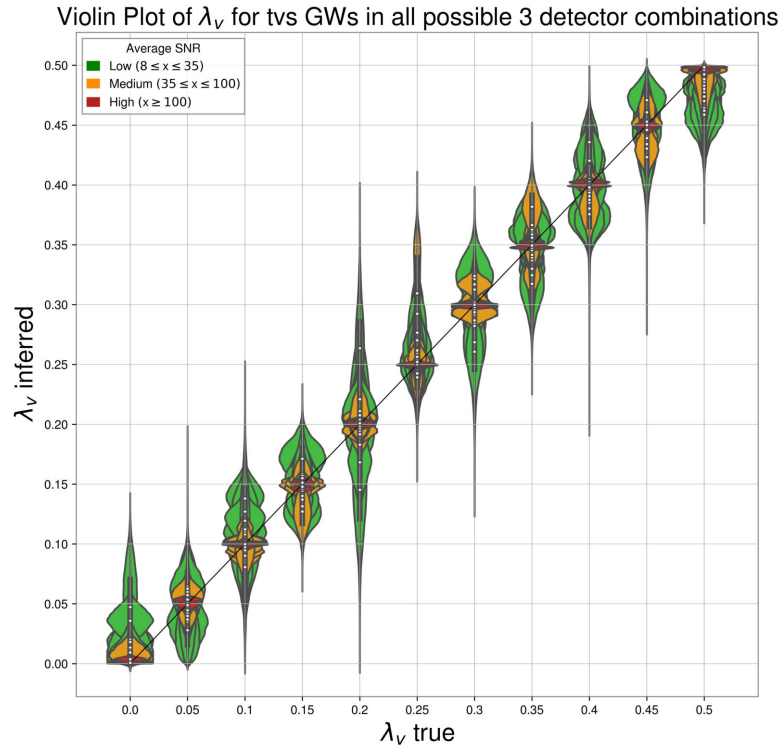


Figure 3.14: Violin plot of λ_V for tvs polarized GW in all possible three-detector combinations for low, medium and high SNRs. For a specific value of λ_V and SNR, the violin plot depicts 10 different violins corresponding to 10 possible three-detector combinations (top) and combines them into a single violin (bottom). Each violin represents an injection with a randomly chosen sky location, polarization angle (ψ) and random distribution of the remaining polarization content between tensor (λ_t value) and scalar (λ_s value) components. The ψ prior distribution is uniform and periodic $\in [0, \pi]$ for the Bayesian parameter estimation.

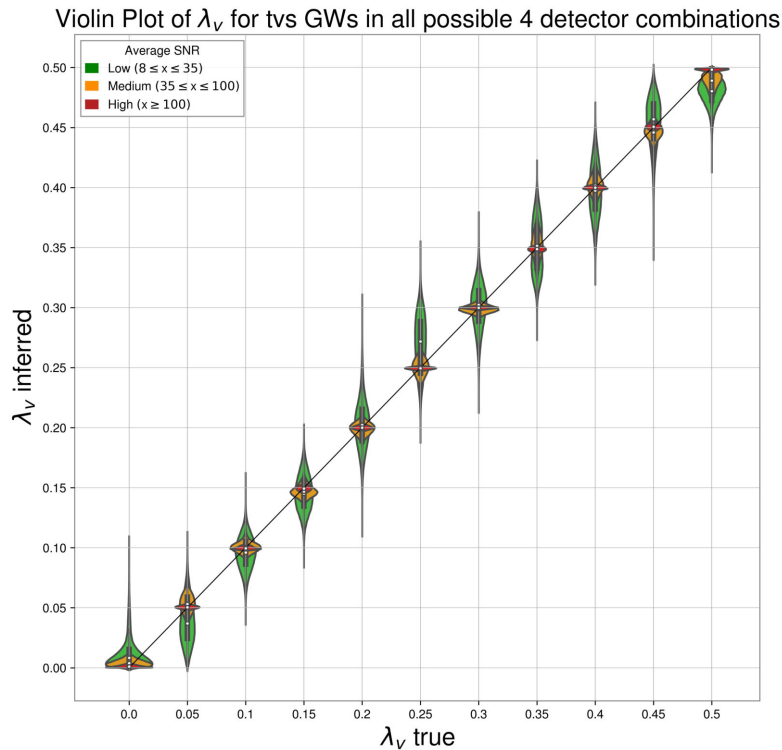
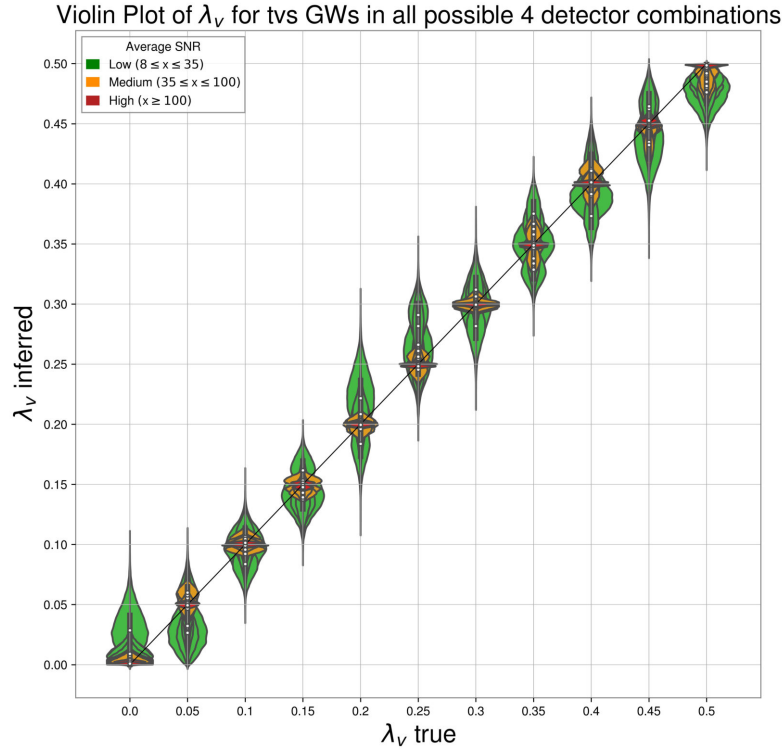


Figure 3.15: Violin plot of λ_v for tvs polarized GW in all possible four-detector combinations for low, medium and high SNRs. For a specific value of λ_v and SNR, the violin plot depicts 5 different violins corresponding to 5 possible four-detector combinations (top) and combines them into a single violin (bottom). Each violin represents an injection with a randomly chosen sky location, polarization angle (ψ) and random distribution of the remaining polarization content between tensor (λ_t value) and scalar (λ_s value) components. The ψ prior distribution is uniform and periodic $\in [0, \pi]$ for the Bayesian parameter estimation.

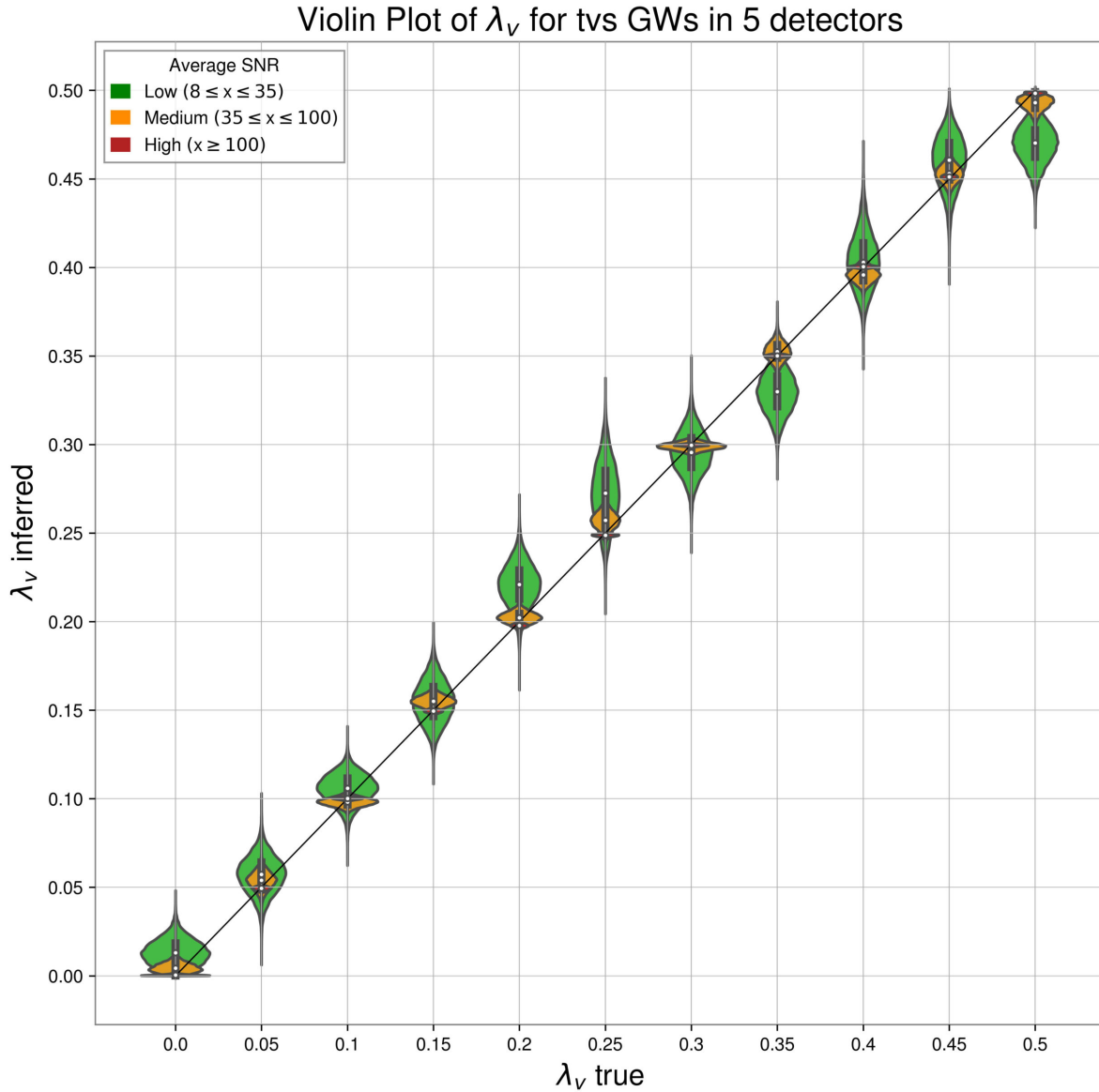


Figure 3.16: Violin plot of λ_v for tvs polarized GW in five detectors for low, medium and high SNRs. Each violin represents an injection with a randomly chosen sky location, polarization angle (ψ) and random distribution of the remaining polarization content between tensor (λ_t value) and scalar (λ_s value) components. The ψ prior distribution is uniform and periodic $\in [0, \pi]$ for the Bayesian parameter estimation.

3.1.6. λ_s posterior for tvs polarized GWs; uniform ψ prior

In Figures 3.17, 3.18, and 3.19 we present violin plots of the inferred λ_s posteriors versus the λ_s true values for tvs polarized GWs in three, four, and five detector combinations respectively.

Each plot highlights posterior probability distribution violins for 33 different tvs polarized GWs (11 increasing values of λ_s with low, medium and high SNRs). The ψ prior distribution is uniform and periodic $\in [0, \pi]$ for the Bayesian parameter estimation.

However, the LIGO Caltech computing cluster was overburdened at the time when these jobs were submitted. As a result, 519 of out the 528 specified jobs in Table 2.5 were completed in a reasonable time (16 days). The specifications of the missing job are outlined in the Appendix.

The one-dimensional λ posterior probability distributions are also plotted as histograms in the Appendix (Figure A.6). The median and errors corresponding to the 90% credible interval for the posterior probability distributions are given in Table A.16 and A.18 in the Appendix. Moreover, the 90% upper and lower limits for the λ_s posterior probability distributions (corresponding to the true values $\lambda_s = 0.0$ and $\lambda_s = 1.0$ respectively) are given in Table A.17.

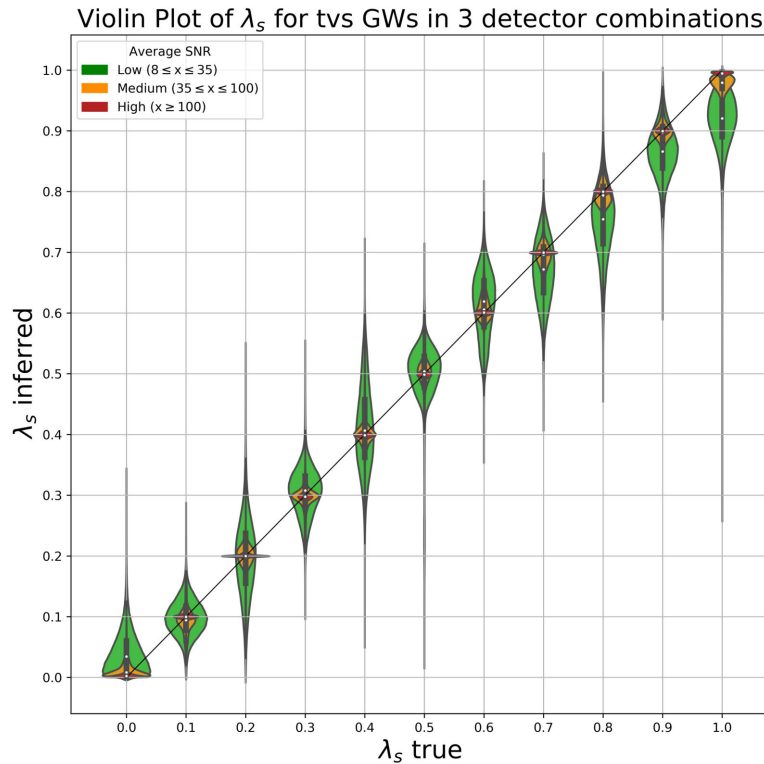
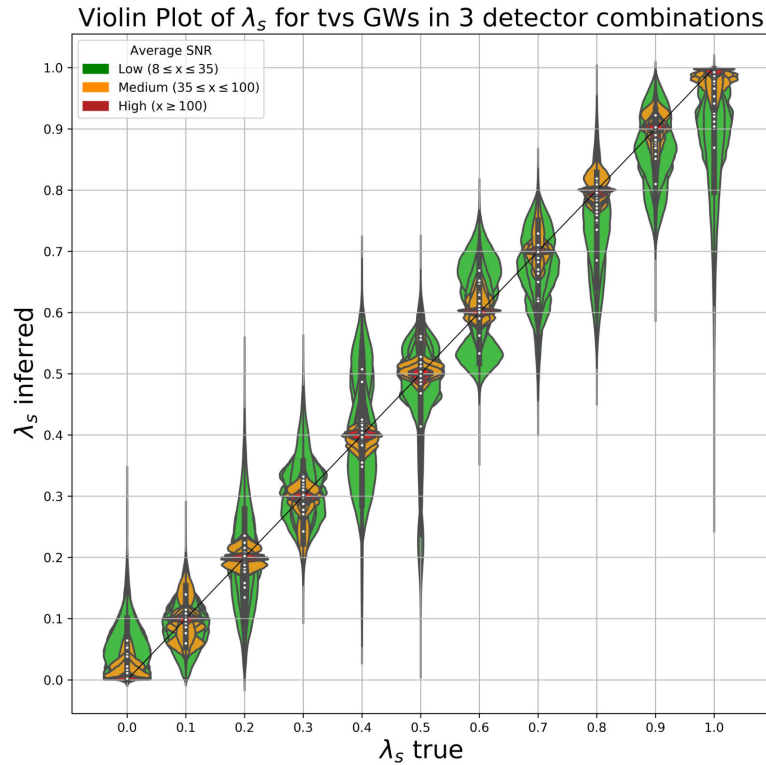


Figure 3.17: Violin plot of λ_s for tvs polarized GW in three-detector combinations for low, medium and high SNRs. For a specific value of λ_s and SNR, the violin plot depicts 10 different violins corresponding to 10 possible three-detector combinations (top) and combines them into a single violin (bottom). Each violin represents an injection with a randomly chosen sky location, polarization angle (ψ) and random distribution of the remaining polarization content between tensor (λ_t value) and vector (λ_v value) components. The ψ prior distribution is uniform and periodic $\in [0, \pi]$ for the Bayesian parameter estimation.

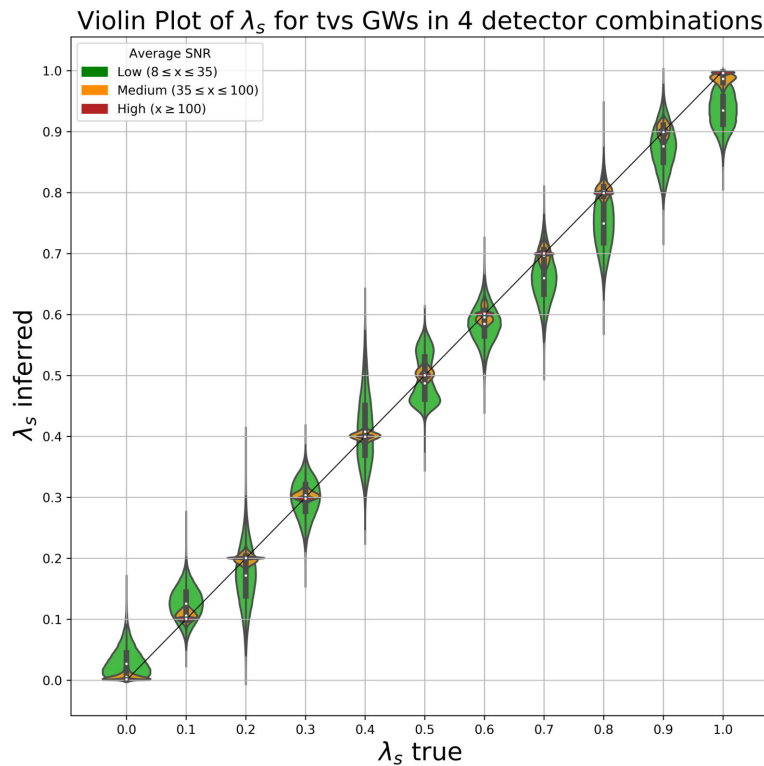
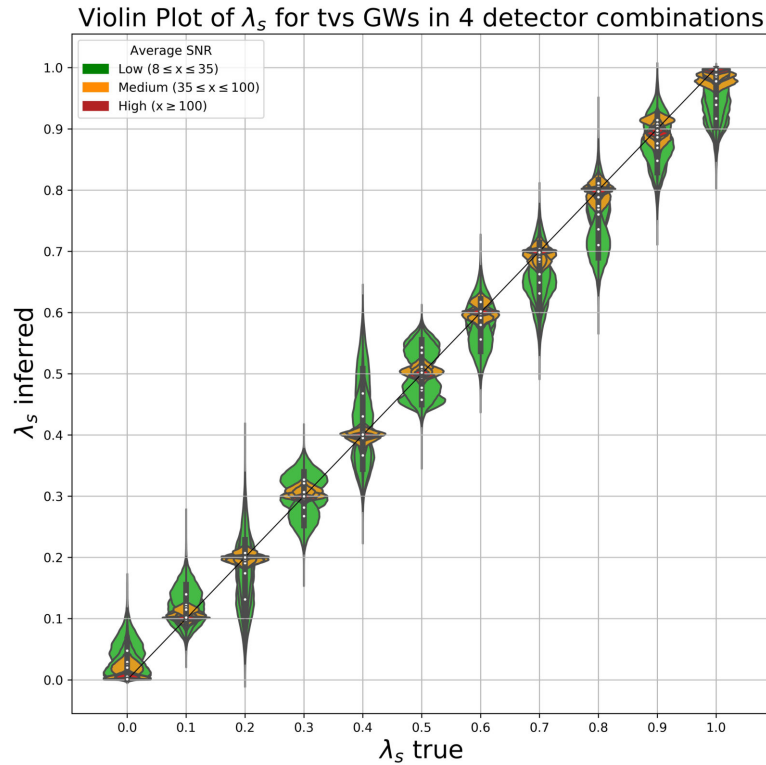


Figure 3.18: Violin plot of λ_s for tvs polarized GW in four-detector combinations for low, medium and high SNRs. For a specific value of λ_s and SNR, the violin plot depicts 5 different violins corresponding to 5 possible four-detector combinations (top) and combines them into a single violin (bottom). Each violin represents an injection with a randomly chosen sky location, polarization angle (ψ) and random distribution of the remaining polarization content between tensor (λ_t value) and vector (λ_v value) components. The ψ prior distribution is uniform and periodic $\in [0, \pi]$ for the Bayesian parameter estimation.

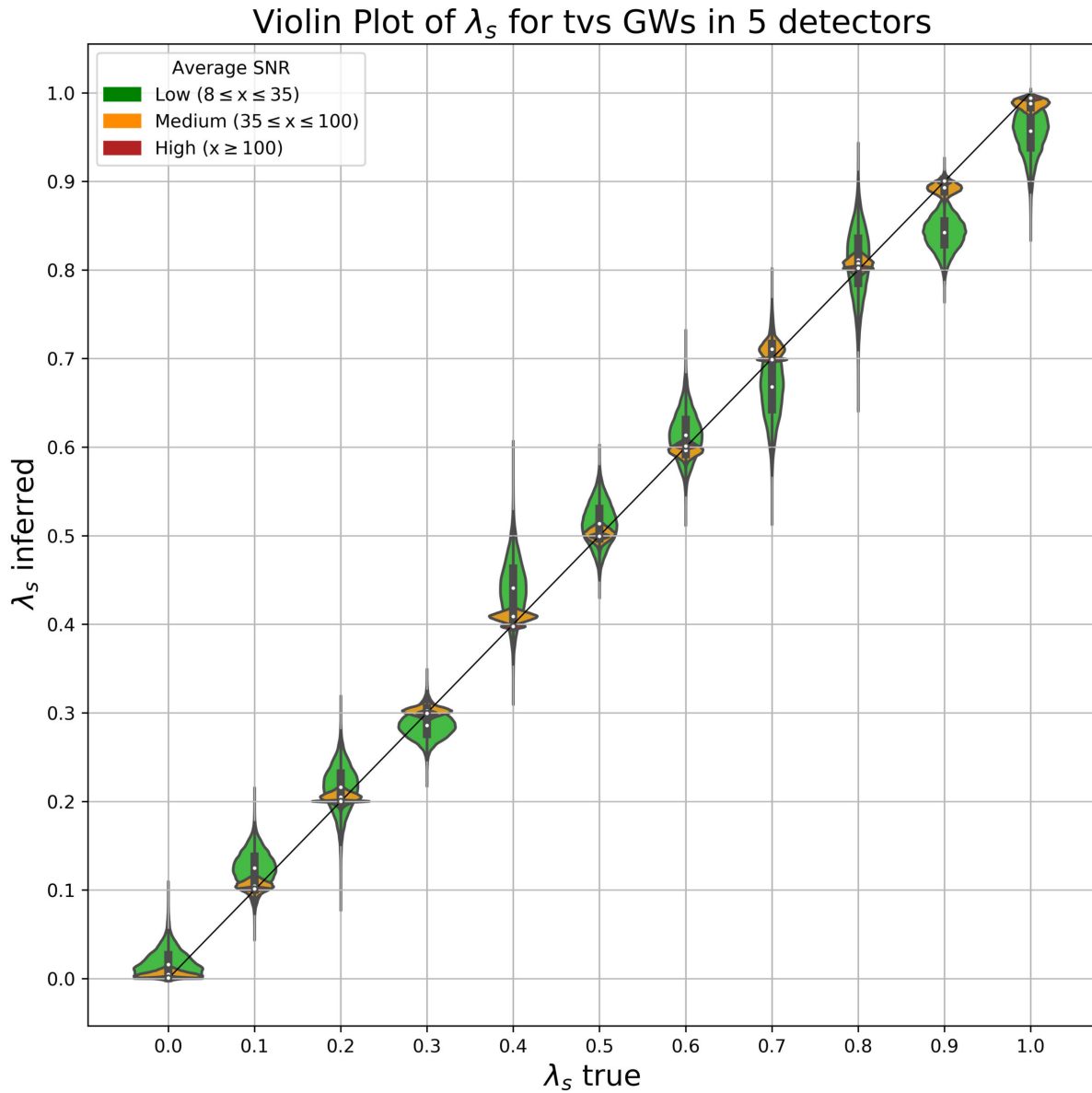


Figure 3.19: Violin plot of λ_s for tvs polarized GW in five detectors for low, medium and high SNRs. Each violin represents an injection with a randomly chosen sky location, polarization angle (ψ) and random distribution of the remaining polarization content between tensor (λ_t value) and vector (λ_v value) components. The ψ prior distribution is uniform and periodic $\in [0, \pi]$ for the Bayesian parameter estimation.

3.1.7. $\vec{\lambda}$ posteriors for tvs polarized GWs with different BBH component masses

Next, we run 9 HTCondor jobs that simulate 9 different tvs polarized GWs in a five-detector network (outlined in the first row of Table 2.6).

These 9 different tvs polarized GWs are further split into 3 simulations of progressively increasing BBH component masses with low ($d_L \in [300, 450, 700]$ Mpc), medium ($d_L \approx 150$ Mpc) and high ($d_L = 70$ Mpc) SNR signals and polarization content corresponding to $\lambda_t = 0.2$, $\lambda_v = 0.15$, $\lambda_s = 0.3$.

Each of the 9 different GWs has a randomly chosen sky location and polarization angle from uniform distributions of $\alpha \in [0, 2\pi]$, $\sin \delta \in [-1, 1]$, and $\psi \in [0, \pi]$. The remaining simulation parameters are common in all 9 injections and are given in Table 3.2. The three progressively increasing BBH component masses have an arbitrarily fixed mass ratio = 0.8 for simplicity.

Thus, 9 jobs = 3 different BBH component masses \times 3 different SNRs.

The purpose of these jobs is to verify that our methods work for different BBH component masses.

Symbol	Parameter	Value
λ_t	Tensor polarization parameter	0.20
λ_v	Vector polarization parameter	0.15
λ_s	Scalar polarization parameter	0.3
\vec{s}_1	Spin vector of primary black hole [M_\odot]	0.
\vec{s}_2	Spin vector of secondary black hole [M_\odot]	0.
θ_{jn}	Inclination angle (with spin orbit precession) [rad]	0.4
ψ	Polarization angle [rad]	random
t_c	Time at coalescence [GPS time in sec]	1451260818 (Jan 1, 2026)
ϕ_c	Phase at coalescence [rad]	1.3

Table 3.2: Table of common parameters in the 9 condor jobs used to verify that our method works for different BBH component masses.

The priors used to compute the likelihood (Eq. 2.14) are Bilby’s default prior distributions for the masses and sky location (α, δ), and uniform priors for d_L . The priors for the $\vec{\lambda}$ parameters span the entire parameter space allowed after imposing a constraint prior corresponding to Eq. 2.9. Prior distributions that are delta functions at the true value are used for the mass, spin, orientation angle and polarization angle (θ_{jn}, ψ) and time and phase at coalescence (t_c, ϕ_c) parameters in Table 3.2.

The one-dimensional λ posterior probability distributions are also plotted as histograms in the Appendix (Figure A.7). The median and errors corresponding to the 90% credible interval for the posterior probability distributions are given in Table A.19 and A.20 in the Appendix.

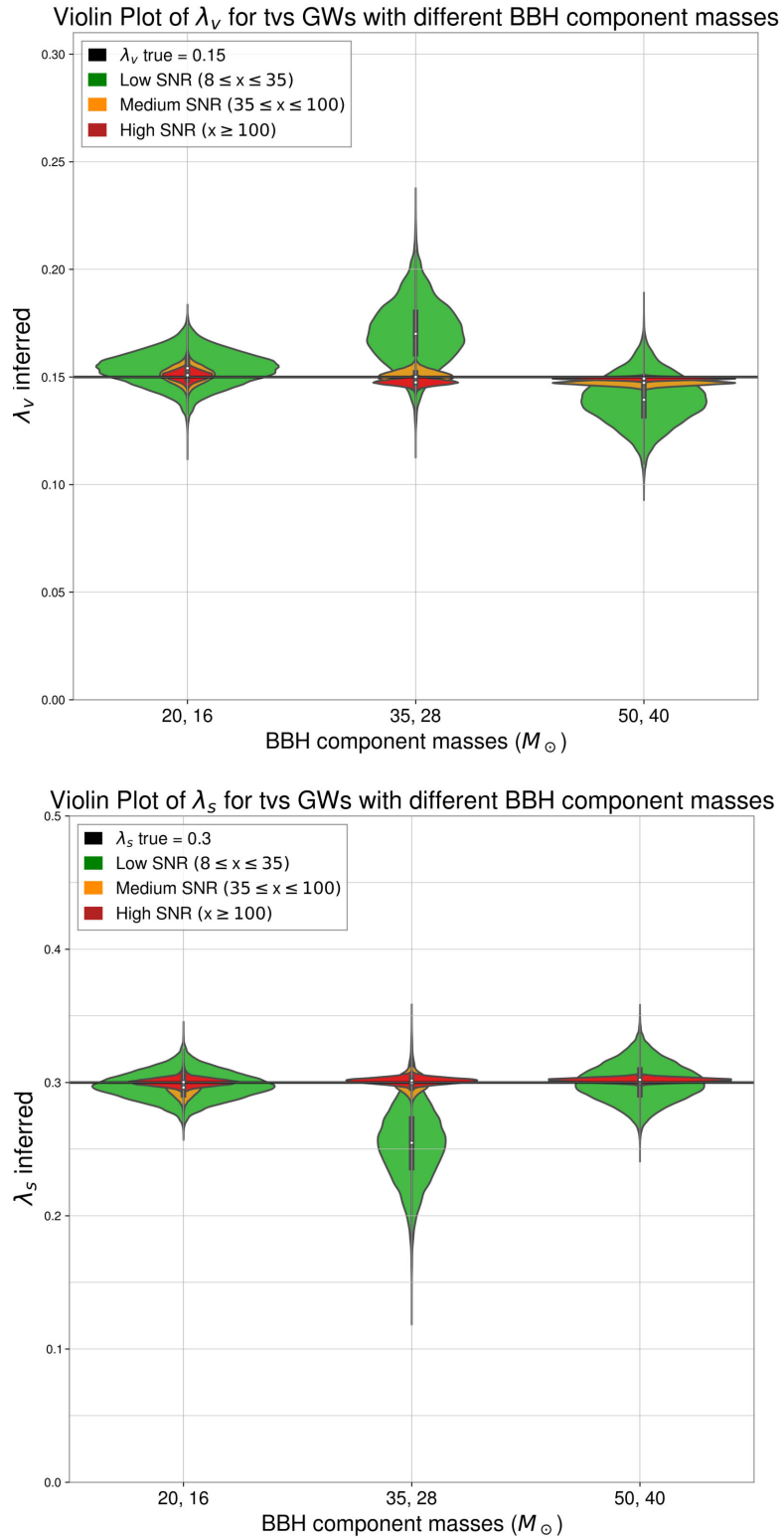


Figure 3.20: Violin plot of λ_v (top) and λ_s (bottom) posteriors for tvs polarized GWs from BBHs with progressively increasing component masses for low, medium and high SNRs in five detectors. The true values of the $\vec{\lambda}$ parameters are $\lambda_v = 0.15$ and $\lambda_s = 0.3$. Each violin represents an injection with a randomly chosen sky location and polarization angle (ψ).

3.2 Multiple Event Analysis

In this section, we explore the possibility that the fraction of vector and/or scalar polarization content is constant for all GW radiation. This involves the hypothesis that the polarization parameters $\vec{\lambda}$ are shared between different GW detections and are independent of all other parameters and properties of the BBH merger.

We generate joint posterior probability distributions for n number of such event by marginalizing over all other parameters. The $\vec{\lambda}$ posterior probability distributions are extracted from each individual event through single event evaluation of the posterior, plotted as one-dimensional histograms and multiplied bin by bin to generate a joint $\vec{\lambda}$ posterior.

We run 149 “embarrassingly parallel” HTCondor jobs simulating 149 different GW injections in a network of five detectors. The polarization content of all 149 GWs corresponds to $\lambda_t = 0.2$, $\lambda_v = 0.15$ and $\lambda_s = 0.3$.

Each GW has a randomly chosen sky location, polarization, luminosity distance and mass of the primary black hole from uniform distributions of $\alpha \in [0, 2\pi]$, $\sin \delta \in [-1, 1]$, $\psi \in [0, \pi]$, $d_L \in [100, 200]$ Mpc, and $m_1 \in [20, 50] M_\odot$ in a network of five detectors.

Masses of the secondary black hole are arbitrarily selected by randomly choosing a mass ratio from the uniform distribution of mass ratio $\in [0.4, 0.8]$ for the 149 injections.

The randomly chosen GPS time corresponds to Jan 1, 2026 when we look forward to observing data from five ground-based GW detectors. Note that the common t_c for all the GW injections is not a problem in our simulated study as we analyse each GW injection as a separate event before computing a joint posterior.

The priors used to compute the likelihood (Eq. 2.14) are delta functions for the masses, spins, orientation and polarization angles (θ_{jn}, ψ) , and time and phase at coalescence (t_c, ϕ_c) . We use Bilby’s default prior distributions for the sky location (α and δ) and uniform priors for d_L . The priors for the $\vec{\lambda}$ parameters span the entire parameter space allowed after imposing a constraint corresponding to Eq. 2.9.

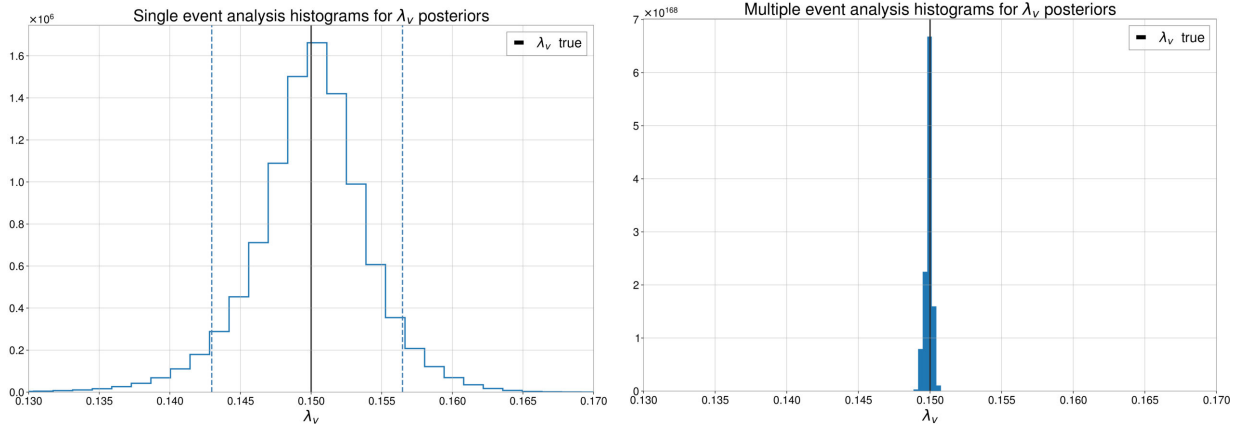


Figure 3.21: λ_v posterior probability distribution histograms for Single (left) and Multiple Event Analysis (right) from 149 tvs polarized GW injections with true values $\lambda_t = 0.2$, $\lambda_v = 0.15$ and $\lambda_s = 0.3$.

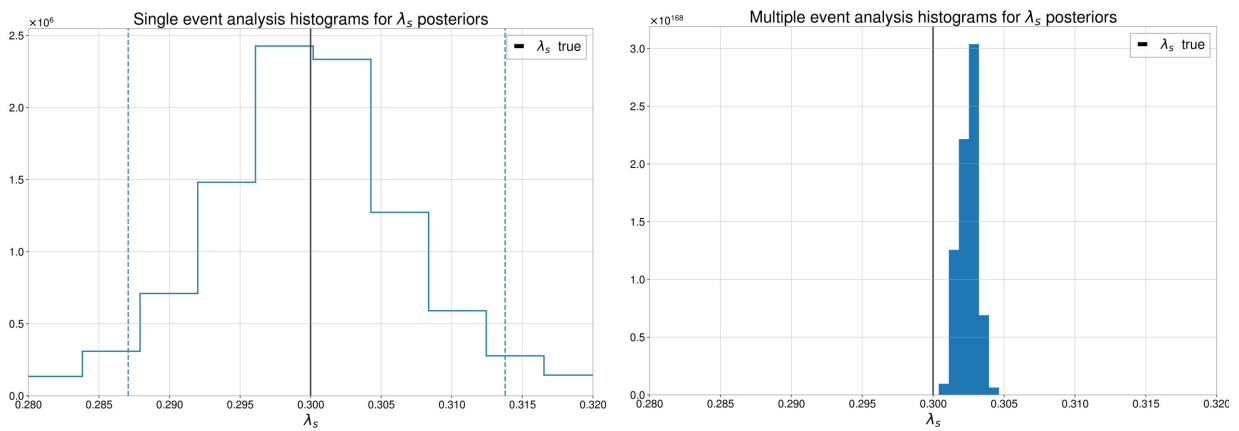


Figure 3.22: λ_s posterior probability distribution histograms for single (left) and Multiple Event Analysis from 149 tvs polarized GW injections with true values $\lambda_t = 0.2$, $\lambda_v = 0.15$ and $\lambda_s = 0.3$.

Summary, Conclusion and Future Work

4.1 Summary

In this thesis, we demonstrate the ability to examine beyond GR regimes and test the GW polarization prediction of GR against those of alternate metric gravitational theories by searching for non-tensorial GW polarization modes.

We address the accuracy and precision with which we can recover the small admixtures of non-tensorial (or non-GR) polarization components in tensor-vector-scalar (tvs) polarized, transient GWs from BBH CBCs. This thesis is future oriented and uses simulated data from a ground-based network of five non-co-oriented GW detectors which would only be available in 2026.

This study is a part of a larger, high risk high reward effort to challenge the completeness of GR and possibly modify GR into a more generalized theory of gravity. We do not expect GR to be violated and the detection of non-tensorial GW polarizations is unlikely, but potentially a spectacular probe for new physics.

Chapter 1 discusses how resolving the polarization content of GWs by searching for admixtures of vector and/or scalar GW polarization modes (as predicted by alternate metric gravitational theories) challenges the existing GR theoretical framework and can lead to a more generalized theory of gravity. It also provides a brief description of the six possible GW polarization modes predicted by the general metric theory of gravity, how each of these modes causes a different geometric response in the DARM of a single ground-based GW detector, and how a network of non-co-oriented GW detectors can resolve polarization degeneracies.

Chapter 2 defines the constrained, linearized $\vec{\lambda}$ parameters (λ_t , λ_v and λ_s) that we use to quantify the fraction of tensor, vector and scalar polarization components in a BBH GW signal (Eqs. 2.9 and 2.10) and outlines our assumption that vector and scalar polarization waveforms are similar to the tensor polarized waveform and differ only in amplitude and phase (Eqs. 2.4 - 2.8). Although this assumption is known to be false, it represents a near worst case scenario for placing upper limits on the detection sensitivity of the vector and scalar polarization admixtures by compelling us to use only the geometrical effect of the GW in the non-co-oriented detector network to distinguish between polarization modes. The chapter also overviews how we generate BBH tvs polarized GW waveforms, simulate GW detectors, and use Bayesian inference parameter estimation and nested sampling to extract the $\vec{\lambda}$ parameters from simulated data and to quantify the GW detection

sensitivity in a network of GW detectors.

Chapter 3 explains in further detail the parameters of the GWs which are fixed or varied for the Bayesian inference parameter estimation. For most of the thesis, the parameters for masses, spins, orientation angle (θ_{jn}), polarization angle (ψ), time and phase at coalescence (t_c, ϕ_c) of the spinless BBHs are “fixed” at their true values (i.e., they are delta functions at their true values outlined in Table 3.1) in the Bayesian parameter estimation. It presents the violin plots of $\vec{\lambda}$ posterior distributions for the GW parameter estimation jobs outlined in Tables 2.5 and 2.6.

The one-dimensional λ posterior probability distributions and credible intervals are presented both graphically (as histograms) and in tabular form in the Appendix.

4.2 Conclusion

We quantify the dependence of polarization detection sensitivity for tvs, tv and ts polarized GWs on the polarization composition ($\vec{\lambda}$ parameters), sky location, and luminosity distance in a network of three, four and five GW detectors (corresponding to the GW parameter estimation jobs outlined in the first four rows of Table 2.5). The results of the study are shown as posterior probability distribution violins for the inferred $\vec{\lambda}$ posteriors versus the true $\vec{\lambda}$ parameter values.

The violin plots for the $\vec{\lambda}$ posteriors visually demonstrate that the recovered $\vec{\lambda}$ parameter values are accurate and precise as the posterior 90% credible intervals enclose the $\vec{\lambda}$ true values in almost all cases and the credible intervals narrow for a greater number of GW detectors and higher SNR signals.

A computationally intensive p-p plot of the of the recovered $\vec{\lambda}$ posteriors plotted against the true $\vec{\lambda}$ values is required to verify that x% credible intervals enclose the true value x% of the time and is left for future work.

Quantifying precision for recovered $\vec{\lambda}$ posteriors

We estimate the average of the range of the credible intervals for the recovered $\vec{\lambda}$ posteriors (for the first four rows in Table 2.5 which correspond to tvs polarized GWs in the violin plots 3.2 - 3.7 and corresponding credible interval Tables A.1 - A.6, the tv polarized GWs in the violin plots 3.8 - 3.10 and corresponding credible interval Tables A.7 and A.9, and the ts polarized GWs in the violin plots 3.11 - 3.13 and corresponding credible interval Tables A.10 and A.12).

The 90% credible intervals for our inferred $\vec{\lambda}$ posterior probability distributions reduce with increasing number of detectors and average at 0.094 for a three-detector network, 0.066 for a four-detector network and 0.044 for a five-detector network. This marks a 53% narrowing of the credible intervals (and consequent improvement in precision) from a three-detector network to a five-detector network.

The 90% credible intervals for our inferred $\vec{\lambda}$ posterior probability distributions also narrow with increasing SNR and on an average range from 0.14 for low SNR GWs ($8 \leq x \leq 35$), 0.05 for medium SNR GWs ($35 \leq x \leq 100$) and 0.001 for high SNR GWs ($x \geq 100$). This marks a 92% narrowing of the $\vec{\lambda}$ posterior credible intervals (and consequent improvement in precision) from a low SNR to a high SNR GW signal.

However, observed BBH mergers usually have lower SNRs. Thus, it is notable that the major improvement in precision for a five-detector network corresponds to the low SNR regime. Averaging over low SNR GWs, the 90% credible intervals for our inferred $\vec{\lambda}$ posteriors range from 0.187 for a three-detector network, 0.141 for a four-detector network, and 0.098 for a five-detector network. This marks a 48% narrowing of the low SNR GW $\vec{\lambda}$ posterior credible intervals (and consequent improvement in precision) from a three-detector network to a five-detector network.

Varying additional parameters in the Bayesian parameter inference

We expect that varying the mass, spin, orientation angle (θ_{jn}), polarization angle (ψ), time and phase at coalescence (t_c, ϕ_c) priors from their delta function distribution in the Bayesian parameter estimation would decrease both the accuracy and precision of our results. However, varying all possible parameters is prohibitively computationally intensive and beyond the scope of this thesis.

To verify that our results are not unrealistic, we allow one of these previously fixed priors, namely the polarization angle (ψ) prior, to vary in the Bayesian parameter estimation for a small number of jobs with tvs polarized GWs (outlined in rows five and six of Table 2.5) and quantify the effect of this uniform ψ prior distribution on our previous results.

We estimate the change in the average range of the credible intervals for the results in which the ψ prior distribution is varied uniformly in the Bayesian parameter estimation (corresponding to rows five and six of Table 2.5, namely tvs polarized GWs in the violin plots 3.14 - 3.19 and credible interval tables A.13- A.18) versus the previous results in which the ψ prior distribution is a delta function at its true value in the Bayesian parameter estimation (corresponding to the first two rows of Table 2.5, namely tvs polarized GWs in the violin plots 3.2 - 3.7 and credible interval tables A.1 - A.6).

The credible intervals slightly broaden (causing the precision to slightly worsen) when the prior ψ distribution is uniform and periodic $\in [0, \pi]$ as compared to when it is a delta function at its true value. When the ψ prior is uniformly varied, the 90% credible intervals increase by an average of 0.0045 from their previous values where the ψ prior is fixed. This marks a 5.6% broadening in the $\vec{\lambda}$ posterior credible intervals when the ψ prior distribution is chosen to be uniform and periodic instead of a delta function. The choice of the ψ prior distribution has almost equal effect on the precision of both λ_v and λ_s parameters.

However, we expect that varying the orientation angle (θ_{jn}) prior from its delta function distribution in the Bayesian parameter estimation would have a more significant impact on our results. Quantifying the effect on detection sensitivity by uniformly varying the prior $\theta_{jn} \in [0, \pi]$ in the Bayesian parameter estimation is left for future work.

Verifying that the method works for different BBH component mass values

The violin plots for the λ_v and λ_s posteriors in Figure 3.20 visually demonstrate that the recovered $\vec{\lambda}$ parameter values for all three different BBH masses are accurate and precise as the posterior 90% credible intervals enclose the $\vec{\lambda}$ true values in almost all cases. This implies that our methods work for different BBH component masses.

We expect the $\vec{\lambda}$ parameter estimation precision to decrease with increasing component masses. This is because, larger mass binaries merge at a lower frequency where the ground-based GW detectors have a smaller bandwidth due to seismic noise [34]. Moreover, the rate of events and the distance up to which signals can be detected also change as a function of the binary masses and can affect the precision.

However, a more comprehensive analysis of the dependence of polarization sensitivity on BBH mass values is left for future work.

Multiple Event Analysis:

Polarization detection sensitivity if the fraction of vector and/or scalar polarization content is constant for all GW radiation

Under the hypothesis that the polarization $\vec{\lambda}$ parameters are shared between different GW detections and are independent of other parameters and properties of the BBH merger, we generate joint one-dimensional λ posterior probability distributions for 149 such GW events by marginalizing over all other parameters. This enables us to explore the possibility that the fraction of vector and/or scalar polarization content is constant for all GW radiation.

The $\vec{\lambda}$ posterior probability distribution histograms for the Single versus Multiple Event Analysis for 149 different GWs in five detectors (Figures 3.21 and 3.22) indicate that results from the Multiple Event Analysis have better precision as the statistical errors reach the sub 1% level.

However, in the Multiple Event Analysis for λ_s posterior in Figure 3.22, we observe a bias in the accuracy due to systematic errors as the precision increases. Thus, in the regime where the statistical error reaches a sub 1% level (the width of the λ_s posterior in Figure 3.22 marks a statistical error of about 0.3%) subtle systematic errors dominate and must be considered.

Systematic Errors

The most probable sources of systematic error in our simulated study are the Bayesian analysis and the method by which results from multiple events are combined to generate a joint posterior. In a real event, however, the major sources of systematic errors include the LIGO calibrated response to a GW signal at 2% accuracy, the LIGO waveform model at 1% accuracy, and the LIGO noise model at 1-2% accuracy.

4.3 Future work

Near-term future work involves looking for evidence of the presence of vector and/or scalar GW polarization components in BBH mergers observed from three or more (ideally five) detectors.

To further benefit such a study, the limit on non-tensor GW polarization admixtures should be estimated in an even more realistic, computationally rigorous manner by allowing the mass, spin, orientation angle (θ_{jn}), time and phase at coalescence (t_c, ϕ_c) priors to vary from their delta function distributions in the Bayesian parameter estimation.

Moreover, the computationally intensive p-p plot of the recovered $\vec{\lambda}$ posteriors versus the true $\vec{\lambda}$ values should be plotted and analyzed to verify that $\vec{\lambda}$ posterior x% credible intervals enclose the true $\vec{\lambda}$ values x% of the time.

Furthermore, long term future work involves constraining the limit on non-tensor GW polarization admixtures arbitrarily well. This can be achieved by developing the true vector and scalar polarized GW waveforms either through a theoretical framework for non-tensor GW waveforms or by reconstructing the vector and scalar waveforms from observational data [12]. If the true vector and scalar waveforms are known, the nested sampler can use a waveform template in addition to the geometrical effect of the GW in the non-co-oriented detector network to distinguish between polarization modes. This crucial additional information could drastically improve our polarization detector sensitivity.

Searching for non-tensorial beyond GR polarizations is part of a larger effort to advance our understanding of gravity in the strong-field, highly dynamic regime. In the case that such admixtures of non-tensor GW polarizations are observed, we must strive to understand the physics behind them.

BIBLIOGRAPHY

- [1] B. P. Abbott et al. “Observation of Gravitational Waves from a Binary Black Hole Merger”. In: *Phys. Rev. Lett.* 116 (6 Feb. 2016), p. 061102. doi: 10.1103/PhysRevLett.116.061102.
- [2] B. P. Abbott et al. “GW151226: Observation of Gravitational Waves from a 22-Solar-Mass Binary Black Hole Coalescence”. In: *Phys. Rev. Lett.* 116 (24 June 2016), p. 241103. doi: 10.1103/PhysRevLett.116.241103.
- [3] B. P. Abbott et al. “Binary Black Hole Mergers in the First Advanced LIGO Observing Run”. In: *Phys. Rev. X* 6 (4 Oct. 2016), p. 041015. doi: 10.1103/PhysRevX.6.041015.
- [4] B. P. Abbott et al. “GWTC-1: A Gravitational-Wave Transient Catalog of Compact Binary Mergers Observed by LIGO and Virgo during the First and Second Observing Runs”. In: *Phys. Rev. X* 9 (3 Sept. 2019), p. 031040. doi: 10.1103/PhysRevX.9.031040.
- [5] B. P. Abbott et al. “Tests of general relativity with the binary black hole signals from the LIGO-Virgo catalog GWTC-1”. In: *Phys. Rev. D* 100 (10 Nov. 2019), p. 104036. doi: 10.1103/PhysRevD.100.104036.
- [6] C. M. Will. *Theory and Experiment in Gravitational Physics, second edition*. New York, NY, USA: Cambridge University Press, 2018.
- [7] C. M. Will. “The Confrontation between General Relativity and Experiment”. In: *Living Rev. Relativ.* 17 (4 Dec. 2014). doi: 10.12942/lrr-2014-4.
- [8] M. Isi, M. Pitkin, and A. J. Weinstein. “Probing dynamical gravity with the polarization of continuous gravitational waves”. In: *Phys. Rev. D* 96 (4 Aug. 2017), p. 042001. doi: 10.1103/PhysRevD.96.042001.
- [9] B. P. Abbott et al. “GW170814: A Three-Detector Observation of Gravitational Waves from a Binary Black Hole Coalescence”. In: *Phys. Rev. Lett.* 119 (14 Oct. 2017), p. 141101. doi: 10.1103/PhysRevLett.119.141101.
- [10] R. C. Hilborn. “GW170814: Gravitational wave polarization analysis”. In: (2018). arXiv: 1802.01193.
- [11] T. Baker et al. “Strong Constraints on Cosmological Gravity from GW170817 and GRB 170817A”. In: *Phys. Rev. Lett.* 119 (25 Dec. 2017), p. 251301. doi: 10.1103/PhysRevLett.119.251301.
- [12] K. Chatziioannou, N. Yunes, and N. Cornish. “Model-independent test of general relativity: An extended post-Einsteinian framework with complete polarization content”. In: *Phys. Rev. D* 86 (2 July 2012), p. 022004. doi: 10.1103/PhysRevD.86.022004.
- [13] M. Isi and A. J. Weinstein. “Probing gravitational wave polarizations with signals from compact binary coalescences”. In: (2017). arXiv: 1710.03794.
- [14] J. M. Weisberg, D. J. Nice, and J. H. Taylor. “Timing Measurements of the Relativistic Binary Pulsar PSR B1913+16”. In: (2010). arXiv: 1011.0718.

- [15] P. C. C. Freire et al. “The relativistic pulsar–white dwarf binary PSR J1738+0333 – II. The most stringent test of scalar–tensor gravity”. In: *Monthly Notices of the Royal Astronomical Society* 423.4 (July 2012), pp. 3328–3343. ISSN: 0035-8711. DOI: 10.1111/j.1365-2966.2012.21253.x.
- [16] I.H. Stairs. “Testing General Relativity with Pulsar Timing”. In: *Living Rev. Relativ.* 6 (5 Sept. 2003). DOI: 10.12942/lrr-2003-5.
- [17] N. Wex. “Testing Relativistic Gravity with Radio Pulsars”. In: (2014). arXiv: 1402.5594.
- [18] Z. Berezhiani et al. “Spontaneous Lorentz Breaking and Massive Gravity”. In: *Phys. Rev. Lett.* 99 (13 Sept. 2007), p. 131101. DOI: 10.1103/PhysRevLett.99.131101.
- [19] S.F. Hassan, A. Schmidt-May, and M. von Strauss. “On consistent theories of massive spin-2 fields coupled to gravity”. In: *Journal of High Energy Physics* 2013.5 (May 2013). ISSN: 1029-8479. DOI: 10.1007/jhep05(2013)086.
- [20] K. Max, M. Platscher, and J. Smirnov. “Gravitational Wave Oscillations in Bigravity”. In: *Physical Review Letters* 119.11 (Sept. 2017). ISSN: 1079-7114. DOI: 10.1103/physrevlett.119.111101.
- [21] P. Brax, A. C. Davis, and J. Noller. “Gravitational Waves in Doubly Coupled Bigravity”. In: (2017). arXiv: 1703.08016.
- [22] D. M. Eardley, D. L. Lee, and A. P. Lightman. “Gravitational-Wave Observations as a Tool for Testing Relativistic Gravity”. In: *Phys. Rev. D* 8 (10 Nov. 1973), pp. 3308–3321. DOI: 10.1103/PhysRevD.8.3308.
- [23] T. Callister et al. “Polarization-Based Tests of Gravity with the Stochastic Gravitational-Wave Background”. In: *Physical Review X* 7.4 (Dec. 2017). ISSN: 2160-3308. DOI: 10.1103/physrevx.7.041058.
- [24] K. S. Thorne, D. L. Lee, and A. P. Lightman. “Foundations for a Theory of Gravitation Theories”. In: *Phys. Rev. D* 7 (12 June 1973), pp. 3563–3578. DOI: 10.1103/PhysRevD.7.3563.
- [25] C. Brans and R. H. Dicke. “Mach’s Principle and a Relativistic Theory of Gravitation”. In: *Phys. Rev.* 124 (3 Nov. 1961). DOI: 10.1103/PhysRev.124.925.
- [26] D. Andriot and G. L. Gómez. “Signatures of extra dimensions in gravitational waves”. In: *Journal of Cosmology and Astroparticle Physics* 2017.06 (June 2017). ISSN: 1475-7516. DOI: 10.1088/1475-7516/2017/06/048.
- [27] C. de Rham. “Massive Gravity”. In: *Living Rev. Relativ* 17 (7 Dec. 2014). DOI: 10.12942/lrr-2014-7.
- [28] N. Rosen. “A theory of gravitation”. In: *Annals of Physics* 84.1 (Dec. 1974), pp. 455–473. DOI: 10.1016/0003-4916(74)90311-X.
- [29] A. P. Lightman and D. L. Lee. “New Two-Metric Theory of Gravity with Prior Geometry”. In: *Phys. Rev. D* 8 (10 Nov. 1973), pp. 3293–3302. DOI: 10.1103/PhysRevD.8.3293.
- [30] C. Mead. “Gravitational Waves in G4v”. In: (2015). arXiv: 1503.04866.

- [31] A. Nishizawa et al. “Probing nontensorial polarizations of stochastic gravitational-wave backgrounds with ground-based laser interferometers”. In: *Phys. Rev. D* 79 (8 Apr. 2009), p. 082002. DOI: 10.1103/PhysRevD.79.082002.
- [32] S. Patrone. “Gravitational wave polarizations: a test for general relativity”. In: *SURF seminar* (Aug. 2019). URL: <https://caltech.app.box.com/s/9ms8yzmeku9egd5wrhnbuqf7g2tn97s1>.
- [33] M. Blagojevic. “Three lectures on Poincare gauge theory”. In: (2003). arXiv: gr-qc/0302040 [gr-qc].
- [34] D. V. Martynov et al. “The Sensitivity of the Advanced LIGO Detectors at the Beginning of Gravitational Wave Astronomy”. In: (2016). arXiv: 1604.00439 [astro-ph.IM].
- [35] P. Eric and C. M. Will. *Gravity: Newtonian, Post-Newtonian, Relativistic*. New York, NY, USA: Cambridge University Press, 2014.
- [36] *Gallery*. Laser Interferometer Gravitational-wave Observatory (LIGO) public web site. URL: <https://www.ligo.caltech.edu/images>.
- [37] *LIGO O3 run summary*. Laser Interferometer Gravitational-wave Observatory (LIGO) web site. URL: <https://summary.ligo.org/~detchar/summary/1238166018-1259193618/>.
- [38] LIGO Scientific Collaboration. *LIGO Algorithm Library - LALSuite*. free software (GPL). 2018. DOI: 10.7935/GT1W-FZ16.
- [39] B. S. Sathyaprakash and B. F. Schutz. *Physics, Astrophysics and Cosmology with Gravitational Waves*. 2009. arXiv: 0903.0338.
- [40] Gregory Ashton et al. “Bilby: A user-friendly Bayesian inference library for gravitational-wave astronomy”. In: (2018). arXiv: 1811.02042 [astro-ph.IM].
- [41] L. Barsotti et al. “The A+ design curve”. In: *LIGO Document T1800042-v5* (Oct. 2018). URL: <https://dcc.ligo.org/LIGO-T1800042/public>.
- [42] S. J. Waldman. “The Advanced LIGO Gravitational Wave Detector”. In: (2011). arXiv: 1103.2728 [gr-qc].
- [43] J. Hough et al. “Third generation gravitational-wave observatories and their science reach”. In: *General Relativity and Gravitation* 43 (Feb. 2010), pp. 361–362. DOI: 10.1007/s10714-010-1130-1.
- [44] E. Berti, V. Cardoso, and C. M. Will. “On gravitational-wave spectroscopy of massive black holes with the space interferometer LISA”. In: (2005). arXiv: gr-qc/0512160 [gr-qc].
- [45] D. Thain, T. Tannenbaum, and M. Livny. “Distributed computing in practice: the Condor experience”. In: *Concurrency - Practice and Experience* 17.2-4 (2005), pp. 323–356. DOI: 10.1002/cpe.938.

Appendix A

Single Event Analysis

The λ_v and λ_s violin plots are sufficient to visually confirm that the results in chapter 3 are accurate and precise.

In addition to the violin plots, we present the one-dimensional posterior probability distributions histograms of the inferred $\vec{\lambda}$ posteriors versus the injected $\vec{\lambda}$ values and the 90% credible interval tables for the various sets of 528 jobs outlined in Table 2.5 and the 9 jobs outlined in the first row of Table 2.6. These histograms and credible interval tables essentially convey the same information presented in the violin plots.

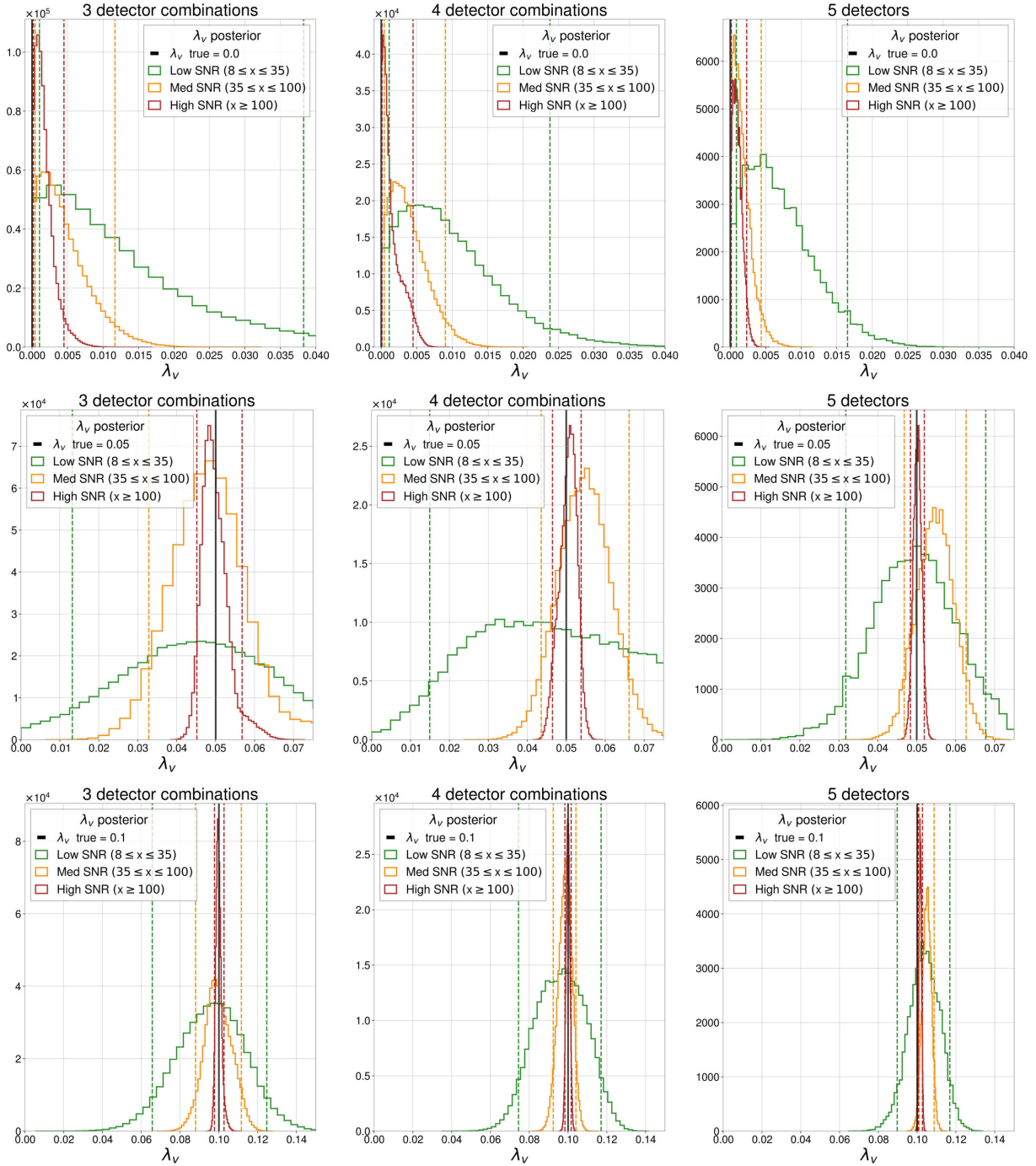
Each histogram in this section is created through a Single Event Analysis. That is, λ_t , λ_v and λ_s probability distributions are extracted from each individual event through a separate evaluation of the posterior.

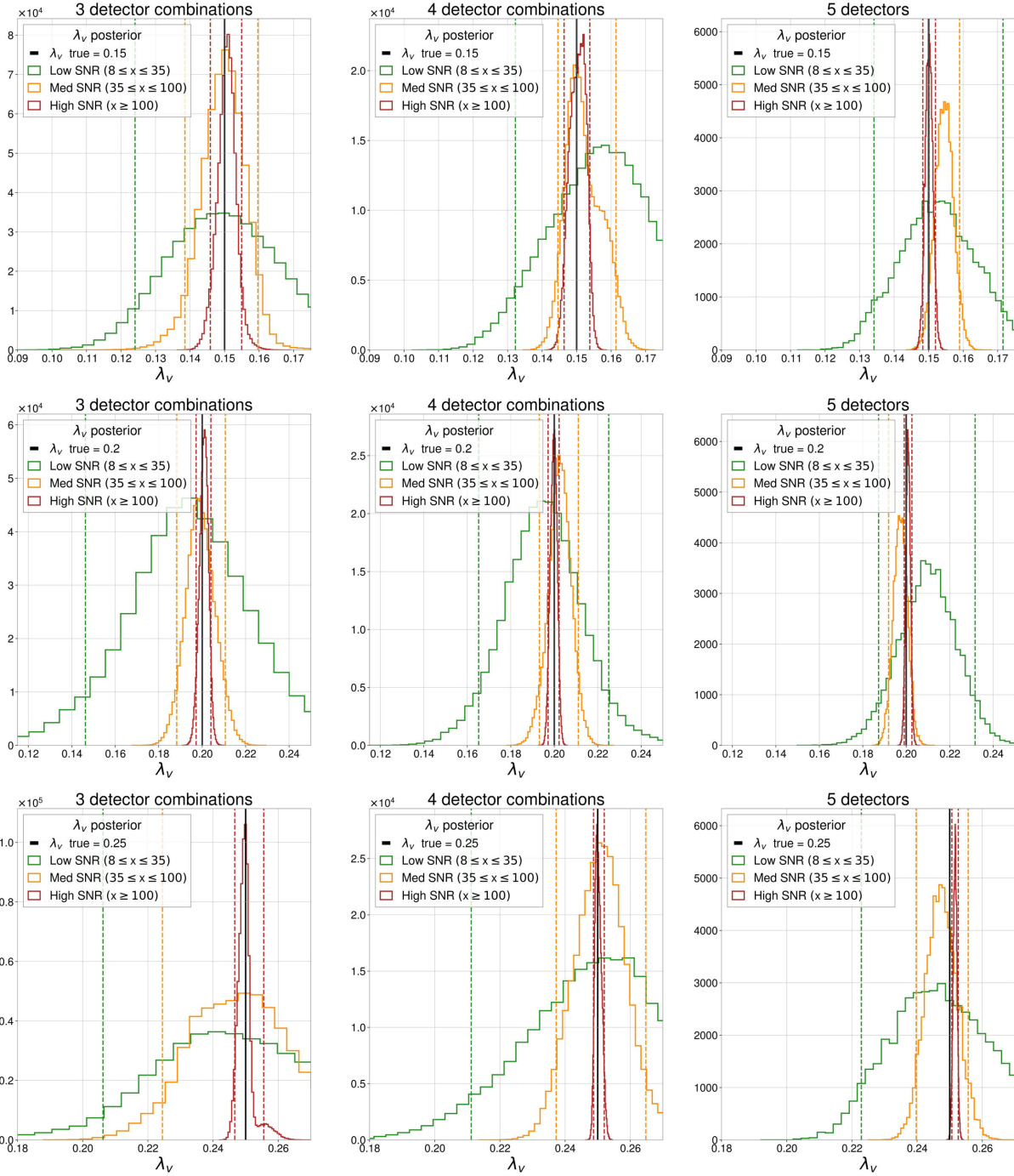
A.1 Tensor-Vector-Scalar (tvs) polarized GWs

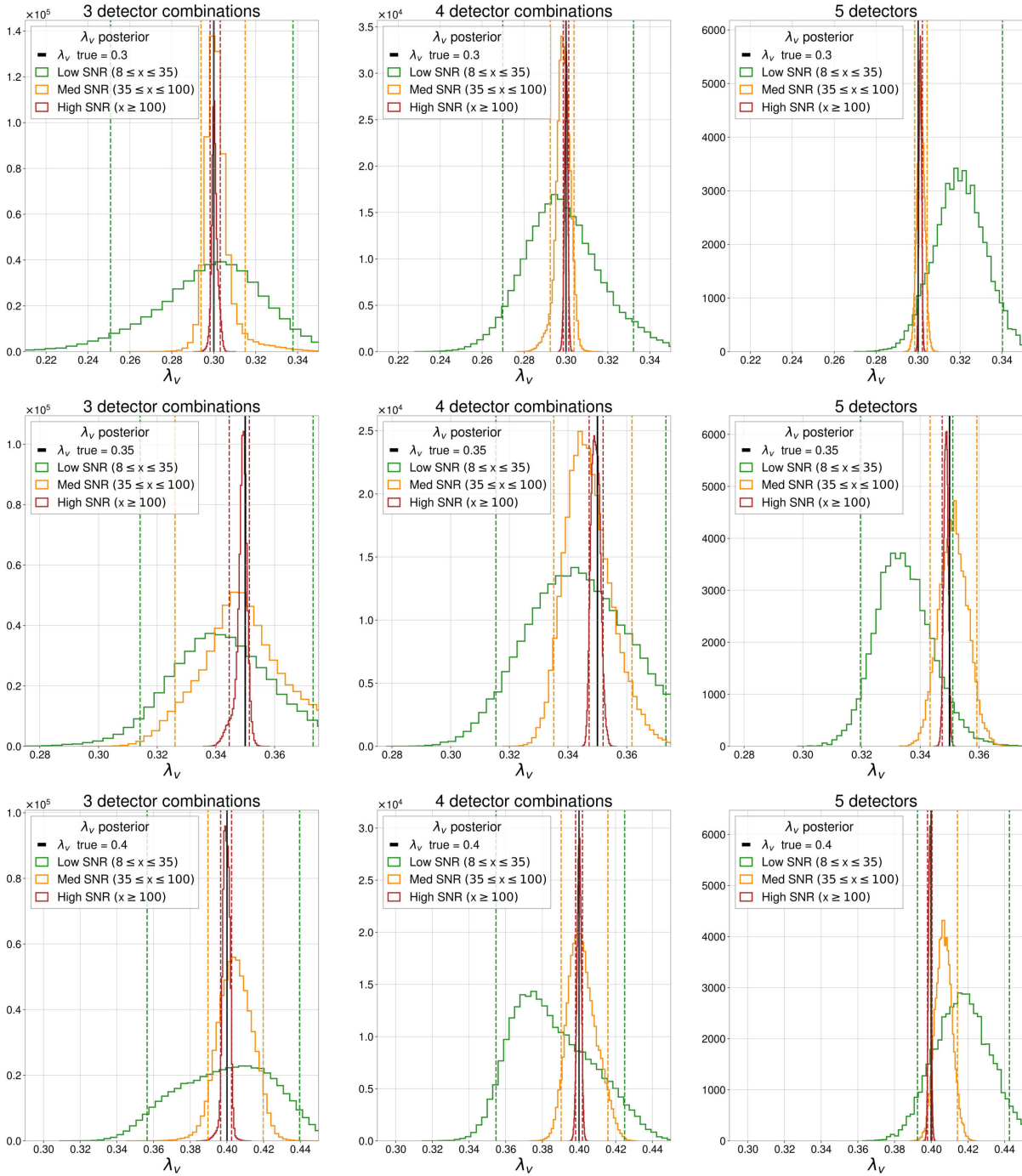
λ_v posterior for tvs polarized GWs; fixed ψ prior

In the following Figure A.1, we plot histograms of λ_v posterior probability distributions for tvs polarized GWs. The rows step through 11 progressively increasing values of $\lambda_v \in [0, 0.5]$. The remaining polarization content is randomly distributed between tensor (λ_t) and scalar (λ_s) components as per the constraint in Equation 2.9.

The 90% credible intervals for the λ_v and λ_s posterior probability distributions are given in Tables A.1 and A.3 respectively. Moreover, the 90% upper and lower limits for the λ_v posterior probability distributions (corresponding to true values $\lambda_v = 0.0$ and $\lambda_v = 0.5$ respectively) are given in Table A.2.







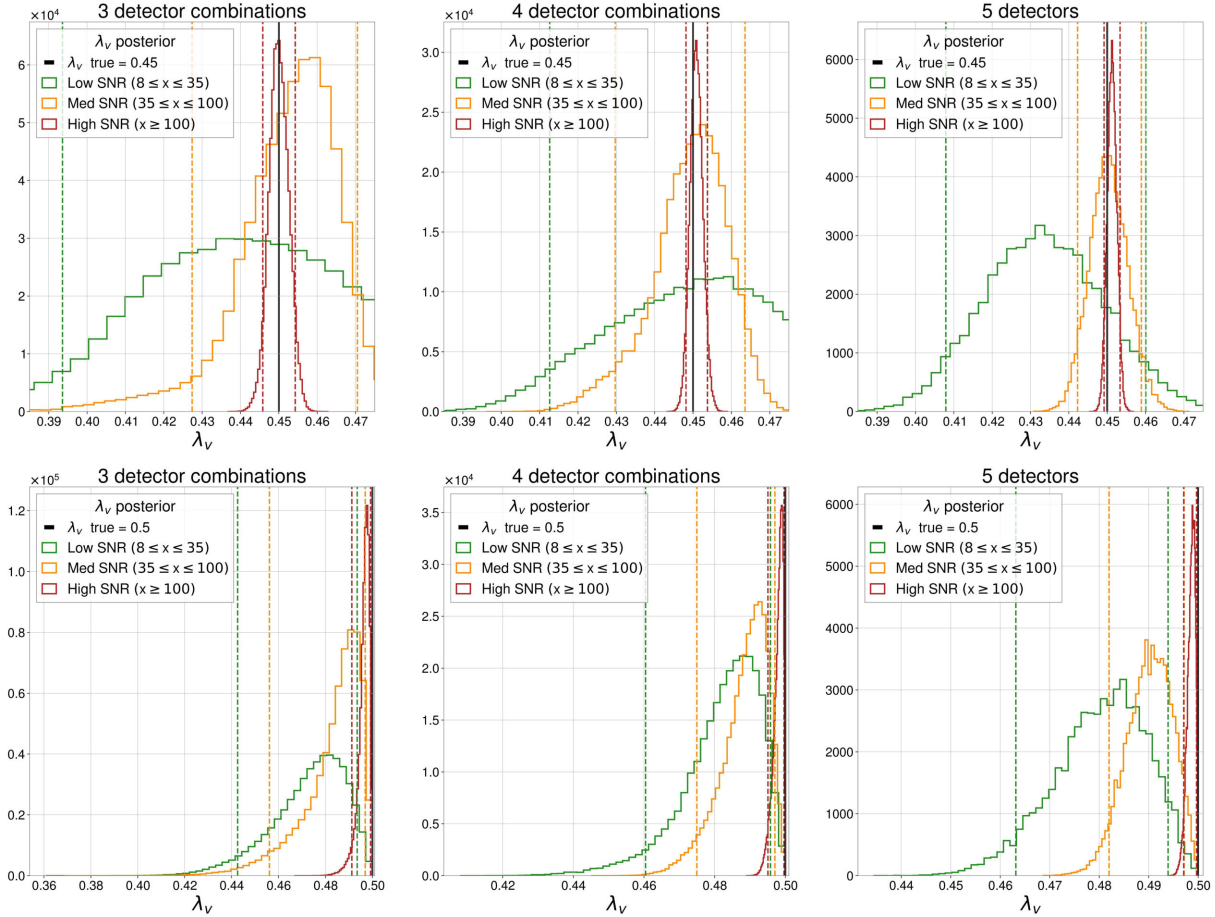


Figure A.1: Histograms of λ_v posteriors for tvs polarized GWs averaged over all possible three (left), four (middle) and five (right) detector combinations for low, medium and high SNRs (corresponding to Figures 3.2, 3.3 and 3.4 respectively). The rows step through 11 progressively increasing values of $\lambda_v \in [0, 0.5]$. The remaining polarization content is randomly distributed between tensor (λ_t) and scalar (λ_s) components as per the constraint in Equation 2.9. Each histogram corresponds to an injection with a randomly chosen sky location and polarization angle (ψ).

λ_v true	SNR	3 detectors	4 detectors	5 detectors
0.0	Low	$0.01^{+0.03}_{-0.009}$	$0.01^{+0.02}_{-0.007}$	$0.01^{+0.01}_{-0.005}$
	Med	$0.004^{+0.008}_{-0.003}$	$0.003^{+0.006}_{-0.003}$	$0.001^{+0.003}_{-0.001}$
	High	$0.001^{+0.003}_{-0.001}$	$0.001^{+0.003}_{-0.001}$	$0.001^{+0.001}_{-0.0008}$
0.05	Low	$0.05^{+0.03}_{-0.03}$	$0.05^{+0.04}_{-0.03}$	$0.05^{+0.02}_{-0.02}$
	Med	$0.05^{+0.04}_{-0.02}$	$0.05^{+0.01}_{-0.01}$	$0.055^{+0.008}_{-0.008}$
	High	$0.049^{+0.007}_{-0.004}$	$0.051^{+0.003}_{-0.004}$	$0.050^{+0.002}_{-0.002}$
0.1	Low	$0.10^{+0.03}_{-0.03}$	$0.10^{+0.02}_{-0.02}$	$0.10^{+0.01}_{-0.01}$
	Med	$0.10^{+0.01}_{-0.01}$	$0.099^{+0.005}_{-0.006}$	$0.105^{+0.004}_{-0.004}$
	High	$0.100^{+0.003}_{-0.002}$	$0.100^{+0.002}_{-0.002}$	$0.102^{+0.001}_{-0.001}$
0.15	Low	$0.15^{+0.03}_{-0.03}$	$0.16^{+0.02}_{-0.02}$	$0.15^{+0.02}_{-0.02}$
	Med	$0.15^{+0.01}_{-0.01}$	$0.15^{+0.01}_{-0.007}$	$0.155^{+0.004}_{-0.004}$
	High	$0.151^{+0.004}_{-0.005}$	$0.150^{+0.003}_{-0.004}$	$0.150^{+0.002}_{-0.002}$
0.2	Low	$0.20^{+0.08}_{-0.05}$	$0.20^{+0.03}_{-0.03}$	$0.21^{+0.02}_{-0.02}$
	Med	$0.20^{+0.01}_{-0.01}$	$0.203^{+0.009}_{-0.009}$	$0.197^{+0.005}_{-0.005}$
	High	$0.201^{+0.003}_{-0.004}$	$0.200^{+0.002}_{-0.003}$	$0.201^{+0.002}_{-0.002}$
0.25	Low	$0.25^{+0.05}_{-0.04}$	$0.25^{+0.03}_{-0.04}$	$0.25^{+0.03}_{-0.02}$
	Med	$0.25^{+0.04}_{-0.03}$	$0.25^{+0.01}_{-0.01}$	$0.247^{+0.008}_{-0.008}$
	High	$0.250^{+0.006}_{-0.003}$	$0.250^{+0.002}_{-0.001}$	$0.252^{+0.001}_{-0.001}$
0.3	Low	$0.30^{+0.04}_{-0.05}$	$0.30^{+0.03}_{-0.03}$	$0.32^{+0.02}_{-0.02}$
	Med	$0.30^{+0.01}_{-0.007}$	$0.299^{+0.005}_{-0.006}$	$0.301^{+0.003}_{-0.003}$
	High	$0.300^{+0.003}_{-0.002}$	$0.300^{+0.001}_{-0.001}$	$0.301^{+0.001}_{-0.001}$
0.35	Low	$0.34^{+0.03}_{-0.03}$	$0.34^{+0.03}_{-0.03}$	$0.33^{+0.02}_{-0.01}$
	Med	$0.35^{+0.03}_{-0.02}$	$0.35^{+0.02}_{-0.01}$	$0.351^{+0.008}_{-0.008}$
	High	$0.349^{+0.002}_{-0.005}$	$0.349^{+0.003}_{-0.002}$	$0.349^{+0.001}_{-0.001}$
0.4	Low	$0.40^{+0.04}_{-0.04}$	$0.38^{+0.04}_{-0.03}$	$0.42^{+0.03}_{-0.02}$
	Med	$0.40^{+0.02}_{-0.01}$	$0.40^{+0.01}_{-0.01}$	$0.407^{+0.007}_{-0.007}$
	High	$0.400^{+0.003}_{-0.003}$	$0.400^{+0.002}_{-0.002}$	$0.399^{+0.001}_{-0.001}$
0.45	Low	$0.44^{+0.04}_{-0.05}$	$0.45^{+0.03}_{-0.04}$	$0.43^{+0.03}_{-0.03}$
	Med	$0.45^{+0.02}_{-0.03}$	$0.45^{+0.01}_{-0.02}$	$0.450^{+0.009}_{-0.008}$
	High	$0.450^{+0.004}_{-0.004}$	$0.451^{+0.003}_{-0.003}$	$0.451^{+0.002}_{-0.002}$

λ_v true	SNR	3 detectors	4 detectors	5 detectors
0.5	Low	$0.48^{+0.02}_{-0.03}$	$0.48^{+0.01}_{-0.02}$	$0.48^{+0.01}_{-0.02}$
	Med	$0.49^{+0.01}_{-0.03}$	$0.49^{+0.007}_{-0.01}$	$0.490^{+0.007}_{-0.008}$
	High	$0.497^{+0.002}_{-0.006}$	$0.498^{+0.001}_{-0.003}$	$0.499^{+0.001}_{-0.002}$

Table A.1: Table of λ_v median and errors corresponding to a 90% credible interval for the posterior probability distributions in Figures 3.2, 3.3, 3.4 and Histograms in Figure A.1.

λ_v true	SNR	3 detectors	4 detectors	5 detectors
0.0	Low	0.03	0.02	0.014
	Med	0.01	0.007	0.003
	High	0.003	0.004	0.002
0.5	Low	0.46	0.46	0.47
	Med	0.47	0.48	0.483
	High	0.493	0.496	0.498

Table A.2: Table of λ_v posterior 90% upper (row 1) and lower (row 2) limits (corresponding to true values $\lambda_v = 0.0$ and $\lambda_v = 0.5$ respectively) in Figures 3.2, 3.3, 3.4.

λ_s true	SNR	3 detectors	4 detectors	5 detectors
0.7	Low	$0.69^{+0.06}_{-0.06}$	$0.68^{+0.05}_{-0.05}$	$0.68^{+0.03}_{-0.03}$
0.86	Low	$0.87^{+0.06}_{-0.06}$	$0.86^{+0.06}_{-0.07}$	$0.87^{+0.04}_{-0.04}$
0.53	Low	$0.52^{+0.08}_{-0.09}$	$0.53^{+0.06}_{-0.06}$	$0.55^{+0.04}_{-0.04}$
0.43	Low	$0.43^{+0.07}_{-0.07}$	$0.42^{+0.04}_{-0.05}$	$0.41^{+0.03}_{-0.03}$
0.37	Low	$0.4^{+0.1}_{-0.2}$	$0.38^{+0.05}_{-0.06}$	$0.39^{+0.04}_{-0.03}$
0.4	Low	$0.4^{+0.09}_{-0.1}$	$0.41^{+0.08}_{-0.08}$	$0.38^{+0.05}_{-0.07}$
0.1	Low	$0.08^{+0.09}_{-0.06}$	$0.10^{+0.05}_{-0.06}$	$0.08^{+0.03}_{-0.03}$
0.21	Low	$0.21^{+0.03}_{-0.03}$	$0.21^{+0.03}_{-0.04}$	$0.23^{+0.01}_{-0.01}$
0.12	Low	$0.1^{+0.1}_{-0.1}$	$0.2^{+0.08}_{-0.1}$	$0.09^{+0.05}_{-0.06}$
0.03	Low	$0.03^{+0.04}_{-0.03}$	$0.03^{+0.03}_{-0.03}$	$0.03^{+0.02}_{-0.02}$
0.0	Low	$0.03^{+0.06}_{-0.02}$	$0.02^{+0.05}_{-0.01}$	$0.02^{+0.03}_{-0.02}$

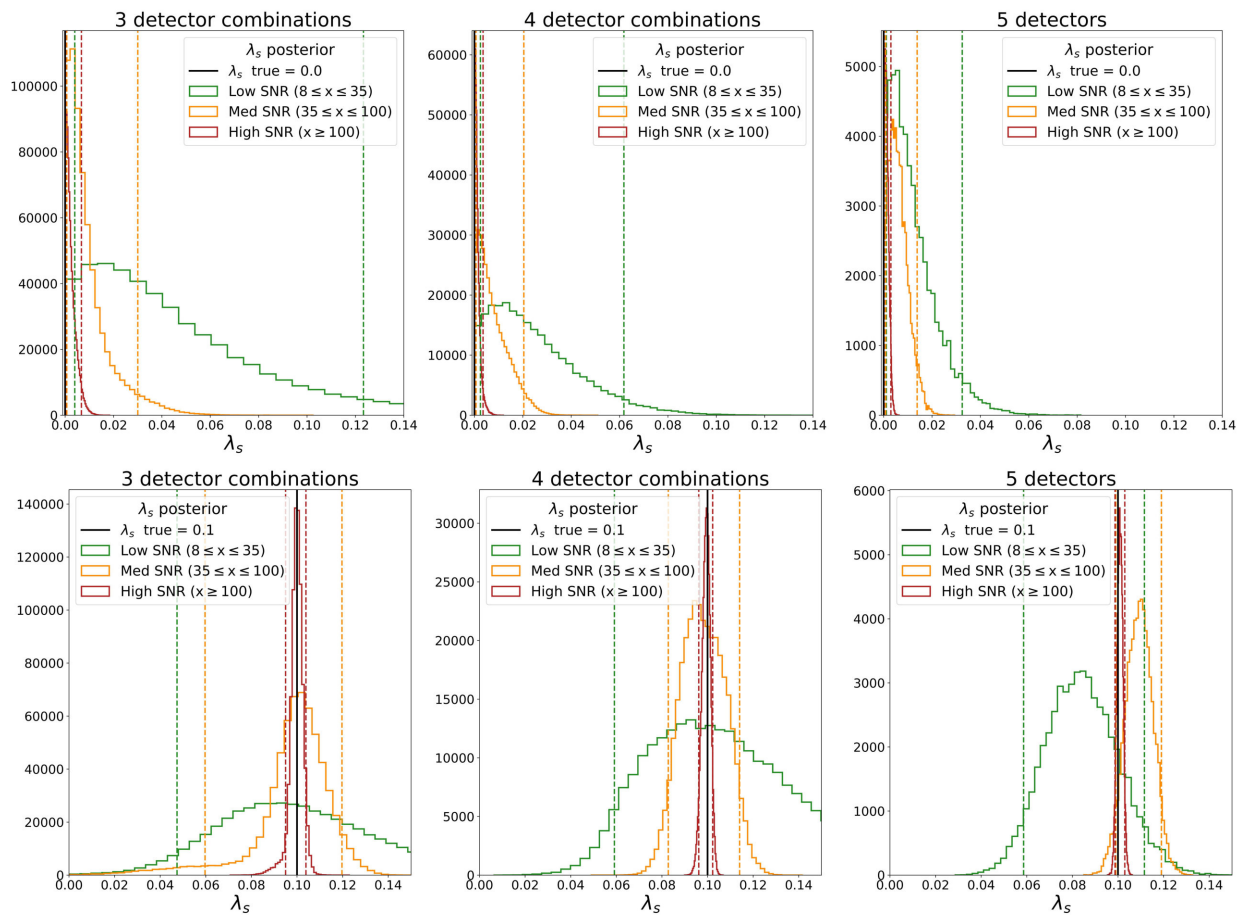
λ_s true	SNR	3 detectors	4 detectors	5 detectors
0.06	Med	$0.06^{+0.02}_{-0.02}$	$0.06^{+0.01}_{-0.01}$	$0.059^{+0.008}_{-0.008}$
0.36	Med	$0.36^{+0.03}_{-0.02}$	$0.36^{+0.01}_{-0.01}$	$0.354^{+0.008}_{-0.007}$
0.45	Med	$0.45^{+0.03}_{-0.03}$	$0.45^{+0.02}_{-0.01}$	$0.442^{+0.009}_{-0.008}$
0.38	Med	$0.38^{+0.02}_{-0.03}$	$0.38^{+0.02}_{-0.02}$	$0.377^{+0.009}_{-0.009}$
0.49	Med	$0.49^{+0.03}_{-0.02}$	$0.48^{+0.01}_{-0.01}$	$0.494^{+0.009}_{-0.009}$
0.33	Med	$0.33^{+0.03}_{-0.07}$	$0.33^{+0.01}_{-0.02}$	$0.33^{+0.01}_{-0.01}$
0.33	Med	$0.33^{+0.02}_{-0.03}$	$0.33^{+0.02}_{-0.02}$	$0.328^{+0.008}_{-0.008}$
0.18	Med	$0.18^{+0.04}_{-0.06}$	$0.18^{+0.03}_{-0.02}$	$0.18^{+0.01}_{-0.02}$
0.06	Med	$0.05^{+0.03}_{-0.04}$	$0.06^{+0.03}_{-0.04}$	$0.05^{+0.02}_{-0.02}$
0.05	Med	$0.04^{+0.05}_{-0.03}$	$0.05^{+0.03}_{-0.03}$	$0.05^{+0.02}_{-0.02}$
0.0	Med	$0.02^{+0.04}_{-0.01}$	$0.01^{+0.03}_{-0.01}$	$0.02^{+0.02}_{-0.01}$
0.75	High	$0.748^{+0.007}_{-0.008}$	$0.75^{+0.005}_{-0.01}$	$0.749^{+0.004}_{-0.004}$
0.1	High	$0.10^{+0.007}_{-0.02}$	$0.100^{+0.005}_{-0.005}$	$0.100^{+0.002}_{-0.002}$
0.4	High	$0.40^{+0.01}_{-0.01}$	$0.399^{+0.008}_{-0.006}$	$0.396^{+0.005}_{-0.004}$
0.24	High	$0.24^{+0.01}_{-0.01}$	$0.24^{+0.01}_{-0.01}$	$0.239^{+0.006}_{-0.006}$
0.36	High	$0.36^{+0.007}_{-0.01}$	$0.360^{+0.005}_{-0.005}$	$0.361^{+0.003}_{-0.003}$
0.22	High	$0.22^{+0.007}_{-0.01}$	$0.221^{+0.004}_{-0.005}$	$0.222^{+0.003}_{-0.003}$
0.29	High	$0.290^{+0.005}_{-0.004}$	$0.291^{+0.004}_{-0.003}$	$0.290^{+0.002}_{-0.002}$
0.3	High	$0.299^{+0.005}_{-0.005}$	$0.299^{+0.005}_{-0.004}$	$0.301^{+0.002}_{-0.002}$
0.04	High	$0.040^{+0.007}_{-0.005}$	$0.040^{+0.003}_{-0.003}$	$0.040^{+0.002}_{-0.002}$
0.06	High	$0.061^{+0.004}_{-0.004}$	$0.061^{+0.003}_{-0.003}$	$0.061^{+0.002}_{-0.002}$
0.0	High	$0.00^{+0.01}_{-0.002}$	$0.002^{+0.005}_{-0.002}$	$0.001^{+0.002}_{-0.0009}$

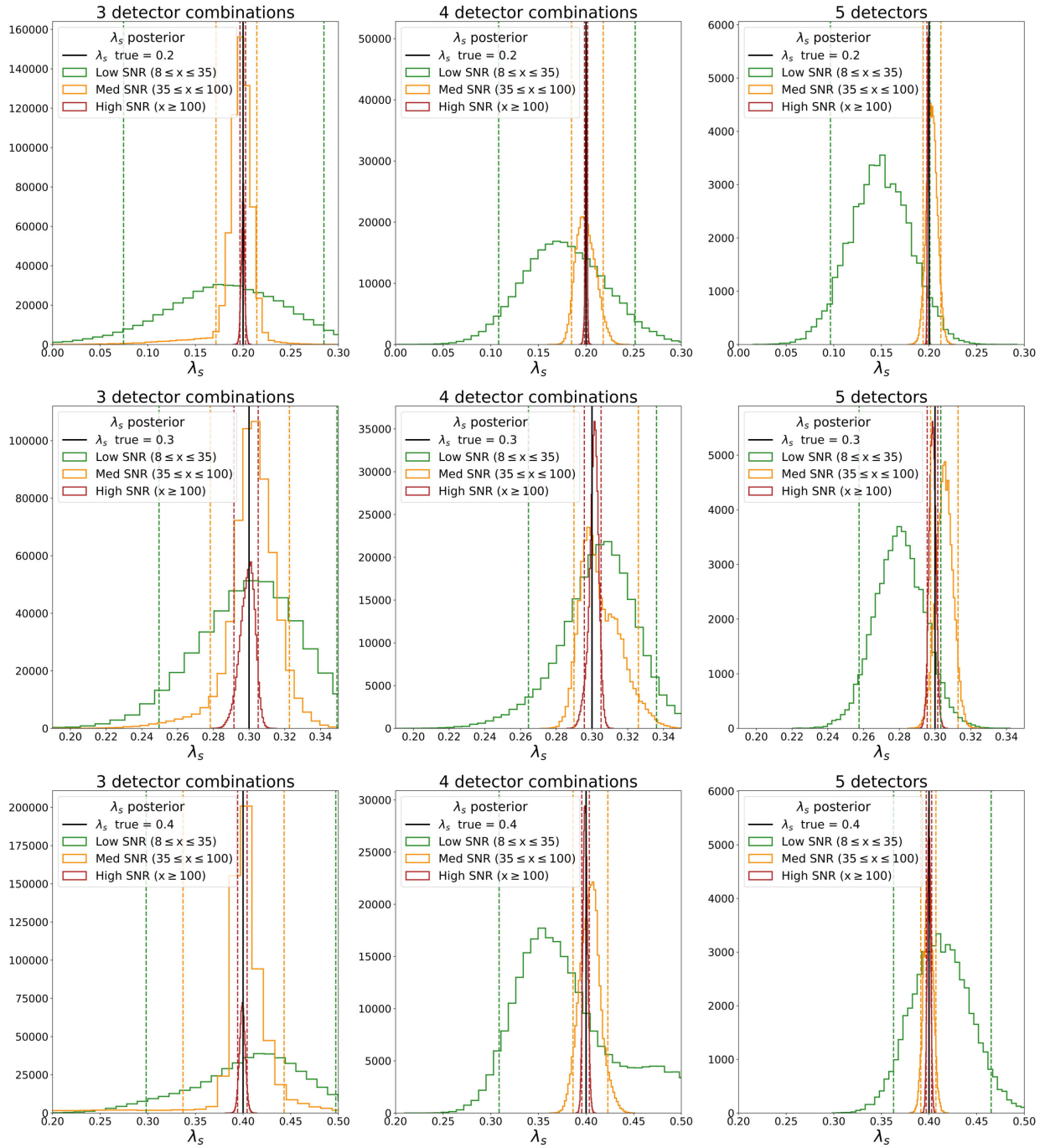
Table A.3: Table of λ_s median and errors corresponding to a 90% credible interval for the posterior probability distributions in Figures 3.2, 3.3, 3.4 and Histograms in Figure A.1.

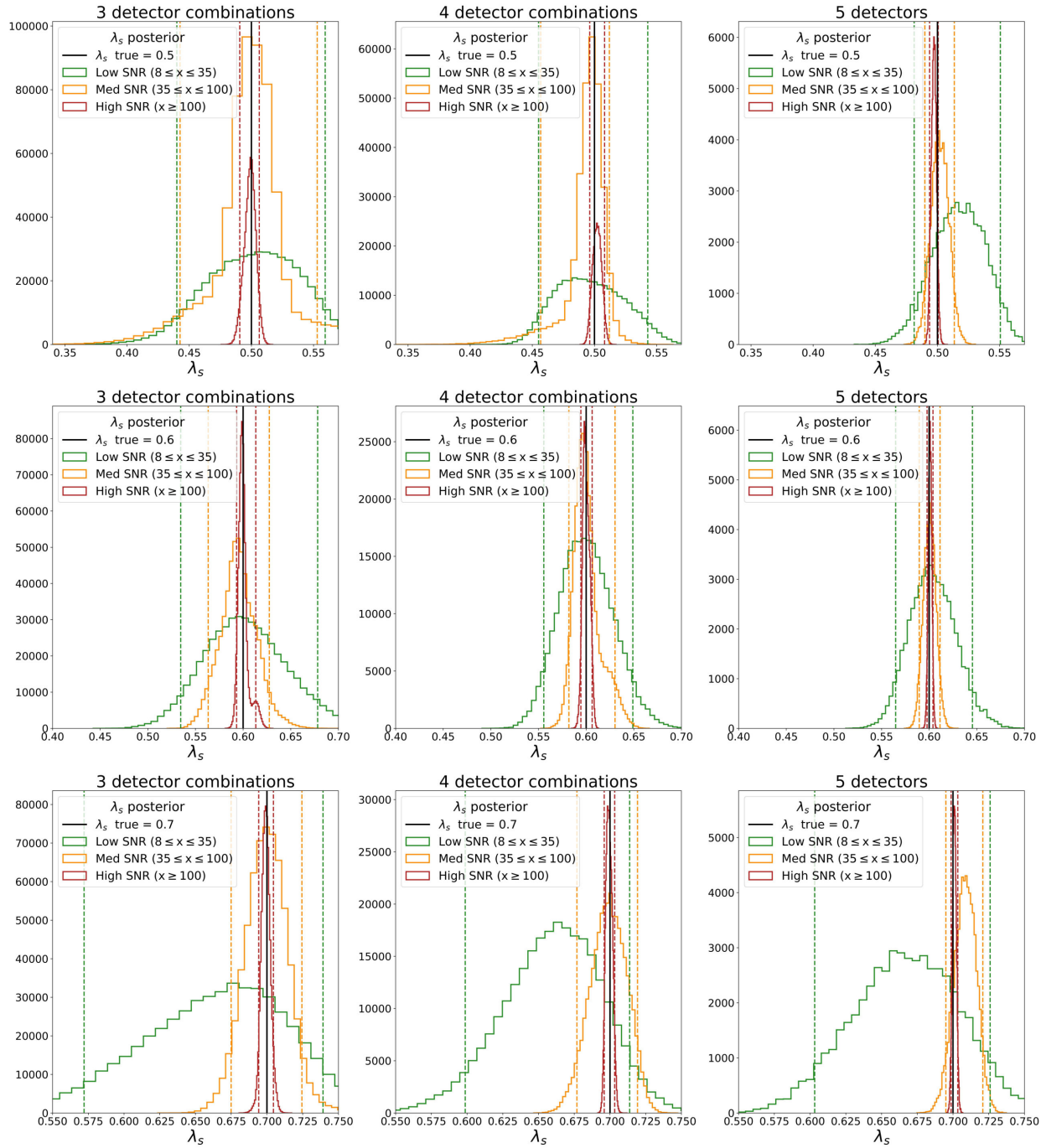
λ_s posterior for tvs polarized GWs; fixed ψ prior

In the following Figure A.2, we plot histograms of λ_s posterior probability distributions for tvs polarized GWs. The rows step through 11 progressively increasing values of $\lambda_s \in [0, 1]$. The remaining polarization content is randomly distributed between tensor (λ_t) and vector (λ_v) components as per the constraint in Equation 2.9.

The 90% credible intervals for the λ_s and λ_v posterior probability distributions are given in Tables A.4 and A.6 respectively. Moreover, the 90% upper and lower limits for the λ_s posterior probability distributions (corresponding to true values $\lambda_s = 0.0$ and $\lambda_s = 1.0$ respectively) are given in Table A.5.







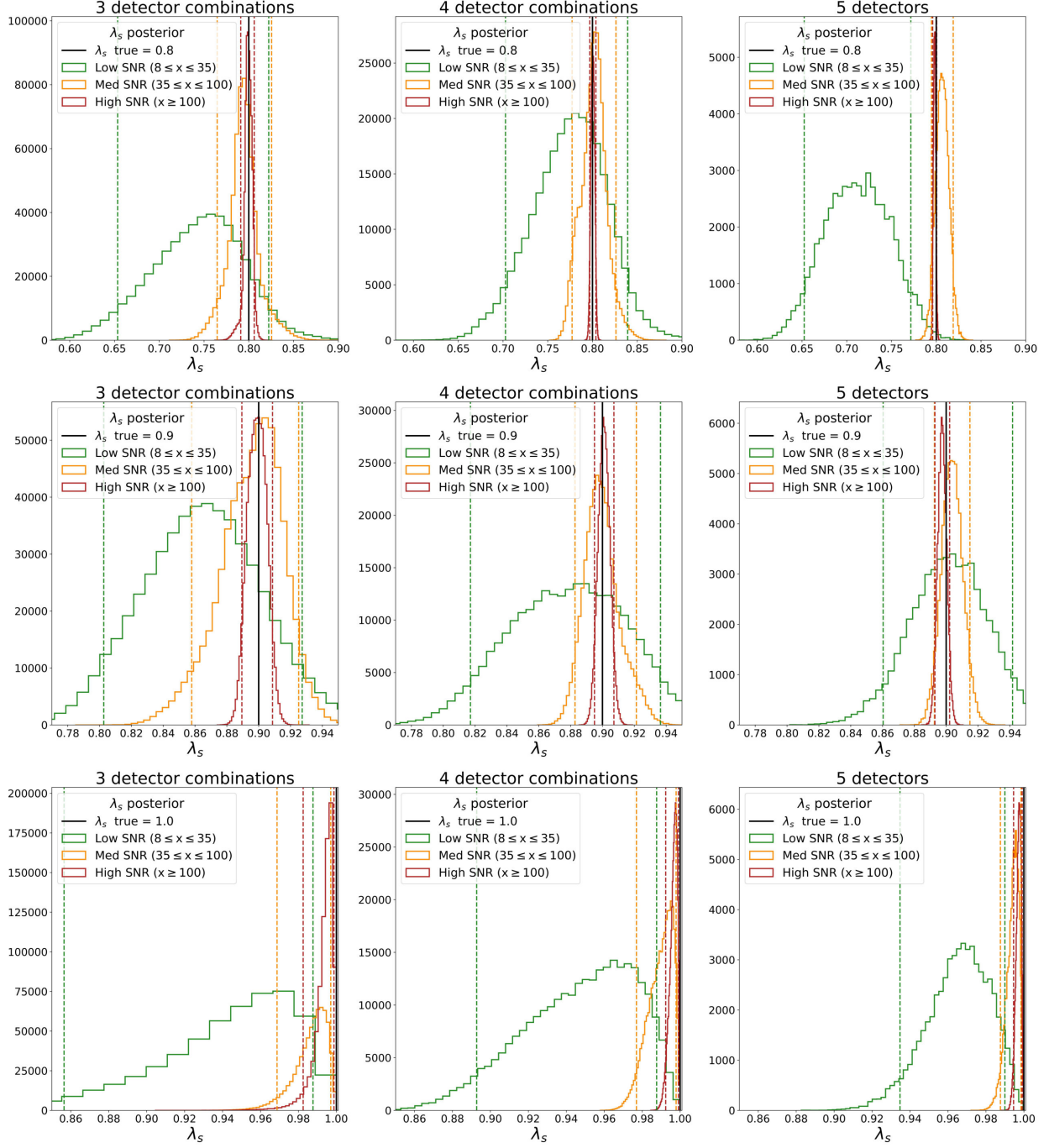


Figure A.2: Histograms of λ_s posteriors for tvs polarized GWs averaged over all possible three (left), four (middle) and five (right) detector combinations for low, medium and high SNRs (corresponding to Figures 3.5, 3.6 and 3.7 respectively). The rows step through 11 progressively increasing values of $\lambda_s \in [0, 1]$. The remaining polarization content is randomly distributed between tensor (λ_t) and vector (λ_v) components as per the constraint in Equation 2.9. Each histogram corresponds to an injection with a randomly chosen sky location and polarization angle (ψ).

λ_s true	SNR	3 detectors	4 detectors	5 detectors
0.0	Low	$0.04^{+0.09}_{-0.03}$	$0.02^{+0.04}_{-0.02}$	$0.01^{+0.02}_{-0.009}$
	Med	$0.01^{+0.02}_{-0.006}$	$0.01^{+0.01}_{-0.006}$	$0.006^{+0.008}_{-0.005}$
	High	$0.002^{+0.005}_{-0.002}$	$0.001^{+0.003}_{-0.0008}$	$0.001^{+0.002}_{-0.001}$
0.1	Low	$0.10^{+0.06}_{-0.05}$	$0.10^{+0.05}_{-0.04}$	$0.08^{+0.03}_{-0.03}$
	Med	$0.10^{+0.02}_{-0.04}$	$0.10^{+0.02}_{-0.02}$	$0.11^{+0.01}_{-0.01}$
	High	$0.100^{+0.004}_{-0.005}$	$0.099^{+0.003}_{-0.003}$	$0.101^{+0.002}_{-0.002}$
0.2	Low	$0.2^{+0.1}_{-0.1}$	$0.18^{+0.08}_{-0.07}$	$0.15^{+0.05}_{-0.05}$
	Med	$0.20^{+0.02}_{-0.03}$	$0.20^{+0.02}_{-0.01}$	$0.203^{+0.009}_{-0.009}$
	High	$0.200^{+0.003}_{-0.003}$	$0.200^{+0.001}_{-0.002}$	$0.199^{+0.001}_{-0.001}$
0.3	Low	$0.30^{+0.05}_{-0.05}$	$0.30^{+0.03}_{-0.04}$	$0.28^{+0.02}_{-0.02}$
	Med	$0.30^{+0.02}_{-0.02}$	$0.30^{+0.02}_{-0.01}$	$0.305^{+0.008}_{-0.008}$
	High	$0.299^{+0.006}_{-0.008}$	$0.301^{+0.004}_{-0.005}$	$0.299^{+0.003}_{-0.003}$
0.4	Low	$0.4^{+0.08}_{-0.1}$	$0.4^{+0.1}_{-0.06}$	$0.41^{+0.05}_{-0.05}$
	Med	$0.40^{+0.04}_{-0.06}$	$0.40^{+0.02}_{-0.02}$	$0.399^{+0.008}_{-0.008}$
	High	$0.399^{+0.005}_{-0.005}$	$0.399^{+0.004}_{-0.004}$	$0.400^{+0.003}_{-0.003}$
0.5	Low	$0.50^{+0.06}_{-0.06}$	$0.50^{+0.05}_{-0.04}$	$0.52^{+0.03}_{-0.04}$
	Med	$0.50^{+0.05}_{-0.06}$	$0.50^{+0.02}_{-0.04}$	$0.50^{+0.01}_{-0.01}$
	High	$0.499^{+0.007}_{-0.008}$	$0.502^{+0.006}_{-0.006}$	$0.497^{+0.003}_{-0.004}$
0.6	Low	$0.60^{+0.08}_{-0.07}$	$0.60^{+0.05}_{-0.04}$	$0.60^{+0.04}_{-0.04}$
	Med	$0.59^{+0.03}_{-0.03}$	$0.60^{+0.03}_{-0.02}$	$0.60^{+0.01}_{-0.01}$
	High	$0.60^{+0.01}_{-0.006}$	$0.600^{+0.007}_{-0.005}$	$0.601^{+0.003}_{-0.003}$
0.7	Low	$0.7^{+0.07}_{-0.1}$	$0.66^{+0.05}_{-0.06}$	$0.67^{+0.06}_{-0.06}$
	Med	$0.70^{+0.02}_{-0.02}$	$0.70^{+0.02}_{-0.02}$	$0.71^{+0.01}_{-0.01}$
	High	$0.699^{+0.005}_{-0.005}$	$0.699^{+0.004}_{-0.003}$	$0.701^{+0.002}_{-0.002}$
0.8	Low	$0.75^{+0.08}_{-0.09}$	$0.78^{+0.06}_{-0.07}$	$0.71^{+0.06}_{-0.06}$
	Med	$0.79^{+0.03}_{-0.03}$	$0.80^{+0.02}_{-0.02}$	$0.81^{+0.01}_{-0.01}$
	High	$0.800^{+0.007}_{-0.009}$	$0.800^{+0.003}_{-0.003}$	$0.798^{+0.002}_{-0.002}$
0.9	Low	$0.86^{+0.06}_{-0.06}$	$0.88^{+0.06}_{-0.06}$	$0.90^{+0.04}_{-0.04}$
	Med	$0.90^{+0.03}_{-0.04}$	$0.90^{+0.02}_{-0.02}$	$0.90^{+0.01}_{-0.01}$
	High	$0.90^{+0.01}_{-0.01}$	$0.901^{+0.006}_{-0.006}$	$0.898^{+0.005}_{-0.005}$

λ_s true	SNR	3 detectors	4 detectors	5 detectors
1.0	Low	$0.95^{+0.04}_{-0.09}$	$0.95^{+0.04}_{-0.06}$	$0.97^{+0.02}_{-0.03}$
	Med	$0.99^{+0.009}_{-0.02}$	$0.99^{+0.007}_{-0.01}$	$0.995^{+0.004}_{-0.007}$
	High	$0.99^{+0.004}_{-0.01}$	$0.997^{+0.002}_{-0.004}$	$0.997^{+0.002}_{-0.003}$

Table A.4: Table of λ_s median and errors corresponding to a 90% credible interval for the posterior probability distributions in Figures 3.5, 3.6, 3.7 and Histograms in Figure A.2.

λ_s true	SNR	3 detectors	4 detectors	5 detectors
0.0	Low	0.1	0.05	0.03
	Med	0.03	0.02	0.012
	High	0.006	0.003	0.002
1.0	Low	0.88	0.90	0.95
	Med	0.98	0.98	0.99
	High	0.987	0.994	0.995

Table A.5: Table of λ_s posterior 90% upper (row 1) and lower (row 2) limits (corresponding to true values $\lambda_s = 0.0$ and $\lambda_s = 1.0$ respectively) in Figures 3.5, 3.6, 3.7.

λ_v true	SNR	3 detectors	4 detectors	5 detectors
0.41	Low	$0.39^{+0.03}_{-0.06}$	$0.40^{+0.03}_{-0.03}$	$0.42^{+0.01}_{-0.01}$
0.06	Low	$0.06^{+0.04}_{-0.04}$	$0.05^{+0.05}_{-0.03}$	$0.07^{+0.02}_{-0.03}$
0.08	Low	$0.08^{+0.03}_{-0.03}$	$0.08^{+0.02}_{-0.02}$	$0.09^{+0.01}_{-0.01}$
0.08	Low	$0.07^{+0.05}_{-0.03}$	$0.08^{+0.03}_{-0.04}$	$0.09^{+0.02}_{-0.02}$
0.13	Low	$0.12^{+0.08}_{-0.06}$	$0.15^{+0.04}_{-0.09}$	$0.12^{+0.03}_{-0.04}$
0.2	Low	$0.20^{+0.04}_{-0.06}$	$0.20^{+0.03}_{-0.02}$	$0.19^{+0.02}_{-0.02}$
0.09	Low	$0.09^{+0.03}_{-0.05}$	$0.10^{+0.02}_{-0.03}$	$0.07^{+0.02}_{-0.02}$
0.01	Low	$0.03^{+0.05}_{-0.03}$	$0.02^{+0.04}_{-0.02}$	$0.04^{+0.03}_{-0.03}$
0.1	Low	$0.11^{+0.03}_{-0.03}$	$0.10^{+0.02}_{-0.03}$	$0.12^{+0.02}_{-0.02}$
0.0	Low	$0.02^{+0.04}_{-0.02}$	$0.02^{+0.03}_{-0.02}$	$0.02^{+0.02}_{-0.02}$
0.0	Low	$0.01^{+0.04}_{-0.01}$	$0.01^{+0.03}_{-0.01}$	$0.01^{+0.01}_{-0.008}$

λ_ν true	SNR	3 detectors	4 detectors	5 detectors
0.09	Med	$0.09^{+0.01}_{-0.01}$	$0.09^{+0.009}_{-0.01}$	$0.095^{+0.005}_{-0.005}$
0.08	Med	$0.08^{+0.02}_{-0.01}$	$0.081^{+0.009}_{-0.007}$	$0.078^{+0.005}_{-0.005}$
0.04	Med	$0.04^{+0.01}_{-0.02}$	$0.041^{+0.008}_{-0.009}$	$0.038^{+0.005}_{-0.005}$
0.06	Med	$0.06^{+0.01}_{-0.02}$	$0.06^{+0.01}_{-0.02}$	$0.059^{+0.006}_{-0.006}$
0.22	Med	$0.22^{+0.03}_{-0.01}$	$0.218^{+0.005}_{-0.007}$	$0.219^{+0.003}_{-0.003}$
0.21	Med	$0.21^{+0.02}_{-0.03}$	$0.21^{+0.03}_{-0.01}$	$0.206^{+0.008}_{-0.008}$
0.14	Med	$0.14^{+0.02}_{-0.02}$	$0.14^{+0.009}_{-0.02}$	$0.136^{+0.006}_{-0.006}$
0.14	Med	$0.14^{+0.01}_{-0.02}$	$0.139^{+0.007}_{-0.008}$	$0.140^{+0.005}_{-0.005}$
0.03	Med	$0.03^{+0.01}_{-0.01}$	$0.03^{+0.01}_{-0.01}$	$0.026^{+0.006}_{-0.006}$
0.04	Med	$0.04^{+0.01}_{-0.02}$	$0.041^{+0.008}_{-0.008}$	$0.038^{+0.006}_{-0.007}$
0.0	Med	$0.003^{+0.007}_{-0.002}$	$0.002^{+0.005}_{-0.002}$	$0.001^{+0.002}_{-0.001}$
0.09	High	$0.090^{+0.003}_{-0.002}$	$0.090^{+0.002}_{-0.001}$	$0.090^{+0.001}_{-0.001}$
0.22	High	$0.220^{+0.004}_{-0.003}$	$0.220^{+0.003}_{-0.003}$	$0.220^{+0.002}_{-0.002}$
0.08	High	$0.080^{+0.005}_{-0.005}$	$0.080^{+0.004}_{-0.004}$	$0.079^{+0.002}_{-0.002}$
0.19	High	$0.190^{+0.003}_{-0.002}$	$0.190^{+0.002}_{-0.002}$	$0.190^{+0.001}_{-0.001}$
0.2	High	$0.200^{+0.003}_{-0.002}$	$0.200^{+0.003}_{-0.002}$	$0.199^{+0.001}_{-0.001}$
0.01	High	$0.010^{+0.002}_{-0.004}$	$0.010^{+0.002}_{-0.002}$	$0.011^{+0.001}_{-0.001}$
0.09	High	$0.090^{+0.003}_{-0.003}$	$0.090^{+0.002}_{-0.001}$	$0.0895^{+0.0009}_{-0.0009}$
0.08	High	$0.080^{+0.004}_{-0.003}$	$0.080^{+0.003}_{-0.003}$	$0.081^{+0.002}_{-0.002}$
0.01	High	$0.011^{+0.004}_{-0.004}$	$0.009^{+0.002}_{-0.002}$	$0.010^{+0.001}_{-0.001}$
0.03	High	$0.030^{+0.002}_{-0.002}$	$0.029^{+0.001}_{-0.001}$	$0.030^{+0.001}_{-0.001}$
0.0	High	$0.002^{+0.006}_{-0.001}$	$0.001^{+0.002}_{-0.0009}$	$0.001^{+0.001}_{-0.0006}$

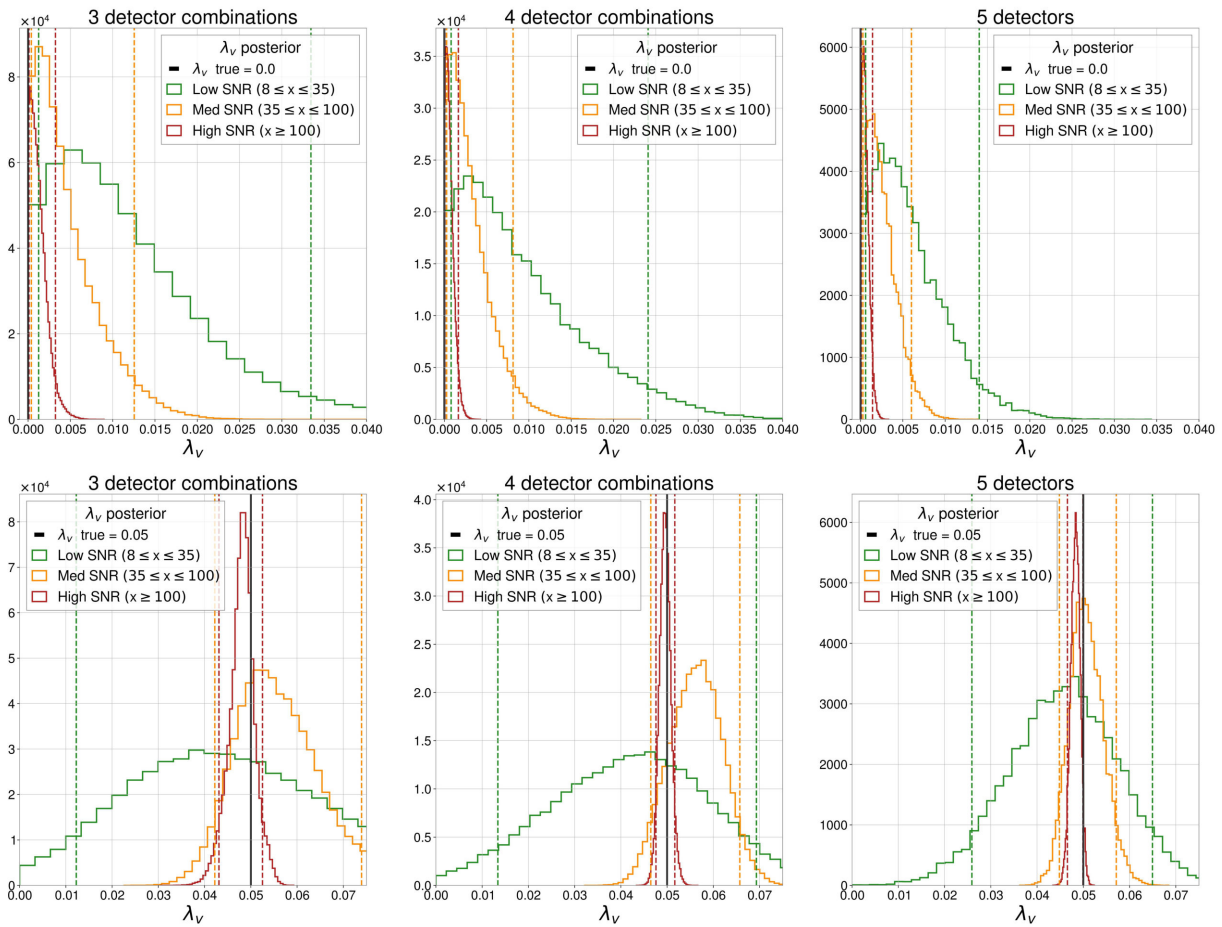
Table A.6: Table of λ_ν median and errors corresponding to a 90% credible interval for the posterior probability distributions in Figures 3.5, 3.6, 3.7 and Histograms in Figure A.2.

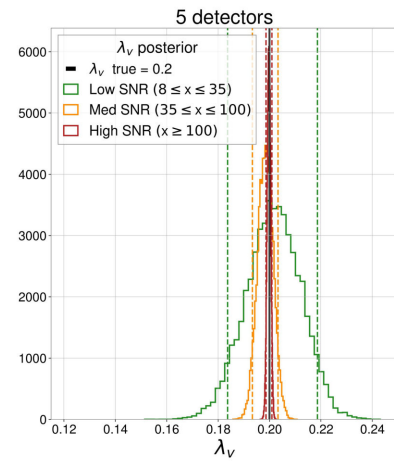
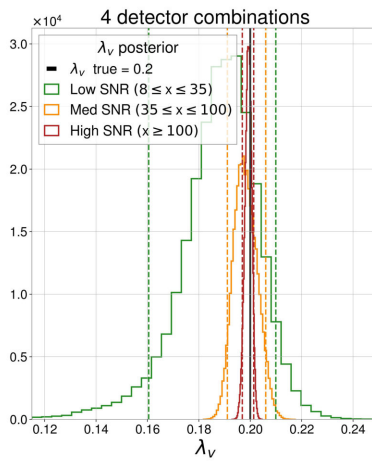
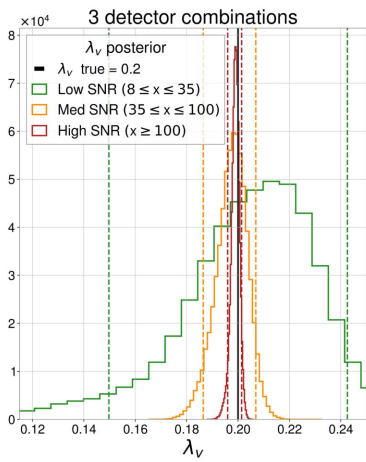
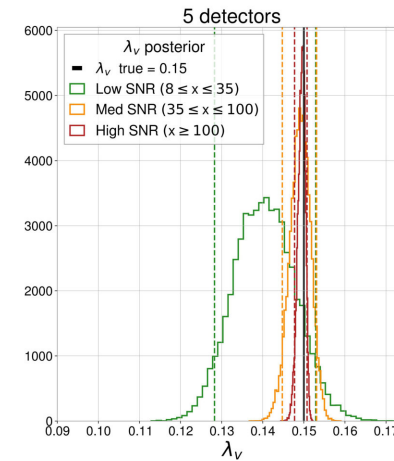
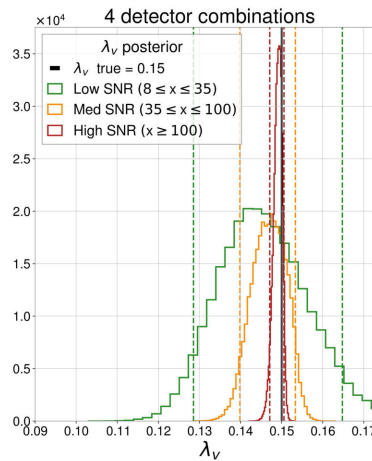
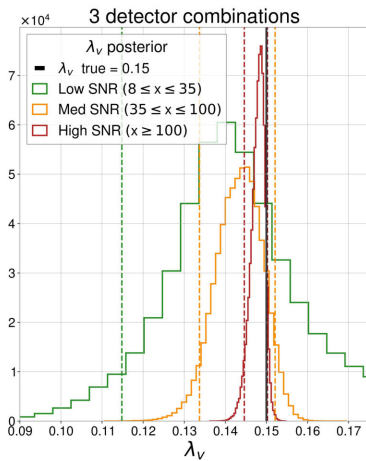
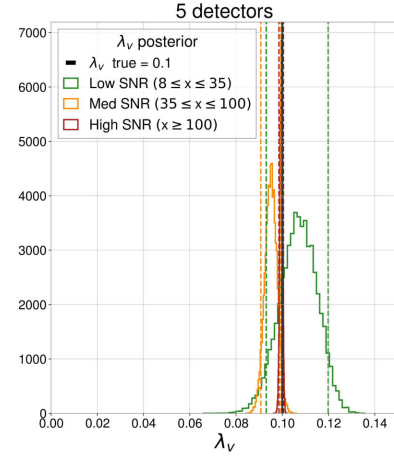
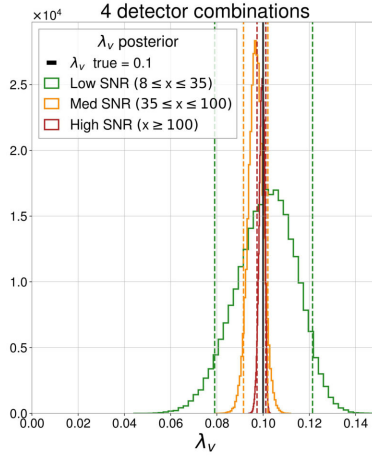
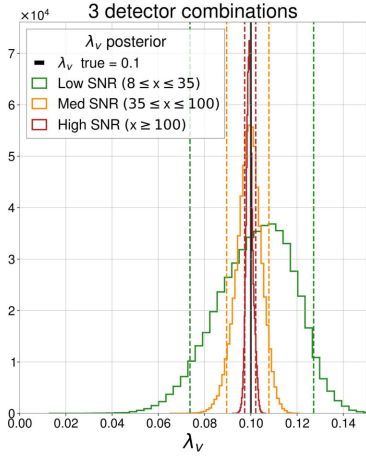
A.2 Tensor-Vector (tv) polarized GWs

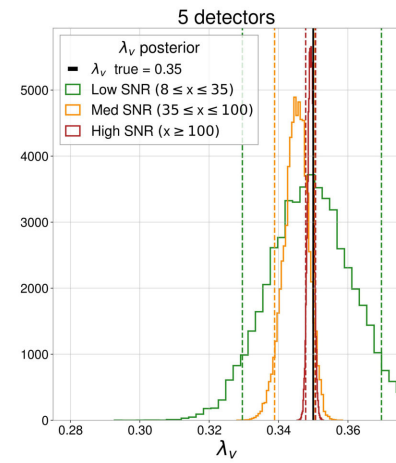
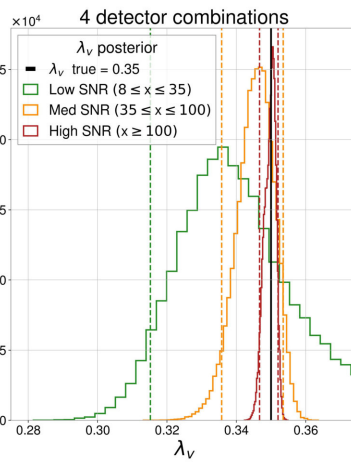
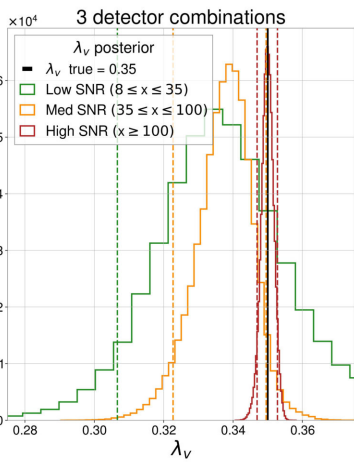
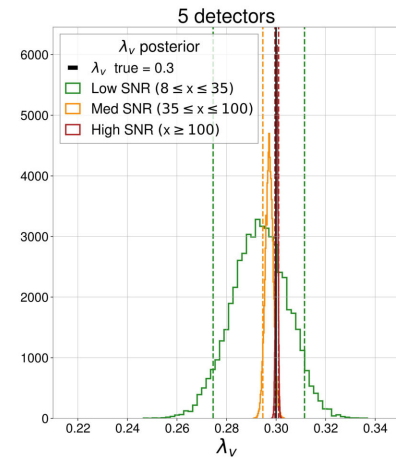
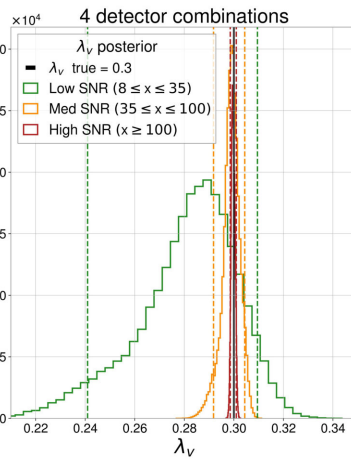
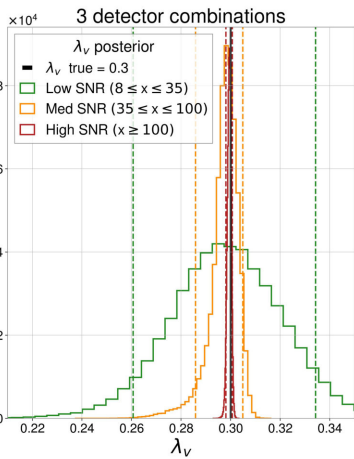
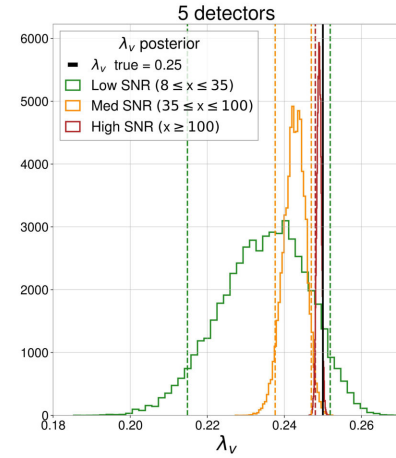
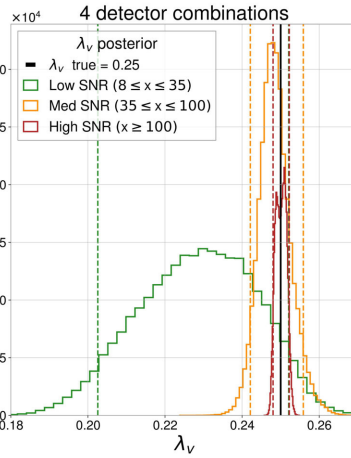
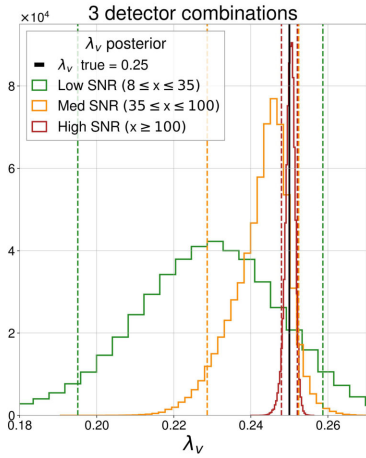
λ_v posterior for tv polarized GWs; fixed ψ prior

In the following Figure A.3, we plot histograms of λ_v posterior probability distributions for tv polarized GWs. The rows step through 11 progressively increasing values of $\lambda_v \in [0, 0.5]$. All the remaining polarization content is tensorial (i.e. $\lambda_s = 0$).

The 90% credible intervals for the λ_v and λ_s posterior probability distributions are given in Tables A.7 and A.9 respectively. Moreover, the 90% upper and lower limits for the λ_v posterior probability distributions (corresponding to true values $\lambda_v = 0.0$ and $\lambda_v = 0.5$ respectively) are given in Table A.8.







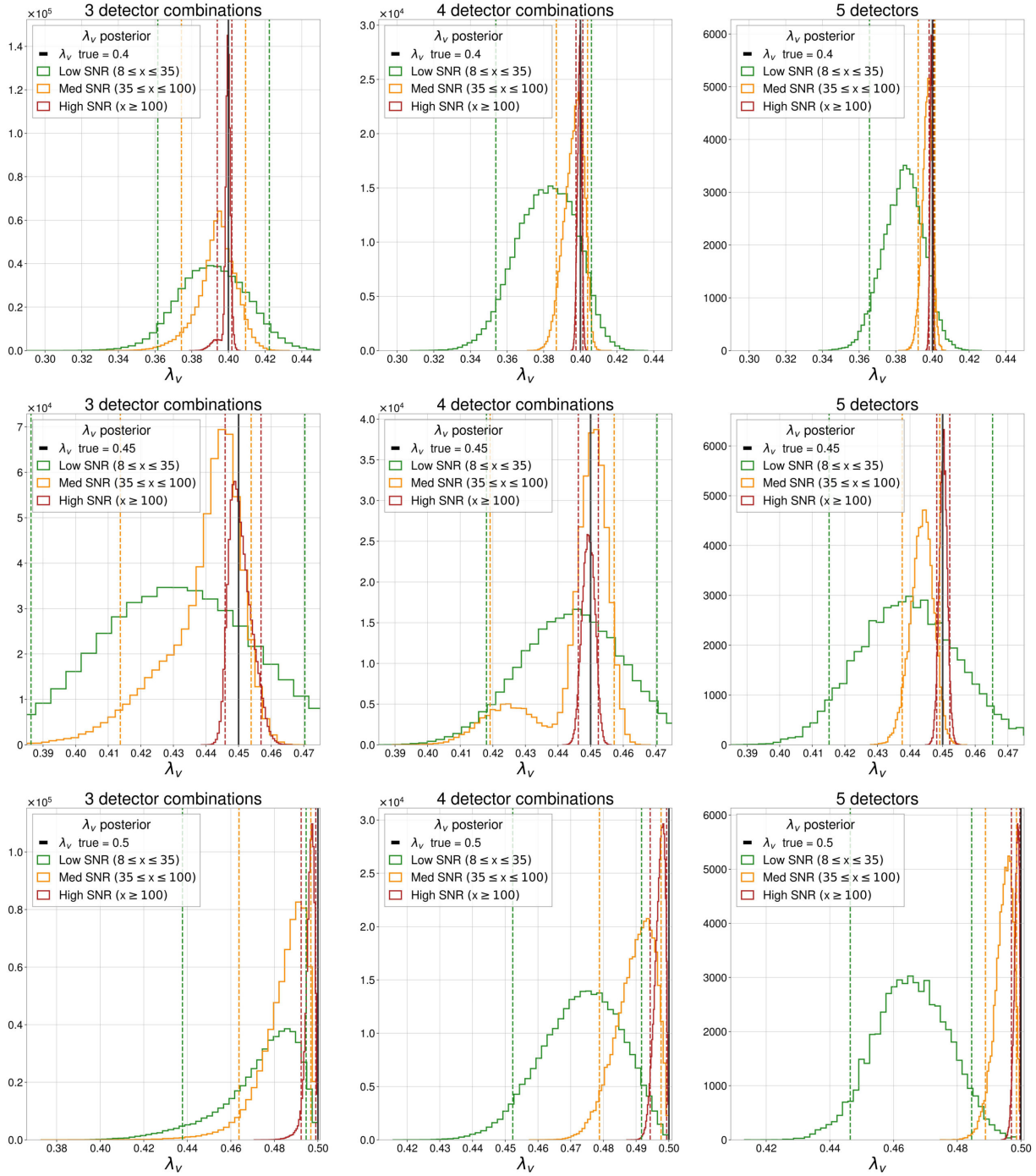


Figure A.3: Histograms of λ_v posteriors for tv polarized GWs averaged over all possible three (left), four (middle) and five (right) detector combinations for low, medium and high SNRs (corresponding to Figures 3.8, 3.9 and 3.10 respectively). The rows step through 11 progressively increasing values of $\lambda_v \in [0, 0.5]$. All the remaining polarization content is tensorial (i.e. $\lambda_s = 0$). Each histogram corresponds to an injection with a randomly chosen sky location and polarization angle (ψ).

λ_v true	SNR	3 detectors	4 detectors	5 detectors
0.0	Low	$0.01^{+0.02}_{-0.009}$	$0.01^{+0.02}_{-0.007}$	$0.005^{+0.009}_{-0.004}$
	Med	$0.004^{+0.009}_{-0.003}$	$0.003^{+0.006}_{-0.002}$	$0.002^{+0.004}_{-0.002}$
	High	$0.001^{+0.002}_{-0.001}$	$0.001^{+0.001}_{-0.0005}$	$0.0005^{+0.0009}_{-0.0005}$
0.05	Low	$0.05^{+0.04}_{-0.03}$	$0.04^{+0.03}_{-0.03}$	$0.05^{+0.02}_{-0.02}$
	Med	$0.06^{+0.02}_{-0.01}$	$0.06^{+0.009}_{-0.01}$	$0.050^{+0.007}_{-0.006}$
	High	$0.048^{+0.004}_{-0.005}$	$0.050^{+0.002}_{-0.002}$	$0.048^{+0.002}_{-0.002}$
0.1	Low	$0.10^{+0.02}_{-0.03}$	$0.10^{+0.02}_{-0.02}$	$0.11^{+0.01}_{-0.01}$
	Med	$0.10^{+0.009}_{-0.01}$	$0.097^{+0.005}_{-0.005}$	$0.095^{+0.004}_{-0.004}$
	High	$0.099^{+0.003}_{-0.002}$	$0.100^{+0.002}_{-0.002}$	$0.100^{+0.0009}_{-0.001}$
0.15	Low	$0.14^{+0.04}_{-0.03}$	$0.15^{+0.02}_{-0.02}$	$0.14^{+0.01}_{-0.01}$
	Med	$0.14^{+0.009}_{-0.01}$	$0.147^{+0.006}_{-0.007}$	$0.149^{+0.004}_{-0.004}$
	High	$0.148^{+0.002}_{-0.003}$	$0.149^{+0.001}_{-0.002}$	$0.150^{+0.001}_{-0.002}$
0.2	Low	$0.21^{+0.04}_{-0.06}$	$0.19^{+0.02}_{-0.03}$	$0.20^{+0.02}_{-0.02}$
	Med	$0.20^{+0.009}_{-0.01}$	$0.198^{+0.008}_{-0.007}$	$0.198^{+0.005}_{-0.005}$
	High	$0.199^{+0.002}_{-0.003}$	$0.199^{+0.002}_{-0.002}$	$0.200^{+0.001}_{-0.001}$
0.25	Low	$0.23^{+0.03}_{-0.03}$	$0.23^{+0.02}_{-0.03}$	$0.24^{+0.02}_{-0.02}$
	Med	$0.24^{+0.009}_{-0.02}$	$0.248^{+0.008}_{-0.006}$	$0.243^{+0.004}_{-0.005}$
	High	$0.250^{+0.002}_{-0.002}$	$0.250^{+0.002}_{-0.002}$	$0.249^{+0.001}_{-0.001}$
0.3	Low	$0.30^{+0.04}_{-0.04}$	$0.28^{+0.03}_{-0.04}$	$0.29^{+0.02}_{-0.02}$
	Med	$0.30^{+0.007}_{-0.01}$	$0.299^{+0.005}_{-0.007}$	$0.297^{+0.003}_{-0.003}$
	High	$0.299^{+0.001}_{-0.001}$	$0.300^{+0.001}_{-0.001}$	$0.3003^{+0.0007}_{-0.0008}$
0.35	Low	$0.34^{+0.06}_{-0.03}$	$0.34^{+0.04}_{-0.02}$	$0.35^{+0.02}_{-0.02}$
	Med	$0.34^{+0.01}_{-0.02}$	$0.35^{+0.008}_{-0.01}$	$0.345^{+0.005}_{-0.006}$
	High	$0.350^{+0.003}_{-0.003}$	$0.350^{+0.002}_{-0.003}$	$0.349^{+0.001}_{-0.001}$
0.4	Low	$0.39^{+0.03}_{-0.03}$	$0.38^{+0.02}_{-0.03}$	$0.38^{+0.02}_{-0.02}$
	Med	$0.39^{+0.01}_{-0.02}$	$0.40^{+0.007}_{-0.01}$	$0.397^{+0.004}_{-0.005}$
	High	$0.400^{+0.002}_{-0.006}$	$0.400^{+0.002}_{-0.002}$	$0.399^{+0.001}_{-0.001}$
0.45	Low	$0.43^{+0.04}_{-0.04}$	$0.44^{+0.03}_{-0.03}$	$0.44^{+0.03}_{-0.02}$
	Med	$0.44^{+0.01}_{-0.03}$	$0.45^{+0.008}_{-0.03}$	$0.444^{+0.005}_{-0.006}$
	High	$0.450^{+0.007}_{-0.004}$	$0.449^{+0.003}_{-0.003}$	$0.450^{+0.002}_{-0.002}$

λ_v true	SNR	3 detectors	4 detectors	5 detectors
0.5	Low	$0.48^{+0.02}_{-0.04}$	$0.47^{+0.02}_{-0.02}$	$0.47^{+0.02}_{-0.02}$
	Med	$0.49^{+0.01}_{-0.02}$	$0.49^{+0.007}_{-0.01}$	$0.495^{+0.004}_{-0.006}$
	High	$0.497^{+0.002}_{-0.004}$	$0.497^{+0.002}_{-0.003}$	$0.499^{+0.001}_{-0.002}$

Table A.7: Table of λ_v median and errors corresponding to a 90% credible interval for the posterior probability distributions in Figures 3.8, 3.9, 3.10 and Histograms in Figure A.3.

λ_v true	SNR	3 detectors	4 detectors	5 detectors
0.0	Low	0.03	0.02	0.012
	Med	0.011	0.007	0.005
	High	0.003	0.0014	0.0012
0.5	Low	0.45	0.45	0.45
	Med	0.47	0.481	0.49
	High	0.494	0.495	0.498

Table A.8: Table of λ_v posterior 90% upper (row 1) and lower (row 2) limits (corresponding to true values $\lambda_v = 0.0$ and $\lambda_v = 0.5$ respectively) in Figures 3.8, 3.9, 3.10.

λ_s true	SNR	3 detectors	4 detectors	5 detectors
0.0	Low	$0.02^{+0.05}_{-0.02}$	$0.02^{+0.03}_{-0.02}$	$0.02^{+0.03}_{-0.02}$
0.0	Low	$0.02^{+0.05}_{-0.02}$	$0.03^{+0.04}_{-0.02}$	$0.04^{+0.03}_{-0.03}$
0.0	Low	$0.03^{+0.09}_{-0.02}$	$0.02^{+0.04}_{-0.02}$	$0.02^{+0.03}_{-0.02}$
0.0	Low	$0.04^{+0.06}_{-0.03}$	$0.02^{+0.05}_{-0.02}$	$0.02^{+0.03}_{-0.02}$
0.0	Low	$0.02^{+0.08}_{-0.02}$	$0.01^{+0.05}_{-0.01}$	$0.02^{+0.02}_{-0.01}$
0.0	Low	$0.05^{+0.08}_{-0.05}$	$0.05^{+0.08}_{-0.05}$	$0.05^{+0.06}_{-0.04}$
0.0	Low	$0.03^{+0.07}_{-0.02}$	$0.02^{+0.08}_{-0.02}$	$0.03^{+0.03}_{-0.02}$
0.0	Low	$0.02^{+0.03}_{-0.02}$	$0.02^{+0.03}_{-0.02}$	$0.03^{+0.03}_{-0.02}$
0.0	Low	$0.0^{+0.1}_{-0.04}$	$0.04^{+0.08}_{-0.04}$	$0.03^{+0.05}_{-0.03}$
0.0	Low	$0.02^{+0.04}_{-0.02}$	$0.01^{+0.03}_{-0.009}$	$0.02^{+0.02}_{-0.02}$
0.0	Low	$0.02^{+0.07}_{-0.02}$	$0.03^{+0.04}_{-0.02}$	$0.04^{+0.03}_{-0.03}$

λ_s true	SNR	3 detectors	4 detectors	5 detectors
0.0	Med	0.00 ^{+0.01} _{-0.004}	0.007 ^{+0.009} _{-0.006}	0.009 ^{+0.008} _{-0.007}
0.0	Med	0.01 ^{+0.03} _{-0.008}	0.01 ^{+0.02} _{-0.01}	0.01 ^{+0.01} _{-0.006}
0.0	Med	0.01 ^{+0.02} _{-0.01}	0.01 ^{+0.02} _{-0.007}	0.01 ^{+0.01} _{-0.009}
0.0	Med	0.01 ^{+0.03} _{-0.01}	0.01 ^{+0.02} _{-0.01}	0.01 ^{+0.01} _{-0.007}
0.0	Med	0.01 ^{+0.03} _{-0.009}	0.01 ^{+0.01} _{-0.007}	0.01 ^{+0.01} _{-0.008}
0.0	Med	0.01 ^{+0.05} _{-0.01}	0.01 ^{+0.02} _{-0.008}	0.01 ^{+0.01} _{-0.008}
0.0	Med	0.01 ^{+0.03} _{-0.007}	0.01 ^{+0.02} _{-0.005}	0.003 ^{+0.005} _{-0.002}
0.0	Med	0.02 ^{+0.04} _{-0.02}	0.01 ^{+0.02} _{-0.009}	0.01 ^{+0.01} _{-0.008}
0.0	Med	0.02 ^{+0.05} _{-0.01}	0.01 ^{+0.02} _{-0.01}	0.01 ^{+0.01} _{-0.005}
0.0	Med	0.02 ^{+0.05} _{-0.02}	0.01 ^{+0.03} _{-0.008}	0.01 ^{+0.01} _{-0.008}
0.0	Med	0.01 ^{+0.04} _{-0.01}	0.01 ^{+0.02} _{-0.01}	0.00 ^{+0.01} _{-0.004}
0.0	High	0.001 ^{+0.003} _{-0.001}	0.001 ^{+0.002} _{-0.001}	0.001 ^{+0.002} _{-0.0009}
0.0	High	0.001 ^{+0.009} _{-0.001}	0.001 ^{+0.002} _{-0.001}	0.002 ^{+0.002} _{-0.001}
0.0	High	0.003 ^{+0.007} _{-0.003}	0.003 ^{+0.008} _{-0.003}	0.002 ^{+0.004} _{-0.002}
0.0	High	0.01 ^{+0.01} _{-0.005}	0.003 ^{+0.006} _{-0.003}	0.005 ^{+0.006} _{-0.004}
0.0	High	0.00 ^{+0.02} _{-0.002}	0.002 ^{+0.005} _{-0.002}	0.001 ^{+0.001} _{-0.0006}
0.0	High	0.002 ^{+0.006} _{-0.002}	0.002 ^{+0.005} _{-0.002}	0.002 ^{+0.003} _{-0.002}
0.0	High	0.002 ^{+0.003} _{-0.002}	0.001 ^{+0.002} _{-0.0009}	0.001 ^{+0.002} _{-0.001}
0.0	High	0.001 ^{+0.003} _{-0.001}	0.001 ^{+0.002} _{-0.0007}	0.001 ^{+0.001} _{-0.0007}
0.0	High	0.00 ^{+0.01} _{-0.001}	0.001 ^{+0.002} _{-0.001}	0.001 ^{+0.002} _{-0.001}
0.0	High	0.002 ^{+0.003} _{-0.001}	0.001 ^{+0.003} _{-0.001}	0.001 ^{+0.001} _{-0.0006}
0.0	High	0.004 ^{+0.009} _{-0.003}	0.003 ^{+0.005} _{-0.002}	0.001 ^{+0.002} _{-0.0007}

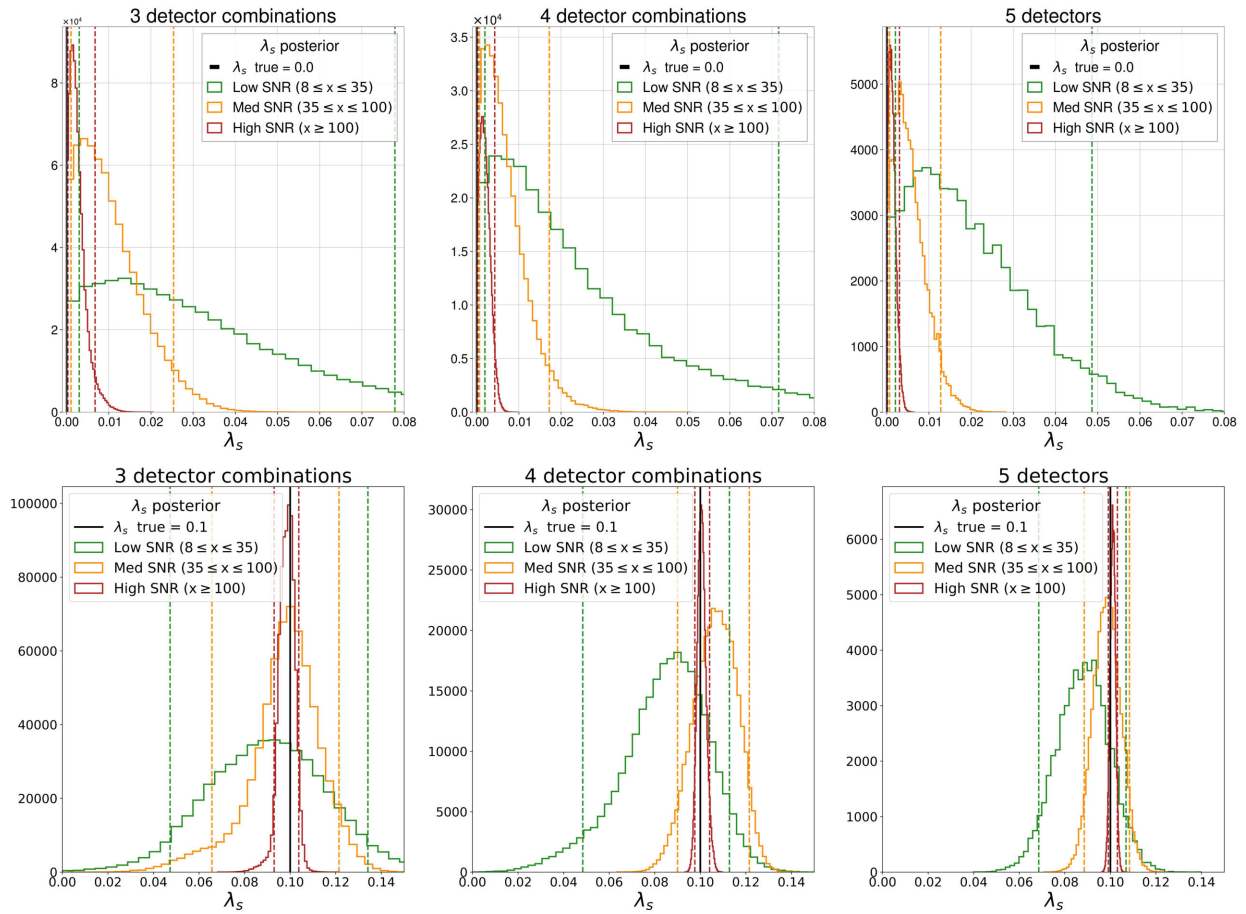
Table A.9: Table of λ_s median and errors corresponding to a 90% credible interval for the posterior probability distributions in Figures 3.8, 3.9, 3.10 and Histograms in Figure A.3.

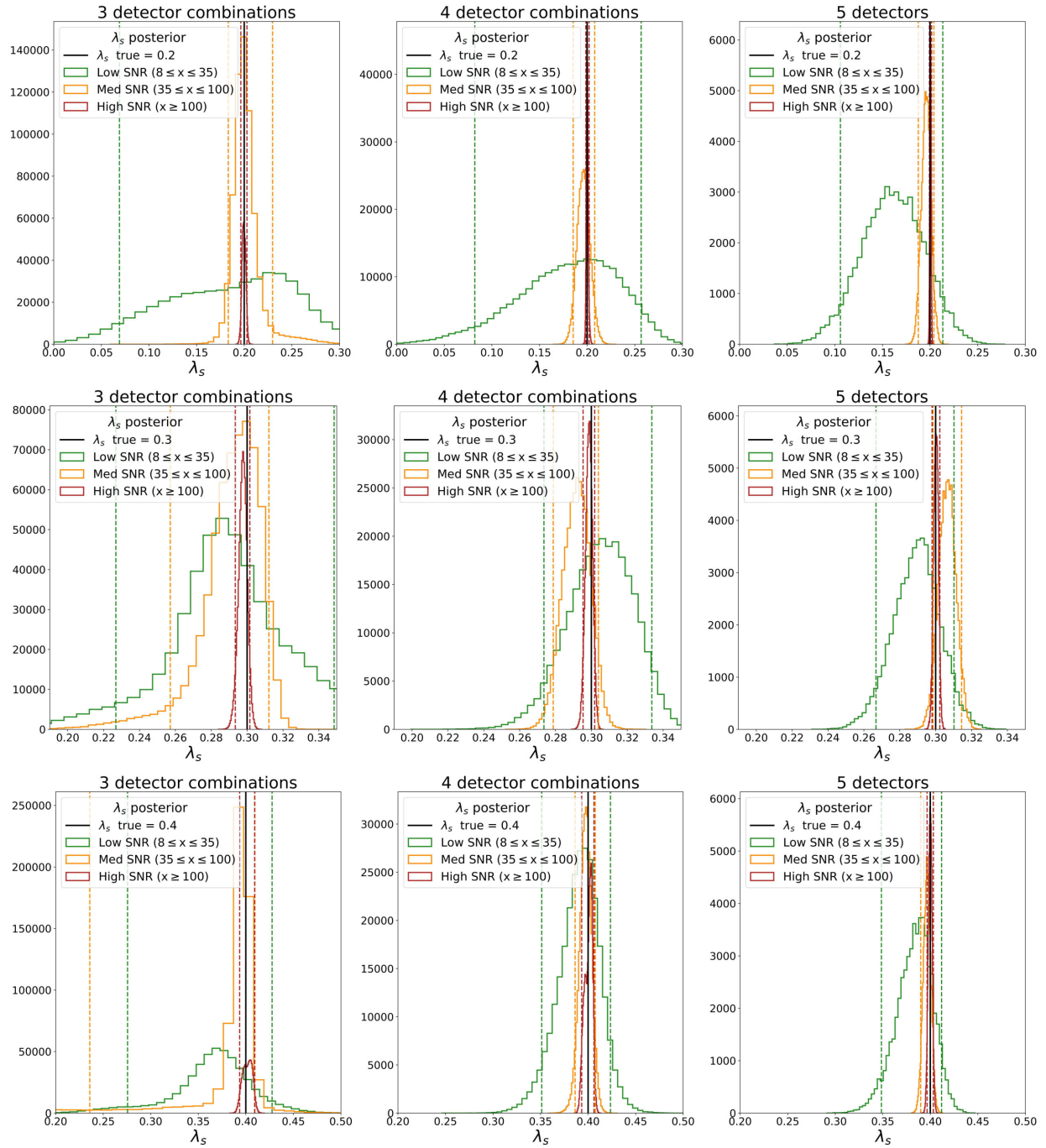
A.3 Tensor-Scalar (ts) polarized GWs

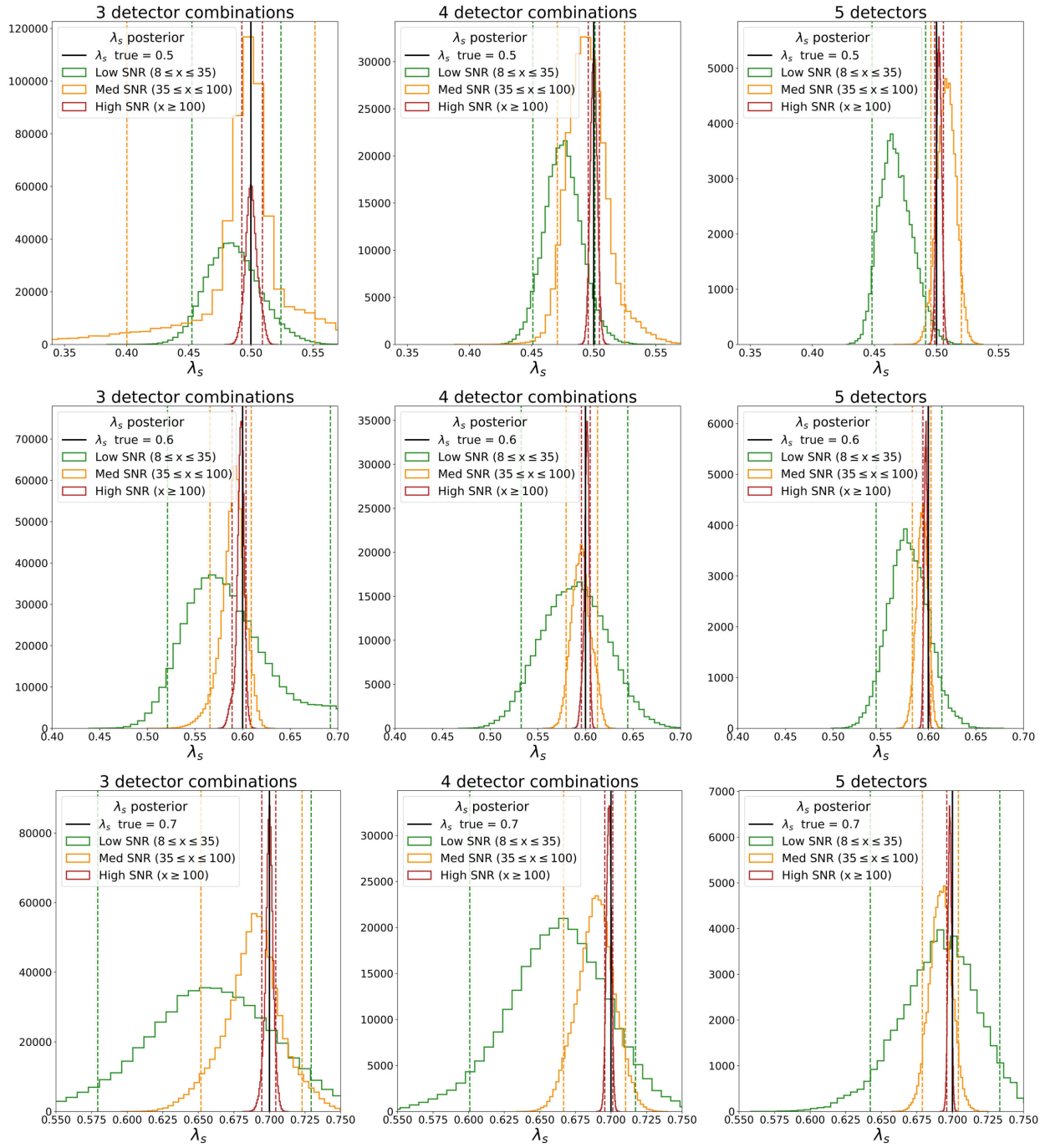
λ_s posterior for ts polarized GWs; fixed ψ prior

In the following Figure A.4, we plot histograms of λ_s posterior probability distributions for ts polarized GWs. The rows step through 11 progressively increasing values of $\lambda_s \in [0, 1]$. All the remaining polarization content is tensorial (i.e. $\lambda_v = 0$).

The 90% credible intervals for the λ_s and λ_v posterior probability distributions are given in Tables A.10 and A.12 respectively. Moreover, the 90% upper and lower limits for the λ_s posterior probability distributions (corresponding to true values $\lambda_s = 0.0$ and $\lambda_s = 1.0$ respectively) are given in Table A.11.







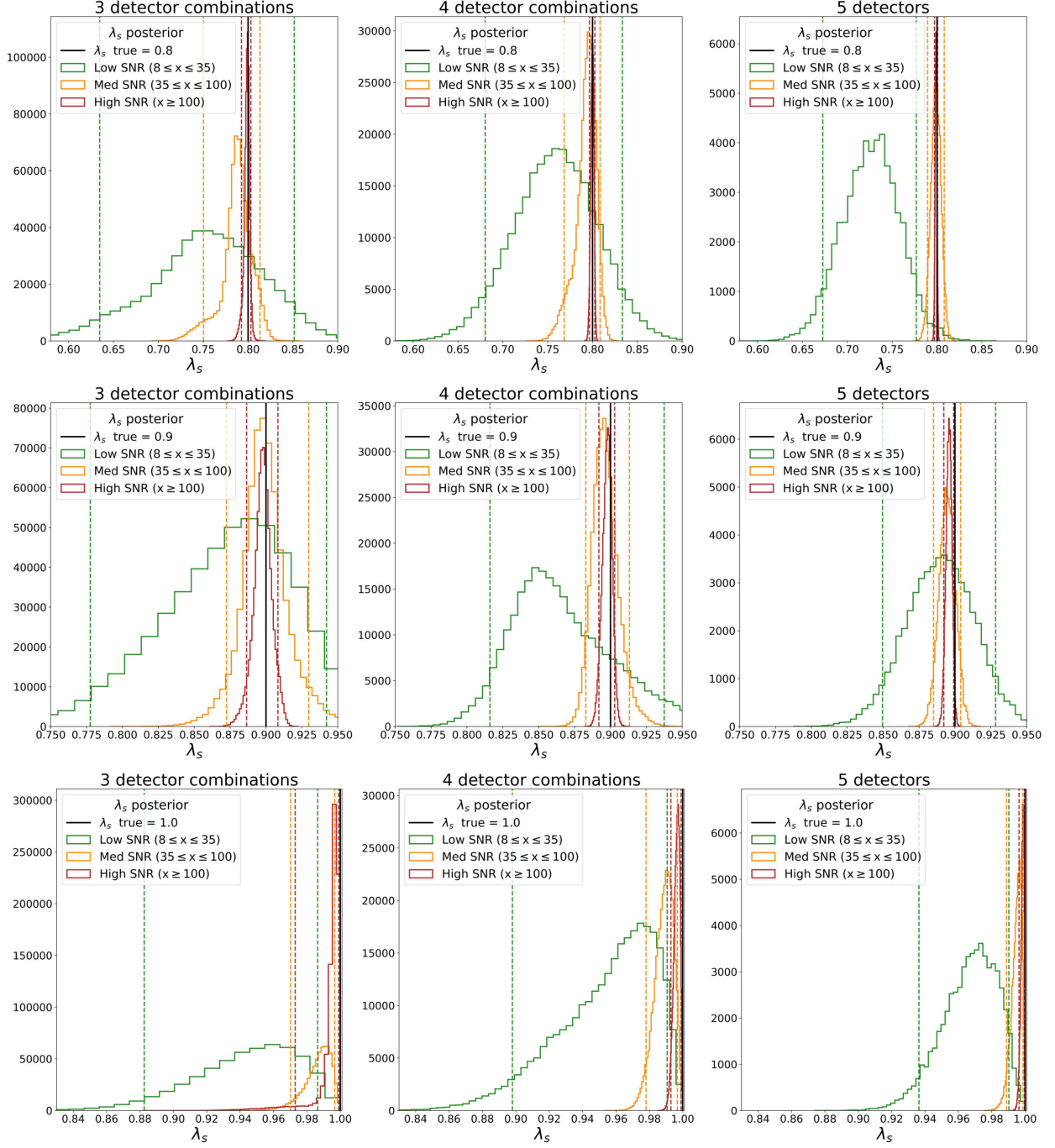


Figure A.4: Histograms of λ_s posteriors for ts polarized GWs averaged over three (left), four (middle) and five (right) detector combinations for low, medium and high SNRs (corresponding to Figures 3.11, 3.12 and 3.13 respectively). The rows step through 11 progressively increasing values of $\lambda_s \in [0, 1]$. All the remaining polarization content is tensorial (i.e., $\lambda_v = 0$). Each histogram corresponds to an injection with a randomly chosen sky location and polarization angle (ψ).

λ_s true	SNR	3 detectors	4 detectors	5 detectors
0.0	Low	$0.03^{+0.05}_{-0.02}$	$0.02^{+0.05}_{-0.02}$	$0.02^{+0.03}_{-0.02}$
	Med	$0.01^{+0.02}_{-0.008}$	$0.01^{+0.01}_{-0.005}$	$0.005^{+0.008}_{-0.004}$
	High	$0.002^{+0.005}_{-0.002}$	$0.002^{+0.002}_{-0.002}$	$0.001^{+0.002}_{-0.001}$
0.1	Low	$0.09^{+0.04}_{-0.04}$	$0.09^{+0.03}_{-0.04}$	$0.09^{+0.02}_{-0.02}$
	Med	$0.10^{+0.02}_{-0.03}$	$0.11^{+0.01}_{-0.02}$	$0.10^{+0.01}_{-0.01}$
	High	$0.099^{+0.005}_{-0.006}$	$0.101^{+0.004}_{-0.003}$	$0.101^{+0.002}_{-0.002}$
0.2	Low	$0.2^{+0.1}_{-0.1}$	$0.2^{+0.07}_{-0.1}$	$0.16^{+0.05}_{-0.06}$
	Med	$0.20^{+0.03}_{-0.02}$	$0.20^{+0.01}_{-0.01}$	$0.196^{+0.008}_{-0.008}$
	High	$0.200^{+0.003}_{-0.003}$	$0.200^{+0.002}_{-0.001}$	$0.200^{+0.001}_{-0.001}$
0.3	Low	$0.29^{+0.06}_{-0.06}$	$0.31^{+0.03}_{-0.03}$	$0.29^{+0.02}_{-0.02}$
	Med	$0.29^{+0.02}_{-0.04}$	$0.29^{+0.01}_{-0.01}$	$0.307^{+0.008}_{-0.008}$
	High	$0.298^{+0.004}_{-0.004}$	$0.299^{+0.003}_{-0.003}$	$0.300^{+0.002}_{-0.002}$
0.4	Low	$0.37^{+0.06}_{-0.09}$	$0.39^{+0.03}_{-0.04}$	$0.38^{+0.03}_{-0.04}$
	Med	$0.4^{+0.02}_{-0.2}$	$0.40^{+0.01}_{-0.01}$	$0.397^{+0.006}_{-0.007}$
	High	$0.402^{+0.007}_{-0.008}$	$0.401^{+0.005}_{-0.008}$	$0.400^{+0.003}_{-0.003}$
0.5	Low	$0.49^{+0.04}_{-0.03}$	$0.48^{+0.03}_{-0.02}$	$0.47^{+0.02}_{-0.02}$
	Med	$0.5^{+0.05}_{-0.1}$	$0.49^{+0.03}_{-0.02}$	$0.51^{+0.01}_{-0.01}$
	High	$0.500^{+0.009}_{-0.008}$	$0.500^{+0.005}_{-0.004}$	$0.502^{+0.003}_{-0.004}$
0.6	Low	$0.6^{+0.1}_{-0.06}$	$0.59^{+0.06}_{-0.06}$	$0.58^{+0.04}_{-0.03}$
	Med	$0.59^{+0.02}_{-0.03}$	$0.60^{+0.02}_{-0.02}$	$0.59^{+0.009}_{-0.01}$
	High	$0.598^{+0.006}_{-0.009}$	$0.601^{+0.004}_{-0.006}$	$0.597^{+0.003}_{-0.003}$
0.7	Low	$0.66^{+0.07}_{-0.08}$	$0.66^{+0.05}_{-0.06}$	$0.69^{+0.04}_{-0.05}$
	Med	$0.69^{+0.03}_{-0.04}$	$0.69^{+0.02}_{-0.02}$	$0.69^{+0.01}_{-0.01}$
	High	$0.700^{+0.005}_{-0.005}$	$0.699^{+0.003}_{-0.003}$	$0.698^{+0.002}_{-0.002}$
0.8	Low	$0.8^{+0.1}_{-0.1}$	$0.76^{+0.07}_{-0.08}$	$0.73^{+0.05}_{-0.05}$
	Med	$0.79^{+0.02}_{-0.04}$	$0.79^{+0.01}_{-0.03}$	$0.799^{+0.009}_{-0.009}$
	High	$0.799^{+0.004}_{-0.006}$	$0.800^{+0.003}_{-0.003}$	$0.799^{+0.002}_{-0.002}$
0.9	Low	$0.9^{+0.07}_{-0.1}$	$0.86^{+0.08}_{-0.05}$	$0.89^{+0.04}_{-0.04}$
	Med	$0.90^{+0.03}_{-0.03}$	$0.90^{+0.02}_{-0.01}$	$0.89^{+0.009}_{-0.01}$
	High	$0.90^{+0.01}_{-0.01}$	$0.898^{+0.005}_{-0.006}$	$0.896^{+0.003}_{-0.004}$

λ_s true	SNR	3 detectors	4 detectors	5 detectors
1.0	Low	$0.95^{+0.04}_{-0.06}$	$0.96^{+0.03}_{-0.06}$	$0.97^{+0.02}_{-0.03}$
	Med	$0.99^{+0.009}_{-0.02}$	$0.99^{+0.007}_{-0.01}$	$0.995^{+0.003}_{-0.006}$
	High	$1.00^{+0.003}_{-0.02}$	$0.997^{+0.002}_{-0.004}$	$0.998^{+0.001}_{-0.002}$

Table A.10: Table of λ_s median and errors corresponding to a 90% credible interval for the posterior probability distributions in Figures 3.11, 3.12, 3.13 and Histograms in Figure A.4

λ_s true	SNR	3 detectors	4 detectors	5 detectors
0.0	Low	0.07	0.06	0.04
	Med	0.02	0.014	0.011
	High	0.005	0.004	0.002
1.0	Low	0.90	0.91	0.95
	Med	0.98	0.98	0.99
	High	0.988	0.994	0.996

Table A.11: Table of λ_s posterior 90% upper (row 1) and lower (row 2) limits (corresponding to true values $\lambda_s = 0.0$ and $\lambda_s = 1.0$ respectively) in Figures 3.11, 3.12, 3.13.

λ_v true	SNR	3 detectors	4 detectors	5 detectors
0.0	Low	$0.01^{+0.03}_{-0.01}$	$0.01^{+0.03}_{-0.01}$	$0.01^{+0.01}_{-0.007}$
0.0	Low	$0.02^{+0.03}_{-0.02}$	$0.02^{+0.02}_{-0.01}$	$0.01^{+0.02}_{-0.007}$
0.0	Low	$0.01^{+0.03}_{-0.009}$	$0.01^{+0.02}_{-0.007}$	$0.01^{+0.01}_{-0.006}$
0.0	Low	$0.02^{+0.03}_{-0.01}$	$0.01^{+0.02}_{-0.01}$	$0.01^{+0.02}_{-0.009}$
0.0	Low	$0.03^{+0.06}_{-0.02}$	$0.01^{+0.03}_{-0.01}$	$0.02^{+0.03}_{-0.02}$
0.0	Low	$0.02^{+0.04}_{-0.02}$	$0.01^{+0.03}_{-0.01}$	$0.03^{+0.02}_{-0.02}$
0.0	Low	$0.01^{+0.03}_{-0.01}$	$0.01^{+0.02}_{-0.008}$	$0.01^{+0.01}_{-0.008}$
0.0	Low	$0.02^{+0.05}_{-0.02}$	$0.02^{+0.05}_{-0.02}$	$0.02^{+0.03}_{-0.01}$
0.0	Low	$0.01^{+0.04}_{-0.01}$	$0.01^{+0.02}_{-0.01}$	$0.01^{+0.02}_{-0.008}$
0.0	Low	$0.02^{+0.04}_{-0.02}$	$0.01^{+0.02}_{-0.01}$	$0.02^{+0.02}_{-0.02}$
0.0	Low	$0.01^{+0.03}_{-0.01}$	$0.01^{+0.02}_{-0.01}$	$0.01^{+0.01}_{-0.006}$

λ_ν true	SNR	3 detectors	4 detectors	5 detectors
0.0	Med	0.00 ^{+0.01} _{-0.004}	0.003 ^{+0.006} _{-0.003}	0.001 ^{+0.003} _{-0.001}
0.0	Med	0.00 ^{+0.01} _{-0.004}	0.004 ^{+0.006} _{-0.003}	0.002 ^{+0.004} _{-0.002}
0.0	Med	0.003 ^{+0.008} _{-0.003}	0.004 ^{+0.005} _{-0.003}	0.002 ^{+0.004} _{-0.002}
0.0	Med	0.01 ^{+0.01} _{-0.005}	0.01 ^{+0.01} _{-0.006}	0.002 ^{+0.004} _{-0.001}
0.0	Med	0.01 ^{+0.01} _{-0.005}	0.004 ^{+0.007} _{-0.003}	0.002 ^{+0.004} _{-0.002}
0.0	Med	0.002 ^{+0.005} _{-0.002}	0.002 ^{+0.004} _{-0.001}	0.001 ^{+0.002} _{-0.001}
0.0	Med	0.00 ^{+0.01} _{-0.004}	0.004 ^{+0.008} _{-0.003}	0.006 ^{+0.006} _{-0.005}
0.0	Med	0.01 ^{+0.02} _{-0.006}	0.00 ^{+0.01} _{-0.004}	0.004 ^{+0.005} _{-0.004}
0.0	Med	0.01 ^{+0.01} _{-0.005}	0.004 ^{+0.009} _{-0.003}	0.002 ^{+0.004} _{-0.002}
0.0	Med	0.005 ^{+0.009} _{-0.004}	0.005 ^{+0.007} _{-0.004}	0.003 ^{+0.005} _{-0.003}
0.0	Med	0.002 ^{+0.006} _{-0.002}	0.003 ^{+0.004} _{-0.002}	0.001 ^{+0.002} _{-0.0007}
0.0	High	0.002 ^{+0.002} _{-0.001}	0.001 ^{+0.004} _{-0.0009}	0.001 ^{+0.001} _{-0.0006}
0.0	High	0.001 ^{+0.002} _{-0.0007}	0.001 ^{+0.001} _{-0.0006}	0.0003 ^{+0.0006} _{-0.0003}
0.0	High	0.002 ^{+0.004} _{-0.002}	0.001 ^{+0.003} _{-0.001}	0.001 ^{+0.002} _{-0.001}
0.0	High	0.001 ^{+0.002} _{-0.001}	0.001 ^{+0.002} _{-0.0008}	0.001 ^{+0.001} _{-0.0006}
0.0	High	0.001 ^{+0.001} _{-0.0007}	0.001 ^{+0.001} _{-0.0005}	0.0004 ^{+0.0008} _{-0.0004}
0.0	High	0.001 ^{+0.002} _{-0.001}	0.001 ^{+0.002} _{-0.0006}	0.001 ^{+0.001} _{-0.0005}
0.0	High	0.001 ^{+0.002} _{-0.0007}	0.001 ^{+0.001} _{-0.0004}	0.0005 ^{+0.0008} _{-0.0005}
0.0	High	0.001 ^{+0.003} _{-0.001}	0.001 ^{+0.002} _{-0.0009}	0.001 ^{+0.002} _{-0.0009}
0.0	High	0.001 ^{+0.003} _{-0.001}	0.001 ^{+0.002} _{-0.0009}	0.0005 ^{+0.0009} _{-0.0004}
0.0	High	0.001 ^{+0.002} _{-0.0007}	0.001 ^{+0.001} _{-0.0005}	0.0004 ^{+0.0007} _{-0.0003}
0.0	High	0.00 ^{+0.01} _{-0.001}	0.001 ^{+0.002} _{-0.0009}	0.000 ^{+0.001} _{-0.0004}

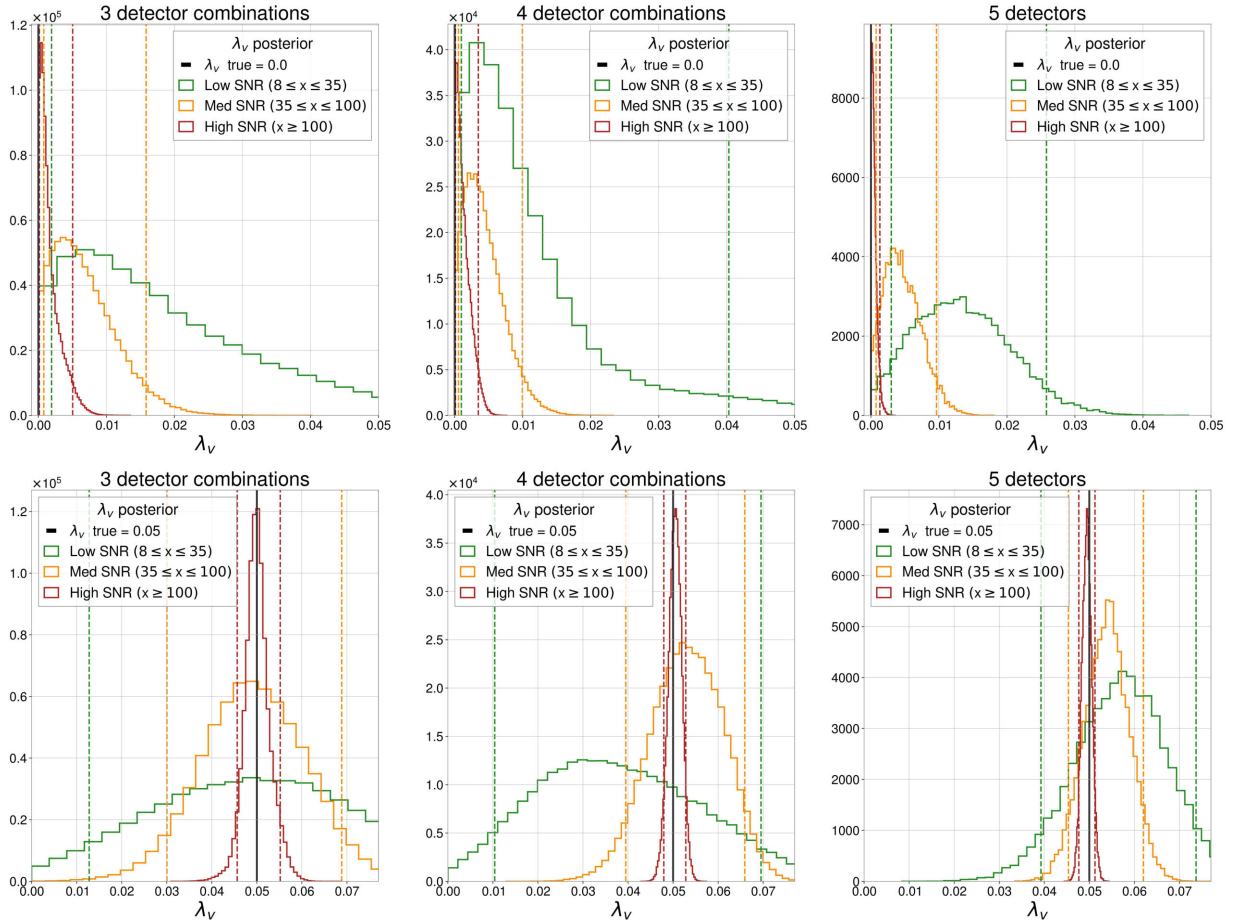
Table A.12: Table of λ_ν median and errors corresponding to a 90% credible interval for the posterior probability distributions in Figures 3.11, 3.12, 3.13 and Histograms in Figure A.4

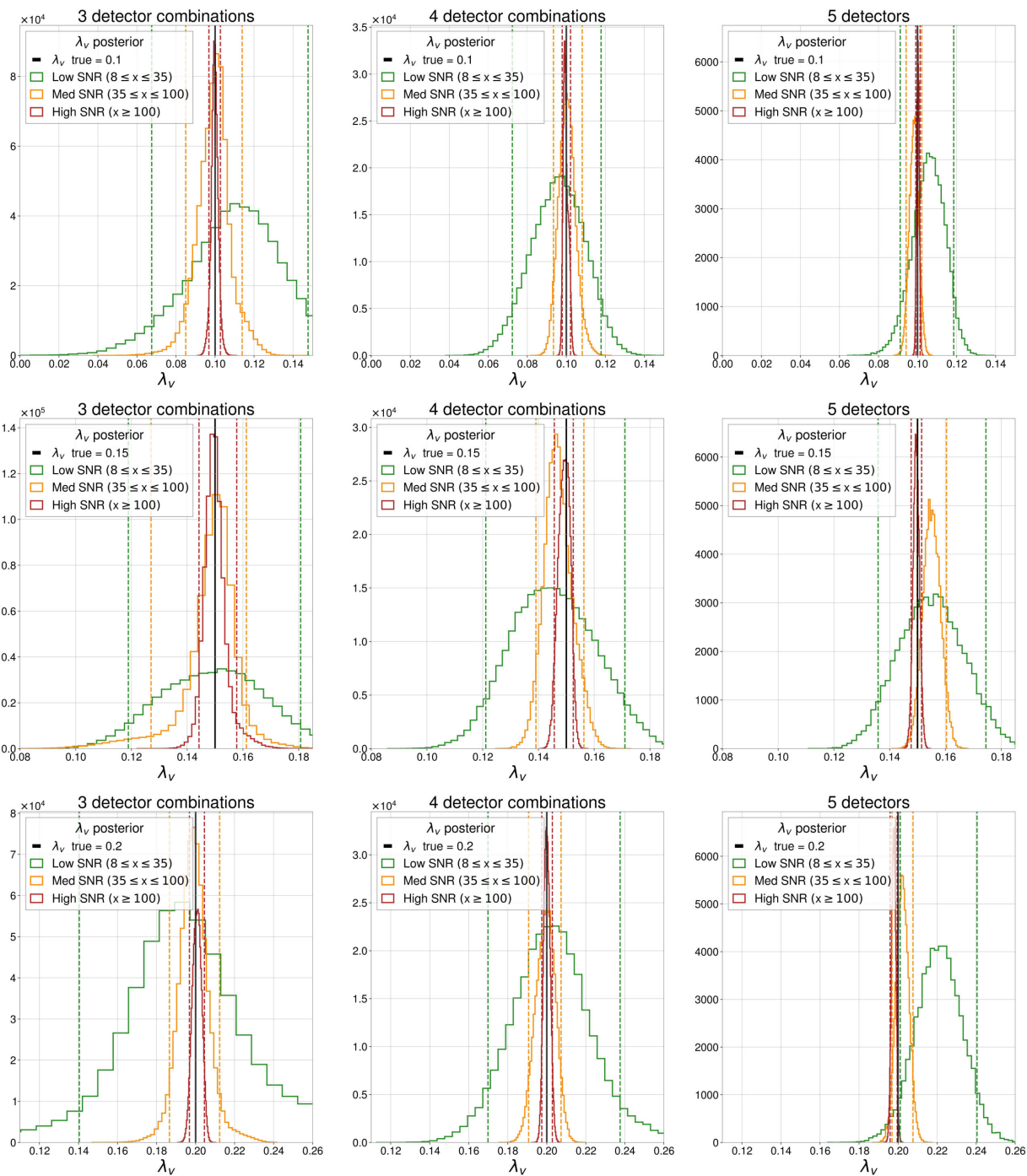
A.4 Tensor-Vector-Scalar (tvs) polarized GWs; uniform ψ prior

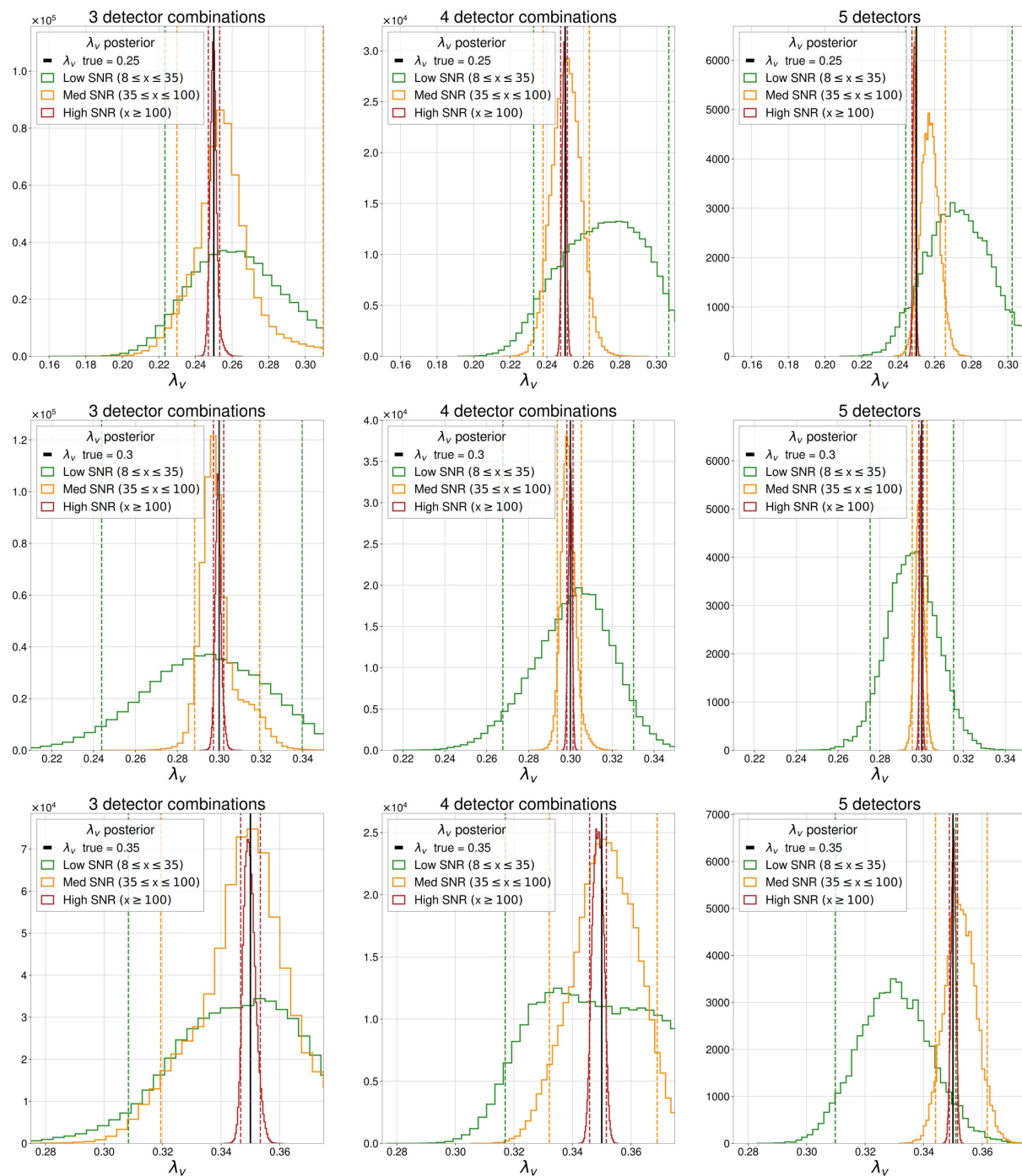
λ_v posterior for tvs polarized GWs; uniform ψ prior

In the following Figure A.5, we plot histograms of λ_v posterior probability distributions for tvs polarized GWs. The rows step through 11 progressively increasing values of $\lambda_v \in [0, 0.5]$. The remaining polarization content is randomly distributed between tensor (λ_t) and scalar (λ_s) components as per the constraint in Equation 2.9. The ψ prior distribution is uniform and periodic $\in [0, \pi]$ for the Bayesian parameter estimation.

The 90% credible intervals for the λ_v and λ_s posterior probability distributions are given in Tables A.13 and A.15 respectively. Moreover, the 90% upper and lower limits for the λ_v posterior probability distributions (corresponding to true values $\lambda_v = 0.0$ and $\lambda_v = 0.5$ respectively) are given in Table A.14.







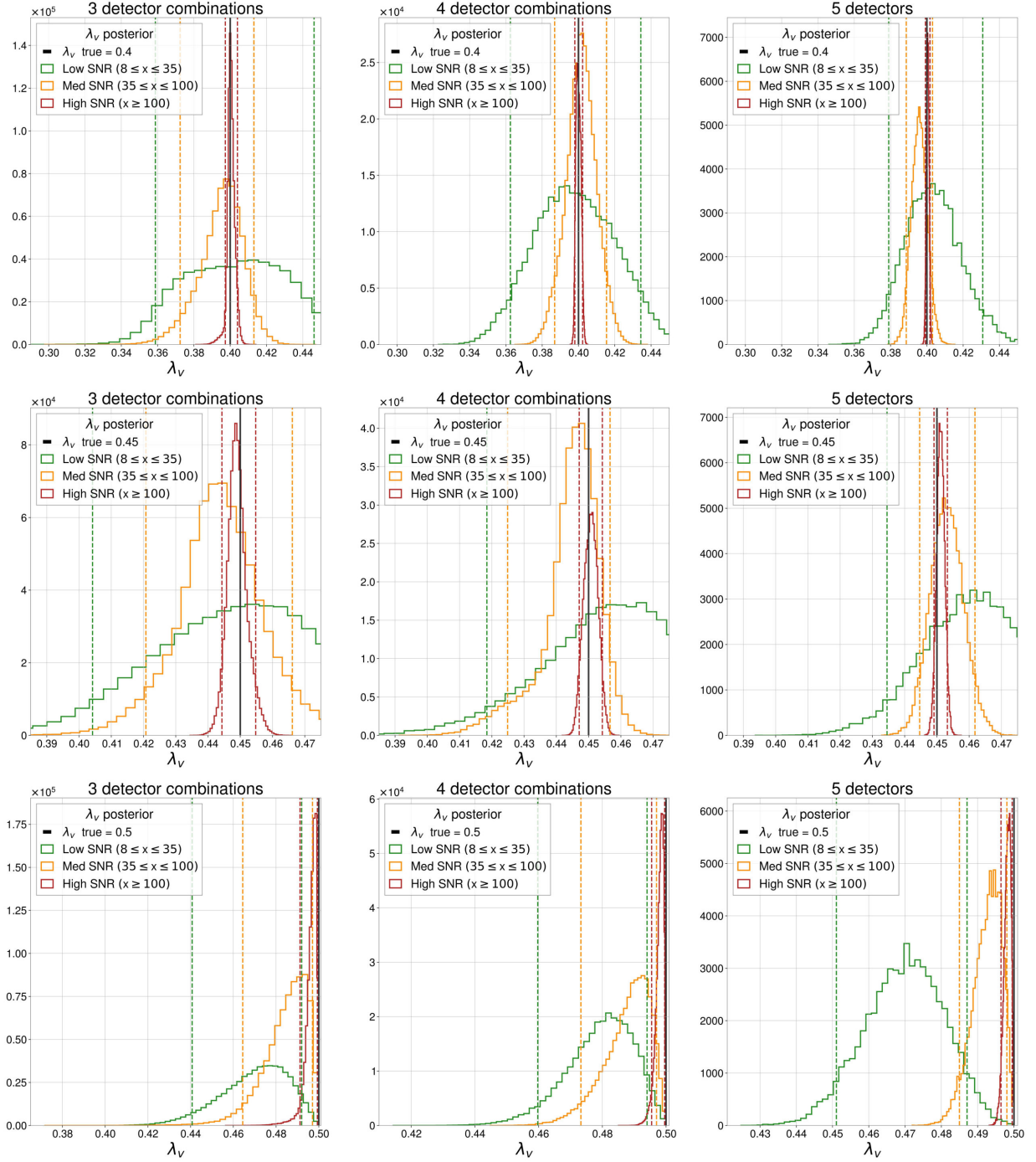


Figure A.5: Histograms of λ_v posteriors for tvs polarized GWs averaged over three (left), four (middle) and five (right) detector combinations for low, medium and high SNRs (corresponding to Figures 3.14, 3.15 and 3.16 respectively). The rows step through 11 progressively increasing values of $\lambda_v \in [0, 0.5]$. The remaining polarization content is randomly distributed between tensor (λ_t) and scalar (λ_s) components as per the constraint in Equation 2.9. Each histogram corresponds to an injection with a randomly chosen sky location and polarization angle (ψ). The ψ prior distribution is uniform and periodic $\in [0, \pi]$ for the Bayesian parameter estimation.

λ_v true	SNR	3 detectors	4 detectors	5 detectors
0.0	Low	$0.02^{+0.04}_{-0.01}$	$0.01^{+0.03}_{-0.007}$	$0.01^{+0.01}_{-0.01}$
	Med	$0.01^{+0.01}_{-0.005}$	$0.004^{+0.006}_{-0.003}$	$0.004^{+0.005}_{-0.004}$
	High	$0.001^{+0.004}_{-0.001}$	$0.001^{+0.002}_{-0.001}$	$0.0004^{+0.0009}_{-0.0004}$
0.05	Low	$0.05^{+0.03}_{-0.04}$	$0.04^{+0.03}_{-0.03}$	$0.06^{+0.02}_{-0.02}$
	Med	$0.05^{+0.02}_{-0.02}$	$0.05^{+0.01}_{-0.01}$	$0.054^{+0.008}_{-0.009}$
	High	$0.050^{+0.005}_{-0.004}$	$0.050^{+0.002}_{-0.003}$	$0.049^{+0.002}_{-0.002}$
0.1	Low	$0.11^{+0.04}_{-0.04}$	$0.10^{+0.02}_{-0.02}$	$0.11^{+0.01}_{-0.01}$
	Med	$0.10^{+0.01}_{-0.01}$	$0.100^{+0.008}_{-0.007}$	$0.098^{+0.004}_{-0.004}$
	High	$0.100^{+0.003}_{-0.003}$	$0.100^{+0.003}_{-0.002}$	$0.100^{+0.001}_{-0.001}$
0.15	Low	$0.15^{+0.03}_{-0.03}$	$0.15^{+0.03}_{-0.02}$	$0.15^{+0.02}_{-0.02}$
	Med	$0.15^{+0.01}_{-0.02}$	$0.147^{+0.009}_{-0.008}$	$0.155^{+0.005}_{-0.005}$
	High	$0.150^{+0.008}_{-0.005}$	$0.149^{+0.003}_{-0.004}$	$0.150^{+0.002}_{-0.002}$
0.2	Low	$0.19^{+0.07}_{-0.05}$	$0.20^{+0.04}_{-0.03}$	$0.22^{+0.02}_{-0.02}$
	Med	$0.20^{+0.01}_{-0.01}$	$0.199^{+0.008}_{-0.009}$	$0.202^{+0.005}_{-0.005}$
	High	$0.201^{+0.004}_{-0.004}$	$0.200^{+0.003}_{-0.003}$	$0.198^{+0.002}_{-0.002}$
0.25	Low	$0.26^{+0.05}_{-0.04}$	$0.27^{+0.03}_{-0.04}$	$0.27^{+0.03}_{-0.03}$
	Med	$0.26^{+0.05}_{-0.03}$	$0.25^{+0.01}_{-0.01}$	$0.257^{+0.009}_{-0.008}$
	High	$0.250^{+0.003}_{-0.003}$	$0.249^{+0.002}_{-0.002}$	$0.249^{+0.001}_{-0.001}$
0.3	Low	$0.29^{+0.05}_{-0.05}$	$0.30^{+0.03}_{-0.03}$	$0.30^{+0.02}_{-0.02}$
	Med	$0.30^{+0.02}_{-0.01}$	$0.299^{+0.006}_{-0.005}$	$0.299^{+0.004}_{-0.004}$
	High	$0.300^{+0.003}_{-0.002}$	$0.300^{+0.001}_{-0.002}$	$0.300^{+0.001}_{-0.001}$
0.35	Low	$0.35^{+0.03}_{-0.04}$	$0.35^{+0.04}_{-0.03}$	$0.33^{+0.02}_{-0.02}$
	Med	$0.35^{+0.03}_{-0.03}$	$0.35^{+0.02}_{-0.02}$	$0.352^{+0.009}_{-0.008}$
	High	$0.350^{+0.004}_{-0.003}$	$0.349^{+0.003}_{-0.003}$	$0.350^{+0.001}_{-0.001}$
0.4	Low	$0.40^{+0.04}_{-0.04}$	$0.40^{+0.04}_{-0.04}$	$0.40^{+0.03}_{-0.02}$
	Med	$0.40^{+0.02}_{-0.02}$	$0.40^{+0.01}_{-0.01}$	$0.396^{+0.007}_{-0.007}$
	High	$0.400^{+0.004}_{-0.003}$	$0.400^{+0.002}_{-0.002}$	$0.400^{+0.001}_{-0.001}$
0.45	Low	$0.45^{+0.03}_{-0.04}$	$0.46^{+0.03}_{-0.04}$	$0.46^{+0.02}_{-0.03}$
	Med	$0.44^{+0.02}_{-0.02}$	$0.45^{+0.01}_{-0.02}$	$0.453^{+0.009}_{-0.008}$
	High	$0.449^{+0.006}_{-0.005}$	$0.451^{+0.004}_{-0.004}$	$0.451^{+0.002}_{-0.002}$

λ_v true	SNR	3 detectors	4 detectors	5 detectors
0.5	Low	$0.47^{+0.02}_{-0.03}$	$0.48^{+0.01}_{-0.02}$	$0.47^{+0.02}_{-0.02}$
	Med	$0.49^{+0.01}_{-0.02}$	$0.49^{+0.008}_{-0.02}$	$0.493^{+0.005}_{-0.008}$
	High	$0.497^{+0.002}_{-0.006}$	$0.498^{+0.001}_{-0.003}$	$0.498^{+0.001}_{-0.002}$

Table A.13: Table of λ_v median and errors corresponding to a 90% credible interval for the posterior probability distributions in Figures 3.14, 3.15, 3.16 and Histograms in Figure A.5.

λ_v true	SNR	3 detectors	4 detectors	5 detectors
0.0	Low	0.05	0.03	0.02
	Med	0.013	0.009	0.008
	High	0.004	0.003	0.0011
0.5	Low	0.45	0.46	0.45
	Med	0.47	0.48	0.487
	High	0.493	0.496	0.497

Table A.14: Table of λ_v posterior 90% upper (row 1) and lower (row 2) limits (corresponding to true values $\lambda_v = 0.0$ and $\lambda_v = 0.5$ respectively) in Figures 3.14, 3.15, 3.16.

λ_s true	SNR	3 detectors	4 detectors	5 detectors
0.7	Low	$0.7^{+0.08}_{-0.1}$	$0.68^{+0.05}_{-0.06}$	$0.72^{+0.04}_{-0.04}$
0.86	Low	$0.86^{+0.08}_{-0.08}$	$0.87^{+0.06}_{-0.05}$	$0.86^{+0.04}_{-0.04}$
0.53	Low	$0.5^{+0.2}_{-0.1}$	$0.53^{+0.07}_{-0.05}$	$0.53^{+0.04}_{-0.04}$
0.43	Low	$0.43^{+0.08}_{-0.07}$	$0.43^{+0.06}_{-0.06}$	$0.46^{+0.04}_{-0.04}$
0.37	Low	$0.4^{+0.09}_{-0.1}$	$0.37^{+0.05}_{-0.05}$	$0.35^{+0.03}_{-0.03}$
0.4	Low	$0.4^{+0.09}_{-0.1}$	$0.37^{+0.07}_{-0.08}$	$0.38^{+0.06}_{-0.06}$
0.1	Low	$0.1^{+0.2}_{-0.08}$	$0.12^{+0.05}_{-0.06}$	$0.08^{+0.04}_{-0.04}$
0.21	Low	$0.21^{+0.07}_{-0.04}$	$0.21^{+0.03}_{-0.03}$	$0.21^{+0.02}_{-0.02}$
0.12	Low	$0.1^{+0.1}_{-0.1}$	$0.1^{+0.1}_{-0.09}$	$0.12^{+0.06}_{-0.06}$
0.03	Low	$0.03^{+0.04}_{-0.03}$	$0.03^{+0.03}_{-0.02}$	$0.03^{+0.02}_{-0.02}$
0.0	Low	$0.03^{+0.05}_{-0.03}$	$0.02^{+0.04}_{-0.02}$	$0.03^{+0.03}_{-0.02}$

λ_s true	SNR	3 detectors	4 detectors	5 detectors
0.06	Med	$0.06^{+0.02}_{-0.03}$	$0.06^{+0.01}_{-0.01}$	$0.058^{+0.008}_{-0.008}$
0.36	Med	$0.36^{+0.02}_{-0.03}$	$0.36^{+0.02}_{-0.01}$	$0.361^{+0.008}_{-0.007}$
0.45	Med	$0.45^{+0.05}_{-0.04}$	$0.45^{+0.01}_{-0.02}$	$0.455^{+0.009}_{-0.009}$
0.38	Med	$0.38^{+0.04}_{-0.02}$	$0.39^{+0.02}_{-0.02}$	$0.37^{+0.01}_{-0.01}$
0.49	Med	$0.49^{+0.02}_{-0.02}$	$0.49^{+0.02}_{-0.02}$	$0.484^{+0.009}_{-0.009}$
0.33	Med	$0.3^{+0.02}_{-0.1}$	$0.33^{+0.01}_{-0.02}$	$0.32^{+0.01}_{-0.01}$
0.33	Med	$0.33^{+0.02}_{-0.04}$	$0.33^{+0.01}_{-0.02}$	$0.331^{+0.008}_{-0.008}$
0.18	Med	$0.18^{+0.06}_{-0.04}$	$0.18^{+0.04}_{-0.03}$	$0.17^{+0.02}_{-0.02}$
0.06	Med	$0.07^{+0.06}_{-0.04}$	$0.06^{+0.03}_{-0.02}$	$0.07^{+0.02}_{-0.02}$
0.05	Med	$0.05^{+0.05}_{-0.04}$	$0.06^{+0.03}_{-0.03}$	$0.04^{+0.02}_{-0.02}$
0.0	Med	$0.02^{+0.04}_{-0.02}$	$0.02^{+0.02}_{-0.01}$	$0.01^{+0.02}_{-0.009}$
0.75	High	$0.75^{+0.007}_{-0.01}$	$0.747^{+0.005}_{-0.006}$	$0.748^{+0.003}_{-0.003}$
0.1	High	$0.10^{+0.009}_{-0.01}$	$0.100^{+0.004}_{-0.004}$	$0.101^{+0.002}_{-0.002}$
0.4	High	$0.40^{+0.01}_{-0.01}$	$0.402^{+0.007}_{-0.007}$	$0.402^{+0.005}_{-0.005}$
0.24	High	$0.24^{+0.01}_{-0.03}$	$0.24^{+0.01}_{-0.009}$	$0.242^{+0.006}_{-0.006}$
0.36	High	$0.36^{+0.009}_{-0.01}$	$0.360^{+0.005}_{-0.007}$	$0.364^{+0.003}_{-0.003}$
0.22	High	$0.219^{+0.008}_{-0.007}$	$0.219^{+0.005}_{-0.005}$	$0.218^{+0.003}_{-0.003}$
0.29	High	$0.290^{+0.004}_{-0.003}$	$0.290^{+0.004}_{-0.003}$	$0.289^{+0.002}_{-0.002}$
0.3	High	$0.298^{+0.006}_{-0.008}$	$0.300^{+0.005}_{-0.006}$	$0.299^{+0.003}_{-0.003}$
0.04	High	$0.040^{+0.009}_{-0.009}$	$0.040^{+0.004}_{-0.004}$	$0.042^{+0.003}_{-0.003}$
0.06	High	$0.060^{+0.006}_{-0.008}$	$0.060^{+0.004}_{-0.003}$	$0.060^{+0.002}_{-0.002}$
0.0	High	$0.00^{+0.01}_{-0.002}$	$0.002^{+0.004}_{-0.001}$	$0.001^{+0.003}_{-0.001}$

Table A.15: Table of λ_s median and errors corresponding to a 90% credible interval for the posterior probability distributions in Figures 3.14, 3.15, 3.16 and Histograms in Figure A.6.

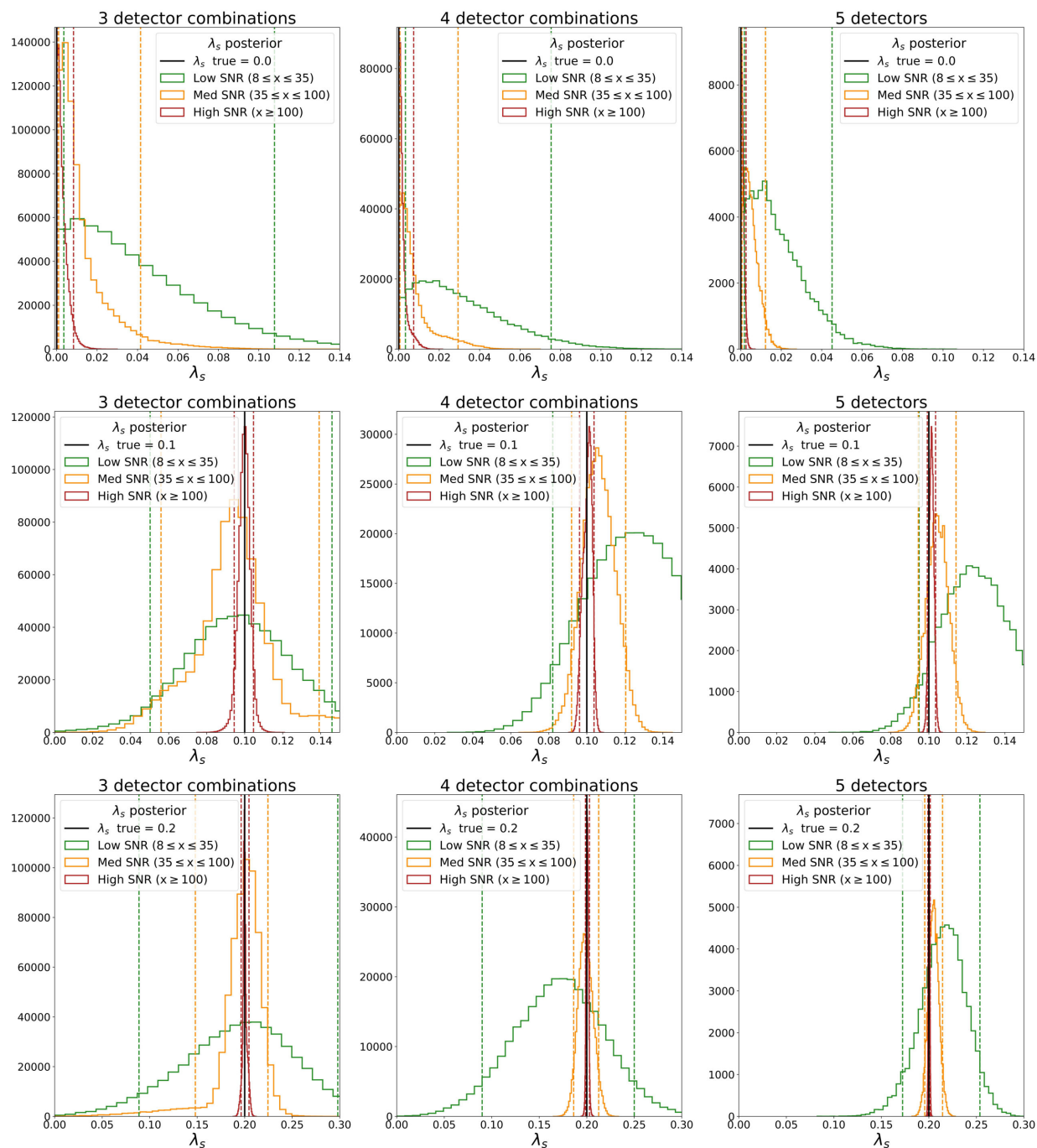
λ_s posterior for tvs polarized GWs; uniform ψ prior

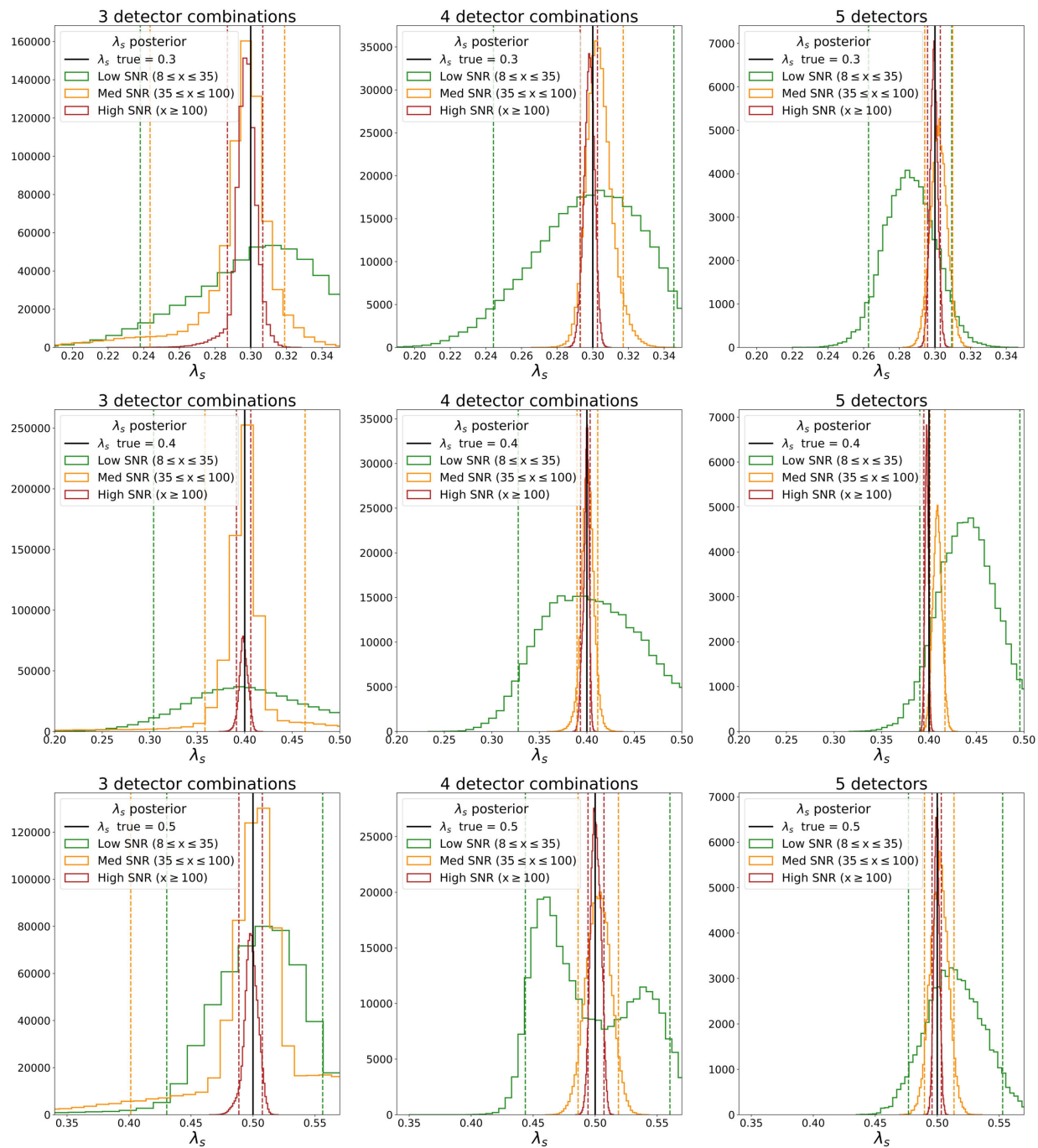
In the following Figure A.6, we plot histograms of λ_s posterior probability distributions for tvs polarized GWs. The rows step through 11 progressively increasing values of $\lambda_s \in [0, 1]$. The remaining polarization content is randomly distributed between tensor (λ_t) and vector (λ_v) components as per the constraint in Equation 2.9. The ψ prior distribution is uniform and periodic $\in [0, \pi]$ for the Bayesian parameter estimation.

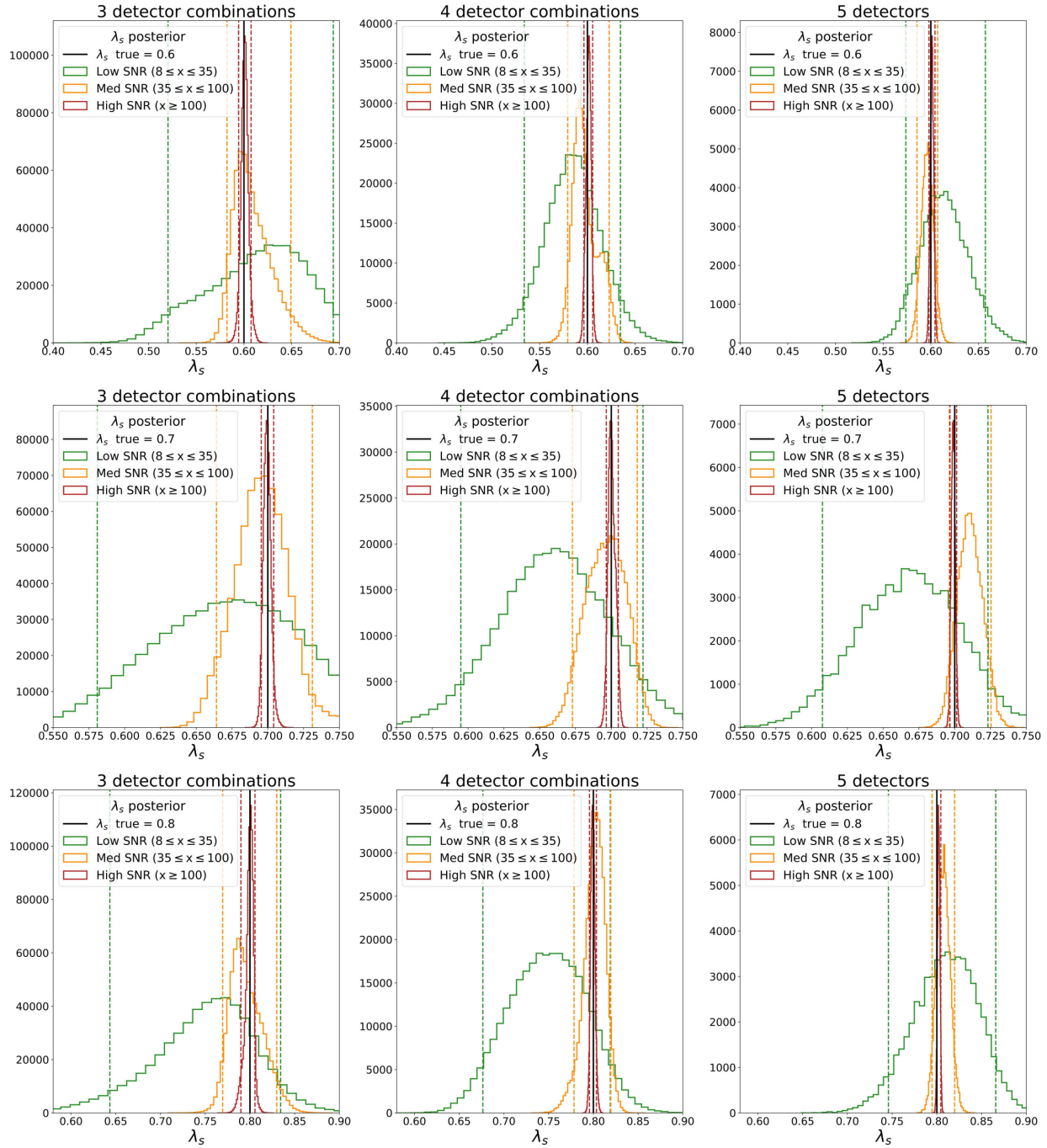
The 90% credible intervals for the λ_s and λ_v posterior probability distributions are given in Tables A.16 and A.18 respectively. The 90% upper and lower limits for the λ_s posterior probability distributions (corresponding to true values $\lambda_s = 0.0$ and $\lambda_s = 1.0$ respectively) are given in Table A.17.

However, the LIGO Caltech computing cluster was overburdened at the time when these jobs were submitted. As a result, 519 out of 528 jobs were completed in a reasonable time (16 days). The list of injections that are missing from our results is as follows:

Number of detectors	Detector combination	SNR	λ_s true
3 detectors	[L1, K1, I1]	medium	$\lambda_s = 0.2$
	[V1, K1, I1]	low	$\lambda_s = 0.6$
	[V1, K1, I1]	high	$\lambda_s = 0.7$
	[L1, V1, K1]	low	$\lambda_s = 0.8$
	[L1, V1, I1]	low	$\lambda_s = 1.0$
4 detectors	[H1, L1, K1, I1]	medium	$\lambda_s = 0.0$
	[L1, V1, K1, I1]	medium	$\lambda_s = 0.4$
	[H1, L1, K1, I1]	medium	$\lambda_s = 0.5$
	[H1, L1, V1, I1]	low	$\lambda_s = 1.0$







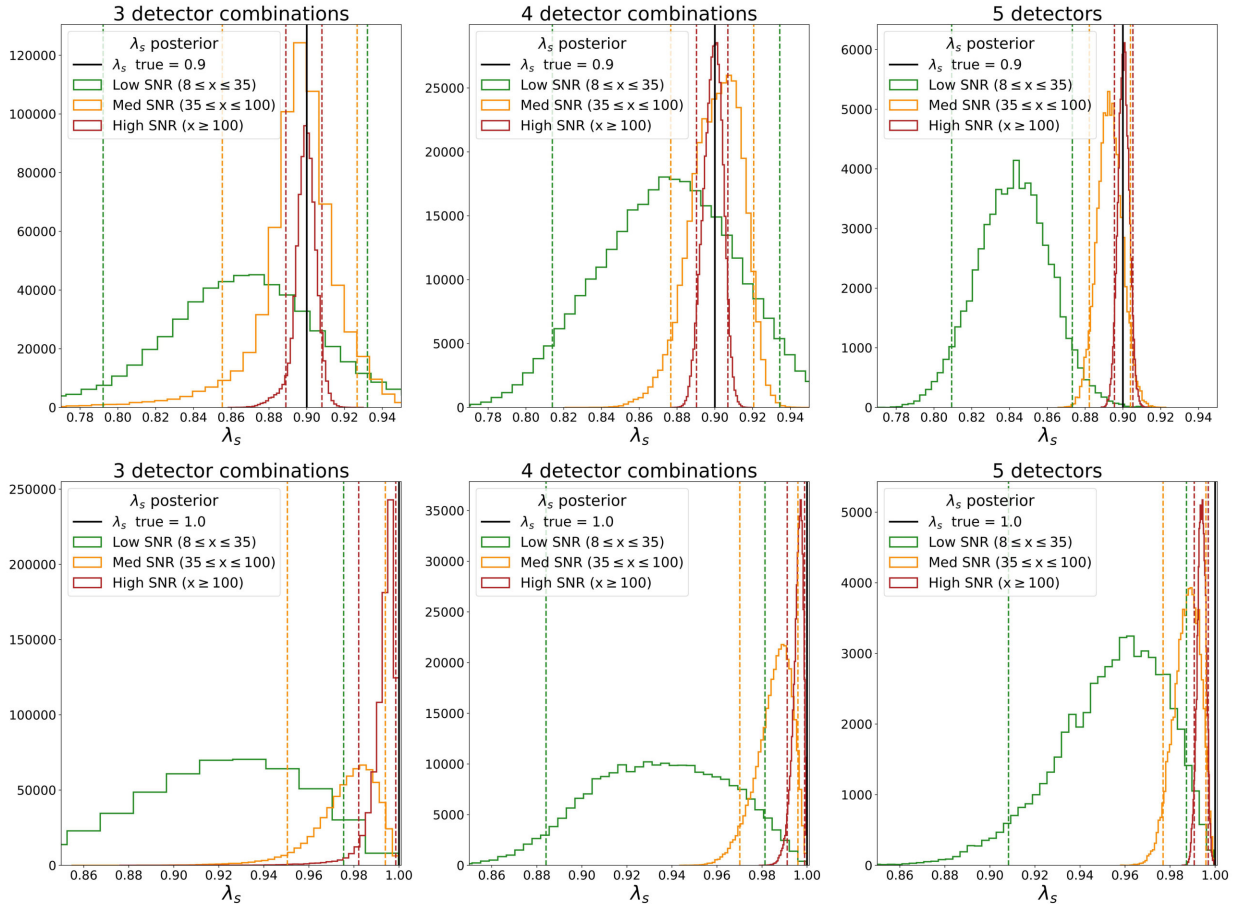


Figure A.6: Histograms of λ_s posteriors for tvs polarized GWs averaged over three, four and five detector combinations for low, medium and high SNRs (corresponding to Figures 3.17, 3.18 and 3.19 respectively). The rows step through 11 progressively increasing values of $\lambda_s \in [0, 1]$. The remaining polarization content is randomly distributed between tensor (λ_t) and vector (λ_v) components as per the constraint in Equation 2.9. Each histogram corresponds to an injection with a randomly chosen sky location and polarization angle (ψ). The ψ prior distribution is uniform and periodic $\in [0, \pi]$ for the Bayesian parameter estimation.

λ_s true	SNR	3 detectors	4 detectors	5 detectors
0.0	Low	$0.03^{+0.07}_{-0.03}$	$0.03^{+0.05}_{-0.02}$	$0.02^{+0.03}_{-0.01}$
	Med	$0.01^{+0.03}_{-0.007}$	$0.01^{+0.02}_{-0.005}$	$0.005^{+0.008}_{-0.004}$
	High	$0.002^{+0.006}_{-0.002}$	$0.001^{+0.006}_{-0.001}$	$0.001^{+0.002}_{-0.0007}$
0.1	Low	$0.10^{+0.05}_{-0.05}$	$0.13^{+0.04}_{-0.04}$	$0.12^{+0.03}_{-0.03}$
	Med	$0.09^{+0.04}_{-0.04}$	$0.11^{+0.01}_{-0.01}$	$0.10^{+0.01}_{-0.01}$
	High	$0.100^{+0.005}_{-0.005}$	$0.101^{+0.003}_{-0.004}$	$0.101^{+0.002}_{-0.002}$
0.2	Low	$0.2^{+0.1}_{-0.1}$	$0.17^{+0.08}_{-0.08}$	$0.22^{+0.04}_{-0.04}$
	Med	$0.20^{+0.02}_{-0.05}$	$0.20^{+0.01}_{-0.01}$	$0.205^{+0.009}_{-0.009}$
	High	$0.200^{+0.005}_{-0.004}$	$0.201^{+0.002}_{-0.002}$	$0.200^{+0.001}_{-0.001}$
0.3	Low	$0.31^{+0.06}_{-0.07}$	$0.30^{+0.05}_{-0.06}$	$0.29^{+0.02}_{-0.02}$
	Med	$0.30^{+0.02}_{-0.05}$	$0.30^{+0.01}_{-0.01}$	$0.302^{+0.008}_{-0.008}$
	High	$0.30^{+0.009}_{-0.01}$	$0.298^{+0.005}_{-0.005}$	$0.299^{+0.004}_{-0.004}$
0.4	Low	$0.4^{+0.1}_{-0.1}$	$0.4^{+0.1}_{-0.08}$	$0.44^{+0.05}_{-0.05}$
	Med	$0.40^{+0.06}_{-0.04}$	$0.40^{+0.01}_{-0.01}$	$0.409^{+0.008}_{-0.008}$
	High	$0.399^{+0.008}_{-0.007}$	$0.400^{+0.004}_{-0.006}$	$0.398^{+0.003}_{-0.003}$
0.5	Low	$0.50^{+0.05}_{-0.07}$	$0.49^{+0.07}_{-0.04}$	$0.51^{+0.04}_{-0.04}$
	Med	$0.5^{+0.08}_{-0.1}$	$0.50^{+0.02}_{-0.02}$	$0.50^{+0.01}_{-0.01}$
	High	$0.50^{+0.009}_{-0.01}$	$0.500^{+0.007}_{-0.006}$	$0.500^{+0.004}_{-0.004}$
0.6	Low	$0.6^{+0.07}_{-0.1}$	$0.58^{+0.05}_{-0.05}$	$0.61^{+0.04}_{-0.04}$
	Med	$0.61^{+0.04}_{-0.02}$	$0.60^{+0.03}_{-0.02}$	$0.60^{+0.01}_{-0.01}$
	High	$0.601^{+0.007}_{-0.006}$	$0.601^{+0.004}_{-0.005}$	$0.601^{+0.003}_{-0.003}$
0.7	Low	$0.67^{+0.08}_{-0.09}$	$0.66^{+0.06}_{-0.06}$	$0.67^{+0.06}_{-0.06}$
	Med	$0.70^{+0.04}_{-0.03}$	$0.70^{+0.02}_{-0.02}$	$0.71^{+0.01}_{-0.01}$
	High	$0.699^{+0.005}_{-0.004}$	$0.700^{+0.005}_{-0.004}$	$0.699^{+0.002}_{-0.002}$
0.8	Low	$0.8^{+0.08}_{-0.1}$	$0.75^{+0.07}_{-0.07}$	$0.81^{+0.05}_{-0.07}$
	Med	$0.79^{+0.04}_{-0.02}$	$0.80^{+0.02}_{-0.02}$	$0.81^{+0.01}_{-0.01}$
	High	$0.80^{+0.006}_{-0.01}$	$0.799^{+0.004}_{-0.004}$	$0.802^{+0.002}_{-0.002}$
0.9	Low	$0.87^{+0.07}_{-0.07}$	$0.88^{+0.06}_{-0.06}$	$0.84^{+0.03}_{-0.03}$
	Med	$0.90^{+0.03}_{-0.04}$	$0.90^{+0.02}_{-0.03}$	$0.89^{+0.01}_{-0.01}$
	High	$0.90^{+0.008}_{-0.01}$	$0.899^{+0.008}_{-0.009}$	$0.900^{+0.005}_{-0.005}$

λ_s true	SNR	3 detectors	4 detectors	5 detectors
1.0	Low	$0.92^{+0.05}_{-0.09}$	$0.93^{+0.05}_{-0.05}$	$0.96^{+0.03}_{-0.05}$
	Med	$0.98^{+0.01}_{-0.03}$	$0.99^{+0.009}_{-0.02}$	$0.99^{+0.008}_{-0.01}$
	High	$0.99^{+0.004}_{-0.01}$	$0.996^{+0.003}_{-0.005}$	$0.994^{+0.003}_{-0.003}$

Table A.16: Table of λ_s median and errors corresponding to a 90% credible interval for the posterior probability distributions in Figures 3.17, 3.18, 3.19 and Histograms in Figure A.6.

λ_s true	SNR	3 detectors	4 detectors	5 detectors
0.0	Low	0.08	0.07	0.04
	Med	0.03	0.03	0.011
	High	0.006	0.005	0.002
1.0	Low	0.86	0.89	0.92
	Med	0.96	0.98	0.979
	High	0.987	0.992	0.991

Table A.17: Table of λ_s posterior 90% upper (row 1) and lower (row 2) limits (corresponding to true values $\lambda_s = 0.0$ and $\lambda_s = 1.0$ respectively) in Figures 3.17, 3.18, 3.19.

λ_v true	SNR	3 detectors	4 detectors	5 detectors
0.41	Low	$0.40^{+0.04}_{-0.04}$	$0.40^{+0.02}_{-0.04}$	$0.40^{+0.01}_{-0.02}$
0.06	Low	$0.06^{+0.04}_{-0.04}$	$0.05^{+0.03}_{-0.03}$	$0.04^{+0.02}_{-0.02}$
0.08	Low	$0.08^{+0.03}_{-0.03}$	$0.08^{+0.02}_{-0.02}$	$0.08^{+0.01}_{-0.01}$
0.08	Low	$0.07^{+0.05}_{-0.04}$	$0.08^{+0.04}_{-0.03}$	$0.09^{+0.02}_{-0.02}$
0.13	Low	$0.13^{+0.06}_{-0.08}$	$0.14^{+0.05}_{-0.07}$	$0.11^{+0.03}_{-0.04}$
0.2	Low	$0.20^{+0.05}_{-0.04}$	$0.21^{+0.02}_{-0.05}$	$0.19^{+0.02}_{-0.02}$
0.09	Low	$0.09^{+0.07}_{-0.04}$	$0.09^{+0.02}_{-0.05}$	$0.11^{+0.01}_{-0.02}$
0.01	Low	$0.03^{+0.06}_{-0.02}$	$0.02^{+0.04}_{-0.02}$	$0.03^{+0.03}_{-0.03}$
0.1	Low	$0.10^{+0.04}_{-0.04}$	$0.11^{+0.03}_{-0.04}$	$0.07^{+0.02}_{-0.02}$
0.0	Low	$0.02^{+0.04}_{-0.02}$	$0.02^{+0.03}_{-0.02}$	$0.01^{+0.02}_{-0.01}$
0.0	Low	$0.02^{+0.05}_{-0.02}$	$0.01^{+0.02}_{-0.01}$	$0.01^{+0.02}_{-0.01}$

λ_ν true	SNR	3 detectors	4 detectors	5 detectors
0.09	Med	0.09 ^{+0.01} _{-0.01}	0.091 ^{+0.008} _{-0.009}	0.088 ^{+0.006} _{-0.006}
0.08	Med	0.08 ^{+0.01} _{-0.01}	0.08 ^{+0.009} _{-0.01}	0.077 ^{+0.005} _{-0.005}
0.04	Med	0.04 ^{+0.01} _{-0.01}	0.044 ^{+0.007} _{-0.007}	0.043 ^{+0.006} _{-0.006}
0.06	Med	0.06 ^{+0.01} _{-0.02}	0.058 ^{+0.008} _{-0.009}	0.070 ^{+0.006} _{-0.006}
0.22	Med	0.22 ^{+0.01} _{-0.01}	0.220 ^{+0.005} _{-0.006}	0.223 ^{+0.003} _{-0.004}
0.21	Med	0.21 ^{+0.04} _{-0.04}	0.21 ^{+0.01} _{-0.01}	0.204 ^{+0.008} _{-0.008}
0.14	Med	0.14 ^{+0.02} _{-0.02}	0.14 ^{+0.009} _{-0.01}	0.143 ^{+0.006} _{-0.006}
0.14	Med	0.14 ^{+0.01} _{-0.01}	0.140 ^{+0.007} _{-0.006}	0.136 ^{+0.005} _{-0.005}
0.03	Med	0.03 ^{+0.01} _{-0.02}	0.03 ^{+0.01} _{-0.01}	0.026 ^{+0.006} _{-0.006}
0.04	Med	0.04 ^{+0.01} _{-0.02}	0.04 ^{+0.01} _{-0.01}	0.039 ^{+0.006} _{-0.006}
0.0	Med	0.00 ^{+0.01} _{-0.003}	0.003 ^{+0.005} _{-0.002}	0.002 ^{+0.003} _{-0.002}
0.09	High	0.090 ^{+0.002} _{-0.002}	0.090 ^{+0.001} _{-0.001}	0.091 ^{+0.001} _{-0.001}
0.22	High	0.220 ^{+0.004} _{-0.003}	0.220 ^{+0.003} _{-0.003}	0.219 ^{+0.002} _{-0.002}
0.08	High	0.08 ^{+0.007} _{-0.01}	0.079 ^{+0.005} _{-0.005}	0.079 ^{+0.002} _{-0.002}
0.19	High	0.19 ^{+0.01} _{-0.004}	0.191 ^{+0.003} _{-0.003}	0.191 ^{+0.002} _{-0.002}
0.2	High	0.201 ^{+0.005} _{-0.003}	0.200 ^{+0.002} _{-0.002}	0.201 ^{+0.001} _{-0.001}
0.01	High	0.009 ^{+0.003} _{-0.003}	0.010 ^{+0.002} _{-0.002}	0.010 ^{+0.002} _{-0.002}
0.09	High	0.090 ^{+0.003} _{-0.003}	0.090 ^{+0.002} _{-0.002}	0.090 ^{+0.001} _{-0.001}
0.08	High	0.080 ^{+0.003} _{-0.004}	0.080 ^{+0.002} _{-0.002}	0.080 ^{+0.002} _{-0.002}
0.01	High	0.010 ^{+0.005} _{-0.004}	0.010 ^{+0.002} _{-0.003}	0.008 ^{+0.001} _{-0.002}
0.03	High	0.030 ^{+0.002} _{-0.002}	0.030 ^{+0.002} _{-0.001}	0.030 ^{+0.001} _{-0.001}
0.0	High	0.002 ^{+0.005} _{-0.001}	0.001 ^{+0.002} _{-0.001}	0.002 ^{+0.002} _{-0.001}

Table A.18: Table of λ_ν median and errors corresponding to a 90% credible interval for the posterior probability distributions in Figures 3.17, 3.18, 3.19 and Histograms in Figure A.6.

$\vec{\lambda}$ posteriors for tvs polarized GWs with different BBH component masses

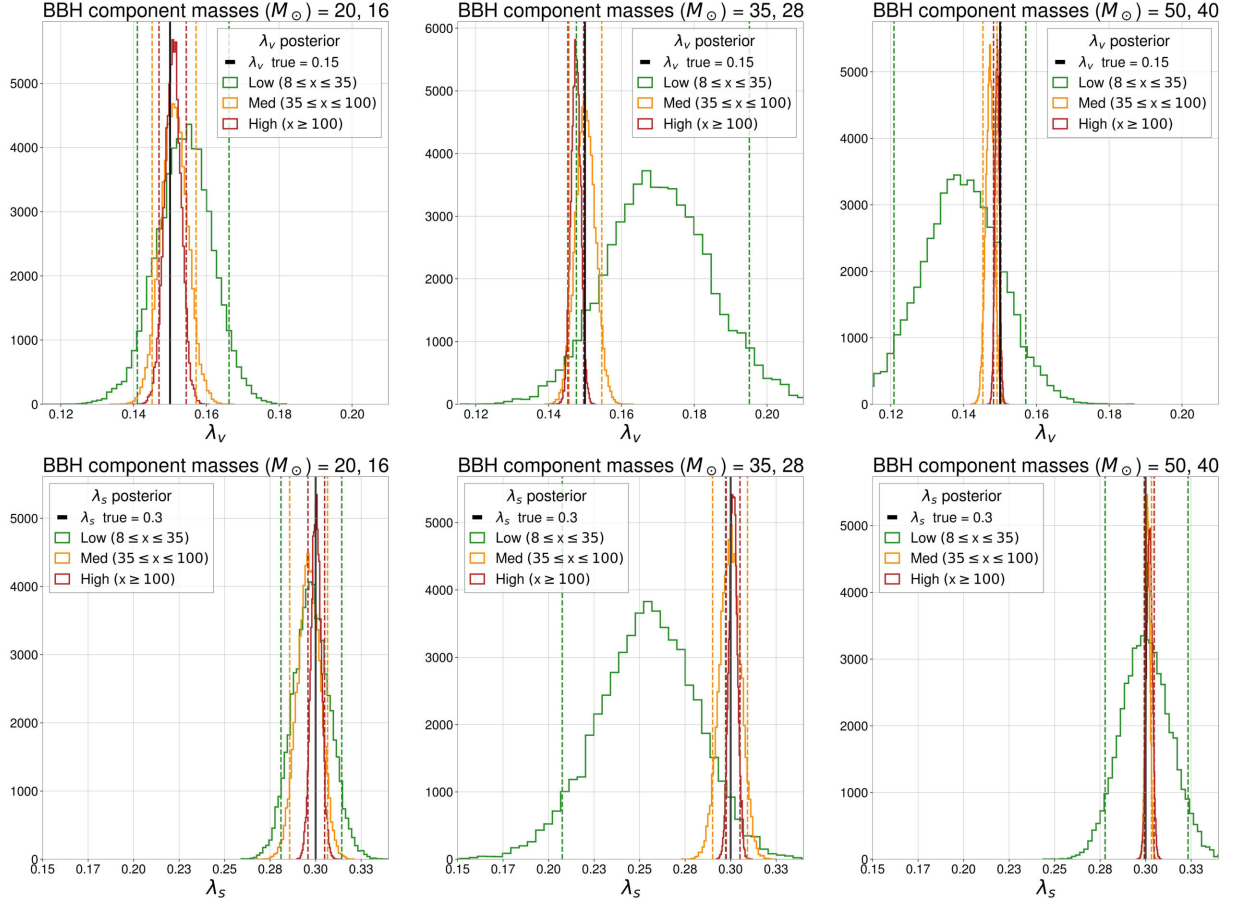


Figure A.7: Histograms of λ_v (top) and λ_s (bottom) posteriors for tvs polarized GWs from BBHs with progressively increasing component masses for low, medium and high SNRs in five detectors (corresponding to Figure 3.20). The true values of the $\vec{\lambda}$ parameters are $\lambda_t = 0.2$, $\lambda_v = 0.15$ and $\lambda_s = 0.3$. Each histogram corresponds to an injection with a randomly chosen sky location and polarization angle (ψ).

λ_v true	SNR	$m_1 = 20 M_\odot$ $m_2 = 16 M_\odot$	$m_1 = 35 M_\odot$ $m_2 = 28 M_\odot$	$m_1 = 50 M_\odot$ $m_2 = 40 M_\odot$
0.15	Low	$0.15^{+0.01}_{-0.01}$	$0.17^{+0.03}_{-0.02}$	$0.14^{+0.02}_{-0.02}$
	Med	$0.151^{+0.006}_{-0.006}$	$0.150^{+0.005}_{-0.004}$	$0.147^{+0.002}_{-0.002}$
	High	$0.151^{+0.004}_{-0.004}$	$0.147^{+0.002}_{-0.002}$	$0.149^{+0.001}_{-0.001}$

Table A.19: Table of λ_v median and errors corresponding to a 90% credible interval for the posterior probability distributions in Figure 3.20 and Histogram in Figure A.7

λ_s true	SNR	$m_1 = 20 M_\odot$ $m_2 = 16 M_\odot$	$m_1 = 35 M_\odot$ $m_2 = 28 M_\odot$	$m_1 = 50 M_\odot$ $m_2 = 40 M_\odot$
0.3	Low	$0.30^{+0.02}_{-0.02}$	$0.25^{+0.04}_{-0.05}$	$0.30^{+0.02}_{-0.02}$
	Med	$0.30^{+0.01}_{-0.01}$	$0.30^{+0.009}_{-0.01}$	$0.301^{+0.002}_{-0.002}$
	High	$0.300^{+0.005}_{-0.004}$	$0.301^{+0.004}_{-0.004}$	$0.302^{+0.003}_{-0.003}$

Table A.20: Table of λ_s median and errors corresponding to a 90% credible interval for the posterior probability distributions in Figure 3.20 and Histogram in Figure A.7